University of Calgary

PRISM Repository **https://prism.ucalgary.ca**

The Vault Open Theses and Dissertations

2017-12-22

Quantifying the Impact of Seismic Lines on Methane Release in a Treed Bog Ecosystem using Unmanned Aerial Vehicles (UAVs)

Lovitt, Julie

Lovitt, J. (2017). Quantifying the Impact of Seismic Lines on Methane Release in a Treed Bog Ecosystem using Unmanned Aerial Vehicles (UAVS) (Master's thesis, University of Calgary, Calgary, Canada). Retrieved from https://prism.ucalgary.ca.

http://hdl.handle.net/1880/106259

Downloaded from PRISM Repository, University of Calgary

UNIVERSITY OF CALGARY

QUANTIFYING THE IMPACT OF SEISMIC LINES ON METHANE RELEASE IN A TREED BOG ECOSYSTEM USING UNMANNED AERIAL VEHICLES (UAVS)

by

Julie Lovitt

A THESIS

SUBMITTED TO THE FACULTY OF GRADUATE STUDIES

IN PARTIAL FULFILMENT OF THE REQUIREMENTS FOR THE

DEGREE OF MASTER OF SCIENCE

GRADUATE PROGRAM IN GEOGRAPHY

CALGARY, ALBERTA

DECEMBER, 2017

© Julie Lovitt, 2017

Abstract

Peatlands are extremely complex and sensitive ecosystems, capable of releasing vast amounts of methane in response to disturbance events. To date, little advancement has been made by researchers to quantify the impact of small-scale anthropogenic disturbances on these ecosystems, specifically seismic lines. These "low-impact" linear features present a challenge to researchers as they exist at dimensions too small for the majority of remote-sensing platforms to successfully identify and measure, even though they account for a considerable portion of land disturbance in Canada's western Boreal, and are anticipated to have extensive, compounding environmental effects. This thesis summarizes how unmanned aerial vehicle photogrammetry can be used to address this knowledge gap by showcasing the ability to generate accurate peatland terrain models, and subsequently estimate seismic-line impacts on both physical parameters (microtopography and depth-to-water) and peatland methane emission, ultimately revealing one of the hidden impacts of seismic lines on Canada's Boreal peatlands.

Keywords: UAV, photogrammetry, boreal peatlands, seismic lines, methane, microtopography

Preface

This is a manuscript-based thesis prepared in accordance with the Faculty of Graduate Studies Guidelines at the University of Calgary. Chapter 2 was published in the open-access, peer-reviewed journal *Remote Sensing*, and has been reproduced under copyright agreement with the publisher MDPI. Chapter 3 was submitted to the peer-reviewed journal *Journal of Geophysical Research: Biogeosciences* on October 18, 2017 and is currently in review. I am intellectually responsible for the majority of works presented in this thesis, including research design, data collection, analysis, graphical preparation, and writing. Research presented in Chapter 2 was completed primarily by myself, whereas Chapter 3 presents more collaborative work, incorporating data prepared by various project partners in the analysis. Dr. Tak Fung with the University of Calgary assisted with statistical analysis presented in Chapter 2. The methane flux data used in Chapter 3 was collected, analyzed, and methods summarized by project colleague Saru Saraswati, a current PhD candidate with the University of Waterloo. The depth-to-water table used in Chapter 3 was generated, assessed and methods summarized by project colleague Mir Mustafizur Rahman, the project research technician at the University of Calgary. Dr. Rahman also assisted with data processing. Figure 3.5 in Chapter 3 was prepared in collaboration with Robin Poitras, a cartographer within the Department of Geography at the University of Calgary. Dr. Gregory McDermid (University of Calgary), Dr. Maria Strack (University of Waterloo), and Dr. Bin Xu (NAIT) assisted in developing overall research design and logistics, and have reviewed final drafts of the articles prior to journal submission.

The vast majority of research focusing on seismic line disturbances within Boreal peatlands has described impacts primarily in terms of habitat fragmentation or suitability, rather than

peatland carbon cycling and storage functions. In fact, no previous research describing the greenhouse-gas impacts of the ubiquitous linear-disturbance features within Boreal peatlands of western North America could be located. Therefore, the research and published works presented here represents my attempt to address this identified knowledge gap within the literature, and contribute meaningful data and methods for future studies to expand upon. The full and anticipated citations are as follows:

Chapter 2: Lovitt, J., Rahman, M.M., & McDermid, G.J. (2017). Assessing the Value of UAV Photogrammetry for Characterizing Terrain in Complex Peatlands. *Remote Sensing*. 9(7): 715.

Chapter 3: Lovitt, J., Rahman, M.M., Saraswati, S., McDermid, G.J., Strack, M., & Xu, B. (2017). UAV Remote Sensing Can Reveal the Effects of Low Impact Seismic Lines on Methane (CH_4) Release in a Boreal Treed Bog. *Journal of Geophysical Research: Biogeosciences*. [In Review].

Acknowledgements

This work would not have been possible without the incredible support I received from my family, friends and the entire F^3GISci team. First and foremost I would like to sincerely thank my supervisor, Dr. Gregory McDermid, who took a chance when he offered me a place in his lab. His unwavering confidence in my abilities was a constant source of inspiration to aim higher, motivating me to excel beyond what I had thought possible. Similarly, I must thank Dr. Mustafizur Rahman for being such a solid team member and friend, often saving me from my personal misgivings and helping me overcome technical obstacles. I lack the words to properly express the depth of my gratitude for these two amazing individuals, so I will simply say that they have profoundly changed my life in the most positive way possible and I will be eternally grateful for having met them.

I was tremendously fortunate to have worked with, and received guidance from, two inspiring scientists: Dr. Maria Strack and Dr. Bin Xu. My research was undoubtingly improved as a direct result of their critical review and insights. I would also like to thank Dr. Joule Bergerson, who served as my external internal examiner. Though our paths crossed only briefly, it was an absolute pleasure to have had her on my thesis review committee.

Of course I must thank everyone in the McDermid lab(s), who are their own special and wonderful breed of crazy. They readily accepted me into the tribe and made the past two years some of the best. I must also thank our collaborators at UWaterloo (Saraswati Belwase) and NAIT (Melanie Bird) who made our field work the most fun you can have north of Grande Prairie.

Finally, I could not have quit my job to pursue a graduate degree had it not been for the complete support and encouragement of my love, and best friend Mike.

For Mum, Dad and Mike heart.

Table of Contents

Abstract ii
Preface iii
Acknowledgements v
Table of Contents vii
List of Tables ix
List of Figures x
List of Symbols, Abbreviations and Nomenclature xii
List of Symbols, Abbreviations and Nomenclature (Continued) xiii
Epigraph xiv

Chapter One: Introduction 15
1.1 Overview 15
1.2 Background 17
1.2.1 Peatlands within Canada and Alberta. 18
1.2.1.1 Peatland Microtopography. ***19***
1.2.1.2 Controlling Factors of Peatland Methane Emission. ***21***
1.2.1.3 Peatland Response to Disturbances: Seismic Lines. ***22***
1.3 The Role of Remote Sensing in Modelling Peatland Ecosystems 25
1.3.1 Extracting Microtopographic Data. 28
1.3.2 Estimating Methane Emission. 29
1.4 Statement of the Problem 31
1.5 Research Objectives 31
1.6 Organization of the Thesis 32

Chapter Two: Assessing the Value of UAV Photogrammetry for Characterizing Terrain in Complex Peatlands 33
2.1 Abstract 33
2.2 Introduction 33
2.3 Materials and Methods 37
2.3.1. Study Area. 37
2.3.2. Data Sets. 40
2.3.2.1. Terrestrial Surveys. ***40***
2.3.2.2. Remote Sensing Observations. ***41***
2.3.3. Accuracy Assessments. 46
2.3.3.1. UAV Photogrammetry Dataset Performance. ***46***
2.3.3.2. Supplemented LiDAR Performance. ***46***
2.3.4. Statistical Analysis. 47
2.4 Results 48
2.5 Discussion 50
Potential Sources of Error. 53
2.6 Conclusions 54

2.7 References.....55

Chapter Three: UAV Remote Sensing Can Reveal the Effects of Low Impact Seismic Lines on Surface Morphology, Hydrology, and Methane (CH_4) Release in a Boreal Treed Bog.....58
3.1 Abstract.....58
3.2 Introduction.....58
3.3 Materials and Methods.....61
3.3.1 Study site. 61
3.3.2 Field-Measured CH_4 Flux (Point Samples). 64
3.3.3 Remote Sensing Observations. 66
3.3.4. Classification of Terrain (Microtopography). 67
3.3.5. Generating the Depth to Water Surface (DTW) Surface. 70
3.3.6. Predicted CH_4 Flux.....71
3.4 Results.....74
3.4.1 Seismic Line Impacts on Microtopography and DTW. 74
3.4.2 CH_4 Flux Estimates and Quantification of Seismic Line Impacts. 76
3.5 Discussion 79
3.5.1 Potential Sources of Error 81
3.6 Conclusions.....83
3.7 References.....84

Chapter Four: Conclusions.....89
4.1 Research Objectives Summary.....90
4.2 Research Contributions.....93
4.3 Recommendations for Future Research 96
4.4 Bibliography.....99

Appendix A: Tutorials.....105

List of Tables

Table 2.1: Dataset Accuracies: Comparison of Dataset Elevations against all RTK Surveyed Point Elevations (678 UAV Photogrammetry dataset and 629 LiDAR and UAV photogrammetry + LiDAR datasets)..... 48

Table 2.2: Dataset Accuracies: Comparison of Dataset Elevations against RTK Point Elevations Classified by Surface Complexity..... 49

Table 3.1: Confusion Matrix of Pixel-Based Density Slicing Classification Approach (Overall Accuracy = 84%; kappa = 0.76) 70

Table 3.2: Summary Table Showing Absolute and Average Differences in Microform Heights, Percent Coverage and Measured Depth-to-Water between Undisturbed and Disturbed Areas 75

Table 3.3: Predicted CH_4 Emissions (standard error) of 3.8ha Subset Study Site over 150-day monitoring Period and Estimated Increase (per ha) due to Seismic Line Disturbance..... 77

Table 3.4: Estimated Total CH_4 Emission across 61 ha Study Site (as per Figure 3.1a) and Predicted Increase over 150 day monitoring Period due to Seismic Line Disturbance..... 78

List of Figures

Figure 1.1: Comparison of Mer Bleue (Left, foreground) a well-researched bog near Ottawa, Ontario (retrieved from Kalacska et al., 2013), and a view of our study site (Right) located near Peace River, Alberta. Peatlands in western Canada are capable of sustaining tree growth, as is apparent in the images. 19

Figure 1.2: Examples of microforms. In the left pane a hollow is displayed as a hole in the surrounding vegetation and moss. In the right pane, a hummock is displayed as a clear moss mound, which rises above the surrounding peat surface. Both of these features occur at the sub-meter scale. Images were provided by project colleagues. 20

Figure 1.3: A low-impact seismic line traversing a boreal bog ecosystem in northern Alberta. This line was constructed in the late 2000s and though ground vegetation is apparent, few trees have reestablished. It is difficult to observe microtopography due to the presence of Labrador Tea. Image was provided by project partners. 23

Figure 2.1: Approximate site location in the province of Alberta (AB) with reference to nearby notable city centers (1a); estimated distribution of surface complexity classes across the study site (1b). An extensive network of linear disturbances transect the site. Areas between these features are assumed to be undisturbed and indicative of natural boreal treed bog conditions within the region. GCP installation locations, cluster sample and detailed transect points are shown (1b), and described in Section 2.3.2.1. 38

Figure 2.2: Examples of each surface complexity class found within the study site. Data displayed is captured from the orthophoto. The example of Class 0 (2.2a) is taken from the new clay road bisecting the study area, Class 1 (2.2b) is taken from a pipeline ROW, Class 2 (2.2c) is from undisturbed portions of the bog, and Class 3 (2.2d) is from densely treed portion of bog. 39

Figure 2.3: Photogrammetric and point-cloud management software workflow illustrating the process of using UAV flight data to generate secondary (DPC and orthomosaic) and tertiary products (ground dense point cloud (gDPC)) used in this research. 44

Figure 2.4: A comparison of dataset performance along a detailed transect within an undisturbed portion of the study site (representing a mixture of Classes 2 and 3). Both UAV photogrammetry and LiDAR overestimate 'true' ground-surface elevation, represented in black, though UAV photogrammetry is better-able to capture microtopographic variability. The area in green indicates ground points that were fully covered by vegetation canopy. 50

Figure 2.5: Comparison of vegetation influence on dataset point densities, modeling a seismic line and adjacent undisturbed peatland. Examples of each surface complexity class indicated as: ① = Class 1 (low); ② = Class 2 (moderate); ③ = Class 3 (high). 52

Figure 3.1: Full Study Site Extents (3.1a) and Subset (3.1b) Showing Equal Area Polygons and Seismic Lines used to Generate Methane Flux Estimates from MT and DTW Surfaces (Process Explained in Section 2.2.3.3). Within Figure 3.1b, a variety of surface features can be observed including dispersed pockets of dense black spruce. 63

Figure 3.2: Relationship between LOGCH_4 ($mgm^{-2}d^{-1}$) and Water Table position (cm), where water table located below ground surface is given a negative value. Error bars indicate the standard error of LOG_{CH4} values (±0.13). 66

Figure 3.3: The workflow for generating microtopographic surface. 67

Figure 3.4: Process of producing the microtopography surface by subtracting the reference surface (Ref) from the digital terrain model (DTM). Areas above Ref are considered hummocks (brown), areas below are considered hollows (light blue), and areas which are masked are assigned the class 'Trees'. 69

Figure 3.5: Graphical visualization of digital surfaces generated from the input surface model (shown at top of stack). Surfaces include the bare earth and water table (WT), microtopography, depth to water (DTW) and CH_4. DTW is shown in centimeters where depths below ground surface are negative, CH_4 is shown in $mgCH_4\ m^{-2}\ d^{-1}$. The DTW surface was derived from the bare earth and WT surfaces, the arrow shows this link to the WT position below ground surface. Figure prepared by Robin Poitras and Julie Lovitt at the University of Calgary. 73

List of Symbols, Abbreviations and Nomenclature

Abbreviation:	Definition:
ANOVA	Analysis of Variance
ASPRS	American Society for Photogrammetry and Remote Sensing
Avg ABS Error	Average Absolute Error
BC OGC	British Columbia Oil and Gas Commission
CH_4	Methane
CHM	Canopy Height Model
CIR	Colour Infrared Imagery
CO_2	Carbon Dioxide
DPC	Dense Point Cloud
DSM	Digital Surface Model
DTM	Digital Terrain Model
DTW	Depth-to-Water
FAO	Food and Agriculture Organization of the United Nations
GCP	Ground Control Point
gDPC	Ground Dense Point Cloud
GFWC	Global Forest Watch Canada
GHG	Greenhouse Gas
GNSS	Global Navigation Satellite System
GPS	Global Positioning System
GtC	Gigatons of Carbon
HH Model	Hummock Hollow Model
INS	Inertial Navigation System
LiDAR	Light Detection and Ranging
masl	Meters Above Sea Level
MT	Microtopography
NWWG	National Wetlands Working Group
RMSE	Root Mean Square Error
RTK	Real Time Kinematic
SfM	Structure from Motion

List of Symbols, Abbreviations and Nomenclature (Continued)

Abbreviation:	Definition:
UAV	Unmanned Aerial Vehicle
UAVP	Unmanned Aerial Vehicle Photogrammetry
WT	Water Table

Epigraph

"Life is like topography, Hobbes. There are summits of happiness and success, flat stretches of boring routine and valleys of frustration and failure."

-Calvin

Chapter One: Introduction

1.1 Overview

Peatlands are recognized as globally important ecosystems due to their role as regional hydrology regulators, biodiversity hotspots, and massive carbon stocks; containing approximately 30% of the Earth's terrestrial soil carbon (Parish et al., 2008; Joosten & Couwenberg, 2009; FAO, 2014). The vast majority of peatlands by area are concentrated within the northern latitudes, specifically within the Boreal Forest/Taiga biome, and coincide with the largest soil-organic carbon stocks (Wieder & Vitt, 2006; Strack, 2008; Parish et al., 2008; Scharlemann et al., 2014). Anoxic decomposition of organic matter within peatlands produces large amounts of methane gas (CH_4): a powerful greenhouse gas (GHG) that has approximately 28 times the global warming potential of CO_2 (Joosten & Couwenberg, 2009; Bridgham et al., 2013; FAO, 2014; Zhu et al., 2014). Wetlands are the largest natural source of CH_4, and a wealth of research has identified strong links between climatic conditions and wetland CH_4 release rates (Bridgham et al., 2013; Turetsky et al., 2014). The balance between environmental factors (hydrology, vegetation, chemistry, climate etc.) within northern peatlands is delicate and sensitive to disturbance events, which may trigger an ecological shift from peatlands serving as carbon sinks to carbon sources (Wieder & Vitt, 2006; Strack & Waddington, 2007; Parish et. al., 2008; Eppinga et al., 2009; Vitt & Bhatti, 2012; Strack & Waddington, 2012; Munir et al., 2014). In particular, anthropogenic disturbance of these sensitive ecosystems may alter environmental conditions to such a degree that CH_4 emissions increase exponentially within disturbed areas (Dabros et al., 2017). In the Boreal region of Alberta, petroleum resource exploration has resulted in the construction of a dense network of seismic lines, many of which intersect low-lying peatlands (Lee & Boutin, 2006; Schneider & Dyer, 2006; van

Rensen et al., 2015). Studying the impact of these linear features on the landscapes they traverse has proven to be a difficult task, as they exist in predominately remote locations unsuitable for access by foot, cross numerous ecosystem types, and generally occur at scales too small for many remote-sensing platforms (ie. satellites) to observe. As a result, the impact of seismic lines on peatland CH_4 emission rates is largely unknown, and has yet to be quantified accurately at any scale (ie. local, regional, or provincial).

Unmanned aerial vehicles (UAVs) are remote-sensing platforms capable of collecting ultra-high resolution aerial imagery over large areas, and offer a desirable alternative to traditional ground-survey methods, which are more costly and labour-intensive (Knoth et. al., 2013; Roosevelt, 2014). For example, high-density photogrammetric point clouds and orthophotography generated from UAV data are ideal for investigating small-scale surface features such as peatland microtopography, CH_4 hotspots, and linear disturbances like seismic lines (Pirotti & Tarolli, 2010). Several studies have indicated that these platforms are well-suited to mapping peatland terrain in high detail when canopy is sparse (Lucieer et al., 2014; Roosevelt, 2014; Turner et al., 2014; Lehmann et. al., 2016), however their applicability within the more complex, treed peatlands common to western Canada has yet to be tested.

This thesis endeavors to describe UAV capabilities in modelling complex peatland terrain, and to demonstrate how these models can be used to quantify seismic-line impacts on both peatland CH_4 release, and surface structure: specifically microtopography and depth-to-water. The research presented here discusses data collected from one study site – a treed bog in northwestern Alberta – and is not anticipated to represent all cases of peatland-seismic disturbance within the province. However, it does present the first-known estimation of seismic-line impacts within a peatland

complex, and is anticipated to serve as a stepping stone for future research, and perhaps to assist regulators in developing mindful land-use policies within western Canada's Boreal region.

This introductory chapter outlines pertinent knowledge gaps and provides essential background information to prepare the reader for subsequent chapters. It presents a number of topics, including (i) a brief description of peatlands in western Canada and their global significance (ii) natural controls on peatland greenhouse-gas emissions and general response to disturbance events, and (iii) the potential applications of quantifying seismic-line impacts on peatlands using UAV technology.

1.2 Background

Peatlands are a class of wetland which cover approximately 400 million hectares (roughly 3%) of the Earth's surface, and can be found on all continents (Wieder & Vitt, 2006). Peatlands can be loosely defined as resource- or nutrient-limited ecosystems which contain a naturally occurring surface-peat soil layer of a given thickness (>40cm in Canada; National Wetlands Working Group [NWWG], 1997; Farmer et. al., 2011; ESRD, 2015). The vast majority of peatlands occur within the Boreal Forest/Taiga biome of northern latitudes, which contain the largest soil-organic carbon stocks (Wieder & Vitt, 2006; Strack, 2008; Parish et al., 2008; Scharlemann et al., 2014). Conservative estimates, incorporating mean peat depth, predict 547 gigatons of carbon (GtC) to be currently stored within northern Boreal peatlands (Yu et. al., 2010). Due to the amount of terrestrial soil carbon stored within these northern peatlands, and the noted link between carbon release and ecosystem disturbance (Wieder & Vitt, 2006; Parish et al., 2008; Eppinga et al., 2009), it has become essential to incorporate peatland carbon-stock estimates within global climate-change models (Yu, 2012; Shi et. al., 2015). Consequently, it has become equally important to

improve the accuracy of models predicting peatland response to disturbances anticipated by climate-change models (Strack et. al., 2006).

Globally, carbon dioxide (CO_2) has been identified as the most important greenhouse gas (Bridgham et. al., 2013). However within northern Boreal peatlands, CO_2 emissions are generally low as it is produced through aerobic decomposition, and the elevated water table of these ecosystems result in primarily anaerobic conditions and CO_2 sequestration (Limpens et. al., 2008). Conversely, the resultant anoxic decomposition of organic matter generates large amounts of methane gas (CH_4): a powerful GHG having approximately 28 times the global warming potential of CO_2 (Joosten & Couwenberg, 2009; Bridgham et. al., 2013; FAO, 2014; Zhu et al., 2014). Wetlands are the largest natural source of CH_4, and previous research has identified strong links between climatic conditions and wetland methane release rates (Bridgham et. al., 2013; Turetsky et. al., 2014). As such, there is currently great interest in identifying factors which contribute to CH_4 production within wetland ecosystems (Bridgham et. al., 2013).

1.2.1 Peatlands within Canada and Alberta.

An estimated 147 million tonnes of soil carbon is thought to be stored within Canadian Boreal peatlands, accounting for 56% of organic carbon stored within all Canadian soils (Strack, 2008). Canada contains approximately 24% of the Earth's wetlands, and approximately 28% of the Earth's peatlands by land area (NWWG, 1997; Strack, 2008). The vast majority of Canada's peatlands are found within the Boreal forest region, which covers approximately 113.6 million hectares (12%) of the country's landmass, including portions of all three coastlines (Strack, 2008). Although peatlands are found throughout the Canadian Boreal forest, two major hotspots of peatlands are apparent: (i) the Hudson Bay Lowlands in eastern Canada, and (ii) the

intercontinental peatlands of interior BC, NWT, and the prairie provinces (Figure 1.1). These two areas are vastly different in climate, hydrology, chemistry, substrate, and vegetation, which has led to the evolution of dissimilar peatland complexes (Rochefort et al., 2012). Perhaps the most obvious difference between eastern and western Canadian Boreal peatlands is the presence of trees. While trees are common in western Canadian peatlands, most eastern Canadian peatlands are open, treeless ecosystems (Rochefort et al., 2012; Munir et al., 2014). Trees are sustained within western ecosystems by fairly dry climatic conditions, where potential evapotranspiration nearly equals annual precipitation measurements (Vitt & Bhatti, 2012). However, these dry conditions also lead to intermittent fire disturbances (Strack, 2008).

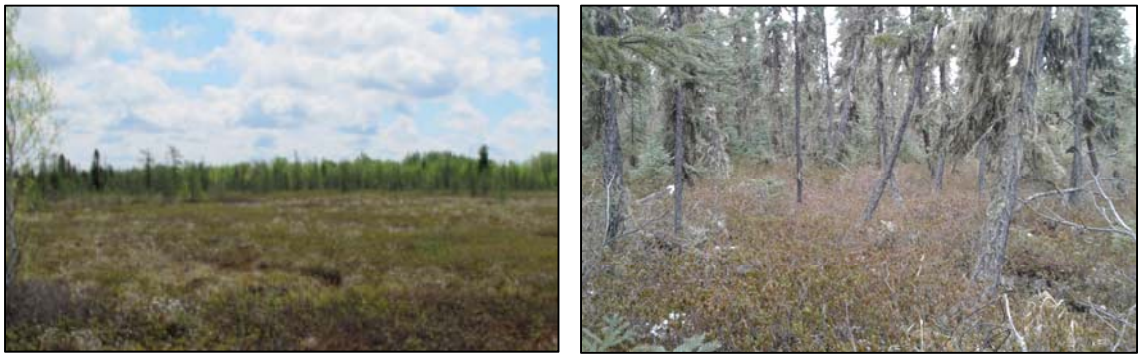

Figure 1.1: *Comparison of Mer Bleue (Left, foreground) a well-researched bog near Ottawa, Ontario (retrieved from Kalacska et al., 2013), and a view of our study site (Right) located near Peace River, Alberta. Peatlands in western Canada are capable of sustaining tree growth, as is apparent in the images.*

1.2.1.1 Peatland Microtopography.

Microtopography describes small-scale heterogeneities in ground elevation and surface structure across a peatland (Cresto Aleina et al., 2015). These features can be referred to as microforms, and are visibly identifiable when patterns become apparent, often occurring around the 1m x 1m scale (Belyea & Malmer, 2004; Eppinga et al., 2009; Cresto Aleina et al., 2015).

Although a variety of terms exist to describe microforms, two terms are consistently used in the literature: hummocks and hollows (Belyea & Malmer, 2004; Couwenberg & Joosten, 2005; Strack & Waddington, 2007; Eppinga et al., 2009; Acharya et al., 2015). Hummocks are areas where organic matter has accumulated over a relatively small spatial scale, creating a small hill in the landscape (Pouliot et al., 2011). Hollows are the opposing, low-lying areas dispersed between hummocks (Figure 1.2) (Nungesser, 2003).

Figure 1.2: *Examples of microforms. In the left pane a hollow is displayed as a hole in the surrounding vegetation and moss. In the right pane, a hummock is displayed as a clear moss mound, which rises above the surrounding peat surface. Both of these features occur at the sub-meter scale. Images were provided by project colleagues.*

Microforms have been shown to provide a variety of important environmental functions, including hydrological regulation by improving water retention within peatlands, as well as controlling spatial distribution of GHG fluxes, microclimates, and nutrient gradients (Lucieer et al., 2010; Macrae et al., 2013; FAO, 2014; Cresto Aleina et al., 2015; Acharya et al., 2015). Once established, peatland microforms may persist for decades in the landscape under equilibrium environmental conditions (Nungesser, 2003). Thus within disturbed peatlands, apparent changes

in vegetation community or microtopographic features surrounding the disturbance may be accredited to the disturbance event rather than natural factors.

The research community has yet to reach consensus on the exact combination of environmental factors responsible for peatland microform formation, distribution, and resiliency. Some sources indicate variations in soil moisture, hydroperiod, and depth to water table are primarily responsible, while others indicate that the spatial distribution of *Sphagnum* species and differences in intrinsic decomposition rates drive microform patterning (Hogg, 1993; Nungesser, 2003; Strack, 2008; Acharya et al., 2015).

1.2.1.2 Controlling Factors of Peatland Methane Emission.

Methane is generated in saturated soils under highly reduced conditions. Therefore, the rate of CH_4 emission within a peatland (flux) has been strongly linked to water-table position below the peat surface and vegetation characteristics (Belyea & Malmer, 2004; Strack & Waddington, 2007; Limpens et al., 2008; Strack, 2008; Parish et al., 2008; Farmer et al., 2011; McCarter & Price, 2012; FAO, 2014; Comas et al., 2014; Cresto Aleina et al., 2015). Peat structure is the main factor directing water-table position, and is largely controlled by the intrinsic decomposition rates of surface vegetation, which determine resultant soil porosity (Hogg, 1993; Nungesser, 2003; Belyea & Malmer, 2004; Strack & Waddington, 2007; Strack, 2008; FAO, 2014; Comas et al., 2014). Changes in soil porosity cause preferential hydrological flow patterns, ultimately creating spatial variability of water table depths across the peatland, and subsequently altering CH_4 generation and emission rates (Belyea & Malmer, 2004; Parish et al., 2008; Comas et al., 2014). Vegetation may also directly influence flux, as is the case of aerenchymous plants (ie. sedges)

which creates a direct link between the atmosphere and saturated CH_4 producing soil layers via specialized aerated roots (Couwenberg et al., 2011; Kalacska et al., 2013).

Peatland microtopography describes spatial variations in environmental conditions (temperature, surface moisture, vegetation, and nutrient availability) which can indirectly describe variability in CH_4 gas generation and release (Cresto Aleina et al., 2015). Therefore, mapping peatland microtopography is anticipated to be a key step towards understanding, and predicting, small-scale heterogeneities in peatland CH_4 emission rates.

1.2.1.3 Peatland Response to Disturbances: Seismic Lines.

Seismic lines have been used for oil and gas resource exploration by the petroleum industry since the 1950's. Initially, construction of these features involved completely clearing a low-density network of lines across the area of interest to substrate via bulldozer, with approximate widths of 8m or greater (Lee & Boutin, 2006; BC OGC, 2016). After the early 2000's, and with the introduction of 3D seismic practices, line design transitioned to favour "low-impact" seismic (LIS) construction methods via hand clearing or mulching lines with 1 to 4m widths (Lee & Boutin, 2006; Schneider & Dyer, 2006; BC OGC, 2016). However, LIS are constructed in high-density grids, with intervals on the scale of mere tens of meters, and as a result have been linked to wide-spread ecosystem fragmentation among other impacts (Schneider & Dyer, 2006; BC OGC, 2016; Pattison et al., 2016). Furthermore, a clear definition of what qualifies as a "low-impact" line has not been established in land-use regulations (BC OGC, 2016). The term currently applies to lines of varying clearing widths, orientations, and construction seasons, which is misleading as changes in these factors have been strongly linked to the likelihood of successful revegetation and habitat

restoration (Schneider & Dyer, 2006; van Rensen et al., 2015; BC OGC, 2016; Pattison et al., 2016). An example of a LIS transecting a boreal bog is provided in Figure 1.3.

Figure 1.3: *A low-impact seismic line traversing a boreal bog ecosystem in northern Alberta. This line was constructed in the late 2000s and though ground vegetation is apparent, few trees have reestablished. It is difficult to observe microtopography due to the presence of Labrador Tea. Image was provided by project partners.*

Construction of these linear features is linked with persistent changes in soil temperature, light levels, and increased soil compaction: all of which are known to influence natural recovery rates and successional trajectories (van Rensen et. al., 2015). The complete removal of micro-topography during early line construction is also associated with permanent changes in vegetation composition and altered local hydrological regimes (van Rensen et. al., 2015). Given the previously described linkages between CH_4 generation, water table position, and vegetation community, it is reasonable to expect these linear features will have an impact on peatland CH_4 emissions. Microform removal or compression and soil compaction is likely to cause decreased

ground elevation and increase overall water table position along seismic lines. Therefore, a strong case can be made for anticipating increased rates of CH_4 emission along seismic lines relative to surrounding undisturbed peatland.

Numerous studies have indicated that conventional seismic lines (those constructed from early 1950's – 2000's) are unlikely to recover to pre-disturbance conditions without active restoration efforts, particularly those which traverse lowland (peatland) areas conditions (Lee & Boutin, 2006; Schneider & Dyer, 2006; BC OGC, 2016). These lines often exist in a stalled successional state, or follow an alternative successive path to an ecosystem that is inconsistent with surroundings. In some examples, simple rewetting of peat soils is considered active restoration (Chimner et al., 2016), though a full peatland-restoration process has been developed in Canada by Quinty and Rochefort (2003). Even in cases where active restoration has occurred, predictive regression models suggest that 10 to 30 years may be required for comparable peatland microtopographic features to redevelop (Pouliot et al., 2011). While active restoration certainly does not guarantee restoration success (reported 40% occurrence of undesirable successional trajectory at 53 monitored bogs of eastern Canada), negligible (<1%) colonization of *Sphagnum* moss species has been reported in areas where active restoration was not pursued (Rochefort, 2000; Gonzalez & Rochefort, 2014). This suggests active restoration is a beneficial practice which increases chances of success.

Estimates of total seismic-line disturbances within the western Canadian Boreal region range from 300,000 km to 1.7 million km, indicating these features represent wide-reaching, long-term disruptions to the peatland ecosystems they intersect (Brandt, et. al., 2013; Pasher, Seed & Duffe, 2013). However, the majority of seismic-line research has focused on assessing the impacts

of early, “conventional” lines rather than LIS lines, due to the ability to easily identify larger lines with remote sensing (ie. Pasher, Seed & Duffe, 2013), and the ability to use these older lines to understand long-term ecosystem impacts (ie. van Rensen et al., 2015). As previously stated, LIS lines are likely to have extensive impacts due to their high-density construction, yet more research must be conducted to determine exactly how these lines are affecting ecosystems they intersect.

1.3 The Role of Remote Sensing in Modelling Peatland Ecosystems

There are currently three major platforms in remote sensing: satellite, airborne, and terrestrial. With any given platform, active sensors and passive sensors may be used to collect data. Satellite-based platforms will not be discussed in great detail, although it is important to note that although satellite imagery is improving, imagery at high enough spatial resolutions to map small-scale peatland surface features, such as microtopography, is not currently available to the scientific community (Lehmann et al., 2016). Active sensors include laser altimetry, radio detection and ranging (RADAR), and light detection and ranging (LiDAR), which work by actively emitting electromagnetic radiation pulses and receiving returns to map ground targets (Lefsky et al., 2002). Passive sensors, alternatively, refer to systems relying upon reflected or emitted radiation, using spectrometers or similar sensors to passively collect radiance data (EisenbeiS, 2009). Unlike ground surveys, aerial platforms require knowledge of external parameters (positional information) to be captured simultaneously with each data point in order to reduce dataset errors (Lefsky et al., 2002; Lejot et al., 2007). This positional information may be captured by onboard equipment, including GPS systems to locate the platform, and inertial navigation systems (INS) to determine attitude (roll, pitch and yaw) of the sensor (Lefsky et al., 2002; Lucieer et al., 2014). Alternatively, this information may be estimated from Structure from Motion (SfM) software used

in data processing. To counteract inaccuracies associated with unknown or poorly defined external parameters, ground control points (GCPs) may be used during image acquisition (Lejot et. al., 2007). GCPs are target points of known location and elevation (x,y,z collected by survey grade terrestrial GPS system) which are visible in the acquired aerial imagery (Lejot et. al., 2007). These GCPs may be used to (i) increase the accuracy of digital elevation models (DEM) and orthophotos generated from the aerial imagery when GPS and INS systems cannot be used, (ii) georeference aerial survey products to determine global location of the imaged site, and (iii) to assess the overall accuracy of the DEM and orthophotos through model validation (Lejot et. al., 2007; Turner et. al., 2012; Lucieer et. al., 2014). Similarly, knowledge of internal parameters (sensor specifications) in addition to these external parameters allow for data adjustments to determine true point locations more accurately (Lefsky et al., 2002; Lejot et al., 2007).

Aerial imagery may be collected by manned or unmanned (ie. UAVs) systems. UAVs, are remotely controlled or autonomous fixed-wing or multi-rotor drones capable of carrying a variety of sensors, including LiDAR and high-resolution digital cameras (Knoth et. al., 2013). Using the basic principles of photogrammetry (measuring geometry from photos), UAV flight plans allow for certain percentages of lateral and forward overlap across the study site (Lehmann et. al., 2016). Photographs must be assessed for quality to ensure blurred images or those with undesirable exposure conditions are removed prior to processing (Lehmann et. al., 2016). These overlapping photos can then be processed in stereoscopic pairings using commercial software packages such as Agisoft PhotoScan™, which utilize Structure from Motion (SfM) algorithms (or similar) to produce orthophotos and dense point clouds containing x,y,z information for each identified point, with corresponding global locations when georeferenced. Additional processing of the point cloud

can produce digital surface models (DSM: elevation models which include vegetation cover), digital terrain models (DTM: elevation models which exclude vegetation), canopy height models (CHM: surfaces produced by subtracting DTMs from DSMs), and orthophotos (planimetric images with relief distortion removed) (Lucieer et. al., 2014; Roosevelt, 2014). These products may be used alone or in combination to generate classified maps and other high-order information products (Lehmann, 2016).

The major strength of UAVs when compared with alternative remote-sensing systems is the ability to collect data at nearly unlimited spatial and temporal resolutions, as well as the capability to investigate potentially hazardous areas, such as active volcanoes or landslides, with reduced risk to pilots (Eisenbeiß, 2009; Lechner et. al., 2012). Additionally, multiple cost-benefit analyses comparing UAV surveys with alternative aerial surveys and ground surveys have proven UAVs to be comparable, if not economically superior (Knoth et. al., 2013; Roosevelt, 2014). For example, Roosevelt (2014) compared UAV photogrammetry (UAVP) data with RTK GNSS data of multiple archaeological sites in Turkey. The conclusions of this research indicated little difference in accuracy between the two datasets, with nearly all attributed to surface conditions (particularly vegetation) at the time of the UAVP survey (Roosevelt, 2014). However, vegetation and macrotopographic relief were also noted as impediments to ground survey accuracies (Roosevelt, 2014). Lucieer et. al. (2014) used UAVs to map the microtopography of Antarctic moss beds, reporting a geometric accuracy of 4cm for the produced orthophoto and DSM, and concluded that these high-spatial-resolution products were excellent for investigating microtopographic features and environmental relationships.

While the majority of current UAV instruments are passive sensors that are therefore unable to penetrate canopies to map ground surface in densely vegetated areas, comparisons of UAV and LiDAR topographic products indicates reasonably similar accuracies in open areas (Lefsky et. al., 2002; Mesas-Carrascosa et. al., 2014). Additionally, point clouds produced from LiDAR instruments mounted on piloted aircraft tend to have low densities (<5pts/m^2) compared to photogrammetric point clouds acquired from a UAV (100's of pts/m^2) (Sturm & Triggs, 1996; Pirotti & Tarolli, 2010). In this respect, UAV systems are more likely to capture minute differences in peatland microtopography (Knoth et. al., 2013). Furthermore, LiDAR data is usually more costly to acquire, limiting broad scale or repeated acquisitions (Knoth et. al., 2013).

Some limitations or potential concerns with UAV data for environmental monitoring purposes include: flight influences on image resolution (determined by altitude and focal length of sensor lens), reliance on good meteorological conditions for flights and high image quality, and reduced flight times resulting from battery life and payload restrictions (Lejot et. al., 2007; Fritz, Kattenborn & Koch, 2013; Chisholm et. al., 2013). In particular, distortion resulting from small focal lengths of digital cameras (ie. 35mm) operating close to the ground may be much higher in UAV data (potentially >5 pixels) when compared to traditional photogrammetric systems (airplanes or helicopter platforms) which contain larger focal lengths operating further away from the ground (Lejot et. al., 2007; Eisenbeiß, 2009).

1.3.1 Extracting Microtopographic Data.

Previous researchers have distinguished peatland hummocks and hollows from each other in terrestrial or aerial surveys through comparative assessments of topographic features, such as relative elevation and slope, as well as vegetation community characteristics and depth to water

table (Bubier et al., 1993; Eppinga et al., 2009; Hartley et al., 2015; Lehmann et al., 2016). Microform classification thresholds appears to depend on site-specific surface morphology, and researcher subjectivity. For example one study conducted within an eastern-Canadian bog identified hummocks as areas ≥20cm above the maximum water table, while other research has identified hummocks as features rising 20-50cm above surrounding hollows or the lowest reported elevation within a surveyed transect (Hogg, 1993; Bubier et al., 1993; Pouliot et al., 2011). Thus, in many cases applying elevation thresholds appears to be a simple, yet effective method for classifying (extracting) microtopography from survey data.

1.3.2 Estimating Methane Emission.

A variety of peatland models currently exist and are used to represent ecosystem-level interactions and estimate GHG emission (Wu et. al., 2010; Cresto Aleina et. al., 2015; Shi et. al., 2015). Generally, these models combine environmental information (area hydrology, climate, vegetation etc.) with point-measured gas flux, and leverage spatial data (ie. ground survey, aerial survey) to upscale flux estimates to a larger study area. One method of upscaling local flux data to a larger area is described by Wu et al. (2010) as parameter upscaling. This process involves weighting variable values by the fractional area coverage of each identified unit (Wu et. al., 2010). When considering peatland microtopography, the variable would be CH_4 emission, and individual units would refer to identified microforms (hummocks, hollows, etc.). Therefore parameter up-scaling would involve weighting CH_4 flux values reported for each microform by the areal coverage of that microform. This method of upscaling has been found to be more computationally efficient than alternate methods, though it is not anticipated to capture as much variability of the modeled variable (Wu et. al., 2010). In order to properly upscale CH_4 fluxes to the ecosystem from

microtopographic data, flux data must be collected for each identified microform class, or reasonable assumptions (such as conservative estimates) should be made in place of missing data (Lehmann et. al., 2016).

Shi et. al. (2015) included microtopographic data into a computer model designed to predict peatland hydrological responses to altered climate variables (ie. increased air temperatures). This model utilized parameter upscaling of modelled peatland microtopography (assuming 75% hummock land cover and 25% hollow land cover as determined by field observations) to estimate responses in vegetation distribution and subsurface biogeochemical processes (Shi et. al., 2015). The model was compared to half-hour field measurements of water table fluctuations over 3 years, and showed strong agreement between modelled data and field values (Shi et. al., 2015). Discussion of these results suggest that inclusion of microtopographic data is essential in accurately representing ecosystem processes (Shi et. al., 2015). Another study involved the development of a new modelling system, named the hummock-hollow (HH) model, based primarily on peatland microtopography to simulate upscaling of CH_4 hotspots and assess underestimation of CH_4 in boreal peatlands (Cresto Aleina et. al., 2015). In this case, microtopographic information was based on a ground surveys (via theolodite) of the peatland study site, with hummocks distinguished as areas reported higher than a local reference point by 20cm (Cresto Aleina et. al., 2015). The HH model was developed using historical data at a 1m x 1m grid (microform level) before upscaling to a 1km x 1km grid (peatland ecosystem level) (Cresto Aleina et. al., 2015). It was then used to predict peatland CH_4 response to air temperature increases predicted by climate-change models (Cresto Aleina et. al., 2015). Results indicated that the inclusion of microtopographic data into the GHG model improved output, compared to traditional

modelling approaches (Cresto Aleina et. al., 2015). This study called for improved peatland microtopographic-mapping techniques to allow for more accurate simulations of surface patterns, hydrology, and CH_4 hotspots (Cresto Aleina et. al., 2015).

1.4 Statement of the Problem

Approximately 16% of Alberta is covered by Boreal peatlands, many of which have been extensively disturbed by a dense network of seismic lines used to delineate valuable underlying petroleum resources (Schneider & Dyer, 2006; Webster et al., 2015). Since activities which disrupt peatland environmental conditions may trigger carbon release, the widespread disturbance of Alberta's Boreal peatlands is likely to have stimulated CH_4 emissions. However, this theory has yet to be tested, since the impact of seismic lines on Boreal peatland surface conditions and CH_4 release has never been quantified. Microtopography and depth-to-water, controlling factors on peatland CH_4 emission, can vary significantly over short distances, which makes them difficult to monitor from low-resolution imagery. However, monitoring these features via UAV platforms fitted with passive sensors is challenged by the capability of western Boreal peatlands to sustain ground-obscuring tree growth. This thesis strives to address the knowledge gaps associated with modeling seismic line impacts on Albertan Boreal peatlands.

1.5 Research Objectives

Two main objectives are addressed in this research:

1. To assess the capacity of UAV photogrammetry for modelling microtopography in complex peatland systems within Alberta by:

a. Assessing the accuracy of modelling peatland microtopography using UAV photogrammetry, and
b. Developing a method for characterizing (classifying) peatland surface morphology using UAV imagery

2. To quantify the impact of seismic lines on physical environmental parameters (microtopography and depth-to-water), and CH_4 emission, in a typical treed bog of northern Alberta

1.6 Organization of the Thesis

Efforts to satisfy these research objectives are summarized in two independent research articles, which comprise the main body of the thesis. Chapter 2 explains the suitability for UAV platforms in characterizing terrain of a complex peatland ecosystem of western Canada (Objective 1a). It addresses recommendations from numerous previous research studies calling for improved methods of estimating peatland GHG emission, through refined spatial data, by determining whether UAVs are up to this task in western Canada. Chapter 3 describes a methodology for classifying peatland microtopography (Objective 1b) and estimates CH_4 emission from the treed bog using the microtopographic surface and a complimentary depth-to-water surface (Objective 2). This chapter also presents the first-known quantification of physical and GHG-related impacts of peatland disturbance by seismic lines. Chapter 4 summarizes conclusions drawn from this research, outlines main contributions, and details potential opportunities for future research.

Chapter Two: Assessing the Value of UAV Photogrammetry for Characterizing Terrain in Complex Peatlands

2.1 Abstract

Microtopographic variability in peatlands has a strong influence on greenhouse gas fluxes, but we lack the ability to characterize terrain in these environments efficiently over large areas. To address this, we assessed the capacity of photogrammetric data acquired from an unmanned aerial vehicle (UAV or drone) to reproduce ground elevations measured in the field. In particular, we set out to evaluate the role of (i) vegetation/surface complexity and (ii) supplementary LiDAR data on results. We compared remote-sensing observations to reference measurements acquired with survey grade GPS equipment at 678 sample points, distributed across a 61 hectare treed bog in northwestern Alberta, Canada. UAV photogrammetric data were found to capture elevation with accuracies, by root mean squares error, ranging from 14–42 cm, depending on the state of vegetation/surface complexity. We judge the technology to perform well under all but the most-complex conditions, where ground visibility is hindered by thick vegetation. Supplementary LiDAR data did not improve results significantly, nor did it perform well as a stand-alone technology at the low densities typically available to researchers.

2.2 Introduction

Fine-scale variability in elevation, commonly referred to as microtopography, is an important factor in the distribution of greenhouse gas (GHG) flux across peatland ecosystems (Lucieer et al., 2010; Couwenberg et al., 2011; Macrae et al., 2013; Comas et al., 2014; FAO, 2014; Cresto Aleina et al., 2015; Acharya et al., 2015). Consequently, including microtopographic information in carbon-balance models is often recommended as a means of improving model accuracies (Strack

et al., 2006; Farmer et al., 2011; Cresto Aleina et al., 2015; Shi et al., 2015; Lehmann et al., 2016). Most commonly, microtopographic data are acquired via terrestrial surveys using real-time kinematic global navigation satellite system (RTK GNSS) equipment, which are capable of centimeter accuracies (Pouliot, Rochefort & Karofeld, 2011; Roosevelt, 2014). However, terrestrial surveys are limited by high costs and personnel requirements, and do not scale well over large areas (Roosevelt, 2014).

Recently, researchers have used photogrammetric data from unmanned aerial vehicles (UAVs) to acquire detailed microtopographic data in a variety of terrestrial settings, suggesting that the technology might provide an attractive alternative to traditional ground surveys in peatlands. Using standard consumer-grade cameras, UAVs can produce high-density point clouds (100 s of points per m^2) and ultra-high resolution orthomosaics with modern photogrammetry principles and structure from motion (SfM) computer-vision software (Sturm & Trigs, 1996). Roosevelt et al. (2014) found UAV photogrammetry to be one order of magnitude more labor-efficient and at least two orders of magnitude more detailed (in terms of data density) than RTK GNSS surveys for microtopographic archaeology surveys in western Turkey. Working in gently sloping, sparsely vegetated hills interspersed with olive orchards, the authors reported vertical root mean squares error (RMSE) values of 21 cm compared to ground control points (GCPs). Lucieer et al. (2014) reported even better RMSE accuracies of 4 cm in microtopographic surveys of East Antarctic moss beds with UAV photogrammetry. Using an alternative multispectral approach, Lehmann et al. (2016) classified vegetation species and microforms with high accuracy (>80%) using UAV-derived color infrared (CIR) imagery of a South Patagonian peatland. While this

research did not make use of photogrammetric elevation data, the authors suggested that doing so would have increased classification accuracies even further (Lehmann et al., 2016).

Building on these promising early studies, there is a need to evaluate the performance of UAV photogrammetry in other, more complex environments. The peatlands of the boreal zone contain globally significant carbon stocks, and are an essential target for climate-change studies (Strack, 2008, Munir et al., 2014). However, terrain modeling in these environments is expected to be more challenging for UAV photogrammetry, given the complexity of the surfaces and the presence of vascular vegetation, both of which can negatively affect the performance of SfM workflows. For example, Javernick, Brasington & Caruso (2014) assessed photogrammetric point clouds from UAVs for modelling the topography of a shallow braided river in New Zealand, and found vegetation cover to negatively affect results. Vertical accuracies fell from 17 cm (RMSE) in bare areas to 78 cm in areas of vegetation, due to the inconsistent ability of passive photography to penetrate the vegetation canopy (Javernick, Brasington & Caruso, 2014). Similarly, elevated wind speeds have been shown to decrease UAV data quality in vegetated areas due to movement of the canopy surface (increased photo blurriness), and interference with UAV positioning and orientation during image capture (Jensen & Mathews, 2016; Zainuddin et al., 2016). In some cases, this effect can be severe. For example, Zainuddin et al. (2016) found excessive tree leaf movement due to strong winds during UAV data acquisition caused ten trees to be completely missed in the produced point cloud, and increased uncertainty in ground surface elevations around modeled trees. This ultimately resulted in a poor quality, and non-useful 3D model for estimating canopy heights (69.6 cm RMSE; Zainuddin et al., 2016).

Additional challenges associated with elevation changes, presence of standing water and image-texture homogeneity have also been noted in the literature. For example, Mancini et al. (2013) compared UAV point clouds from passive photogrammetry to those derived from a terrestrial light detection and ranging (LiDAR) scanning system, an active (laser) technology, over sand dunes in Italy. The authors found photogrammetric point density to decrease in flat bare areas, due to the inability of the SfM feature-matching algorithm to reliably identify tie points. Areas of dense vegetation were excluded from this assessment, though sparse vegetation (15- to 20-cm patches) were included in the linearly interpolated DSM surfaces and reportedly influenced overall accuracy (11 cm RMSE; Mancini et al., 2013). Similar results have been reported in areas of standing water, where the surface is too homogenous to accurately locate tie points, or where variations in reflectance across the water surface cause SfM algorithms to incorrectly estimate point locations (Rosnell & Honkavaara, 2012; James & Robson, 2012).

One potentially promising strategy involves combining passive photogrammetric data (high point density, but limited canopy penetrating abilities) with airborne LiDAR, which typically has lower densities but an enhanced capacity to penetrate vegetation. LiDAR has proven to be highly accurate in estimating ground surface elevations within bare, flat areas (Lefsky et al., 2002; Pirotti & Tarolli, 2010), though canopy interference and low point densities are likely to decrease estimated surface accuracies in more complex environments. However, these data have yet to be widely assessed in a peatlands context.

The goal of this research is to assess the value of UAV photogrammetry for characterizing terrain in vegetated peatlands in the Canadian boreal forest. In this study, we worked in a treed-bog ecosystem in North-West Alberta, Canada that displayed a wide range of complexity, from

relatively flat, open areas to a mixture of highly undulating and treed zones. Our objective was to assess the accuracy of photogrammetric point clouds for capturing terrain elevation under a variety of vegetation/surface-complexity conditions, paving the way for future work aimed at classifying peatland microtopographic landforms (hummocks and hollows). In addition, we also assessed the value of supplementary LiDAR data over the same gradient of complexity. To achieve these objectives, we created three-dimensional point clouds from three different remote sensing data sets: (i) UAV photogrammetry; (ii) LiDAR; and (iii) merged UAV photogrammetry + LiDAR. The accuracy of these data sets was assessed using terrestrial surveys conducted in the field.

2.3 Materials and Methods

2.3.1. Study Area.

The study site is a 61-hectare section of treed bog located approximately 35 km northeast of Peace River, Alberta, Canada (Figure 2.1). The site is a mixture of open bog, mostly covered by mosses and lichens (e.g., *Sphagnum* mosses, big red stem moss (*Pleurozium schreberi*), stair step moss (*Hylocomium splendens*), fairy's puke (*lcmadophila ericetorum*), and reindeer lichens (*Cladina stellaris*, *C. rangiferina, C. mitis*)), shrubby bog with dispersed to moderately dense shrubs (e.g., Labrador tea (*Rhododendron groenlandicum*) and Lignonberry (*Vaccinium vitis-idaea*)), and moderately dense treed bog dominated by black spruce (*Picea mariana*). In the few marginal fen-like areas, tamarack (*Larix laricina*) and willow (*Salix spp.*) are present. Upland areas are dominated by mixed forest including balsam poplar (*Populus balsamifera*), trembling aspen (*Populus tremuloides*) and white spruce (*Picea glauca*). Black spruce, the dominant tree species in boreal bog ecosystems, do generally not produce large-diameter canopies. However, these trees

are dense enough in some portions of our study site to obscure the ground surface from passive sensors, as are shrubby vegetation cover types such as Labrador tea.

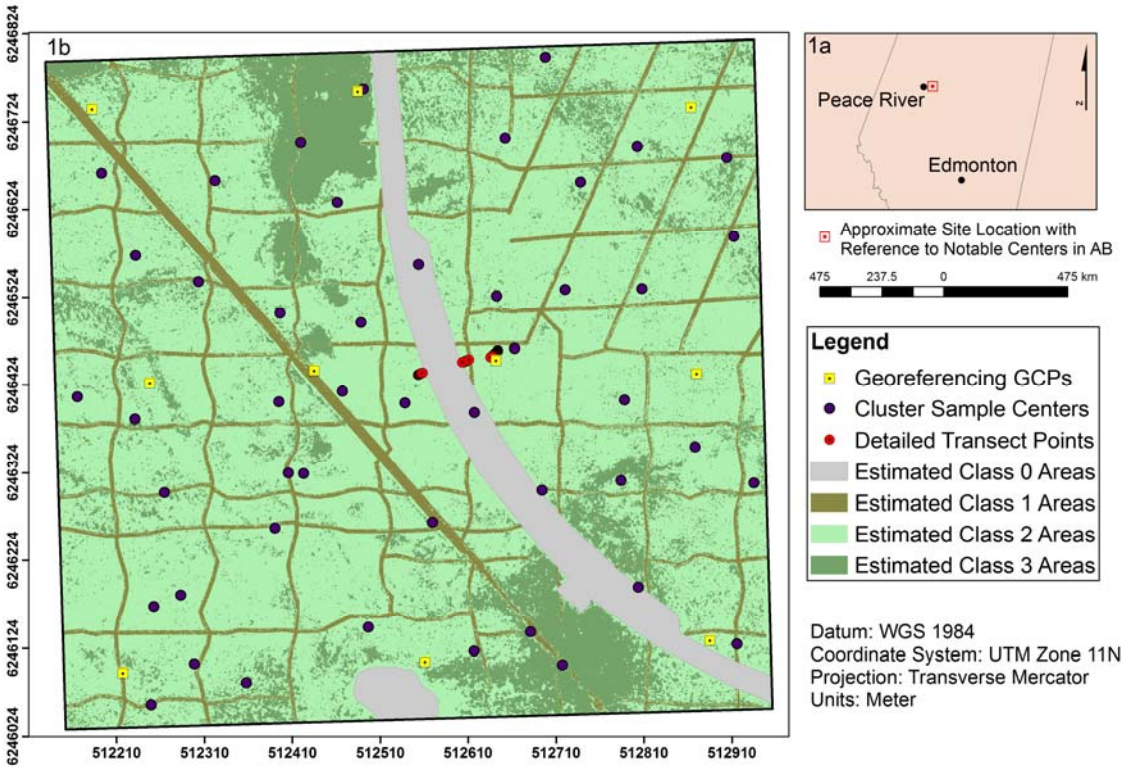

Figure 2.1: *Approximate site location in the province of Alberta (AB) with reference to nearby notable city centers (1a); estimated distribution of surface complexity classes across the study site (1b). An extensive network of linear disturbances transect the site. Areas between these features are assumed to be undisturbed and indicative of natural boreal treed bog conditions within the region. GCP installation locations, cluster sample and detailed transect points are shown (1b), and described in Section 2.3.2.1.*

Microforms (hummocks and hollows) are well established in undisturbed bog portions of the study area, and generally occur at scales between 30 and 100 cm. However, a network of linear disturbances, including seismic lines, a pipeline right-of-way (ROW), and a roadway, also transect the site.

For the purpose of this research, we stratified the study area into four classes of surface complexity, based upon visual observations of the site conditions: tree cover, anticipated surface irregularity (roughness), and visual homogeneity. The four classes were defined as: 0. Bare Areas; 1. Low Complexity; 2. Moderate Complexity; and 3. High Complexity. An example of each class is provided in Figure 2.2. Class 0 (Figure 2.2a) exclusively describes the newly constructed roadway and large south pond; Class 1 (Figure 2.2b) represents linear disturbances within the bog; Class 2 (Figure 2.2c) includes sparsely treed, undisturbed portions of the bog; and Class 3 (Figure 2.2d) represents more densely treed areas of undisturbed bog and upland zones.

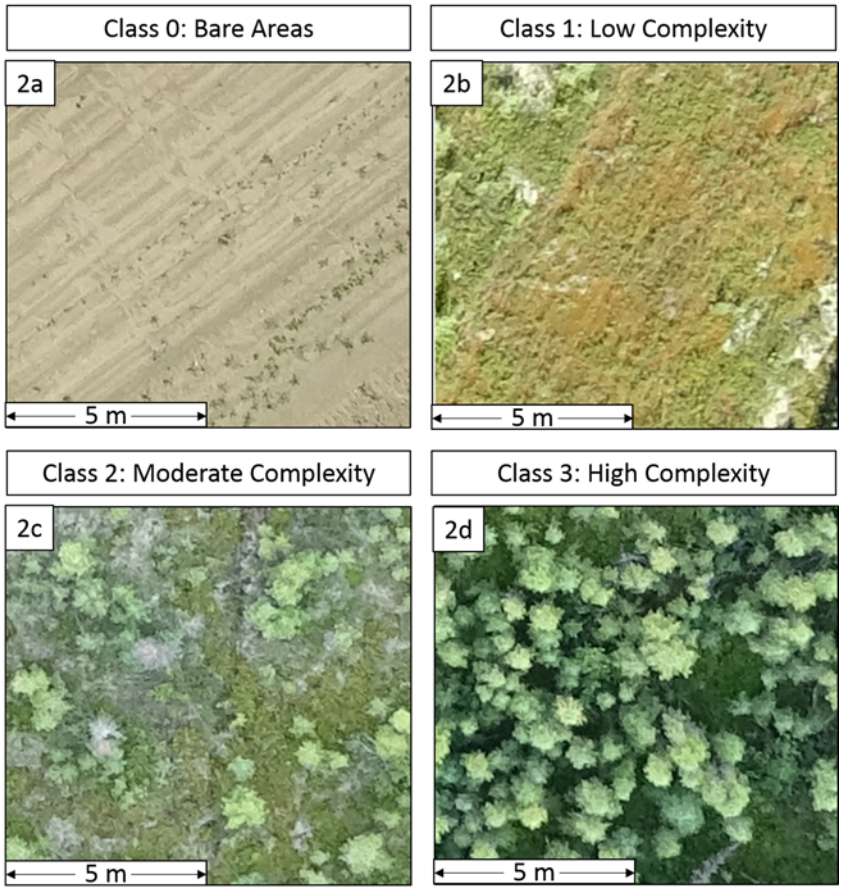

Figure 2.2: *Examples of each surface complexity class found within the study site. Data displayed is captured from the orthophoto. The example of Class 0 (2.2a) is taken from the new*

clay road bisecting the study area, Class 1 (2.2b) is taken from a pipeline ROW, Class 2 (2.2c) is from undisturbed portions of the bog, and Class 3 (2.2d) is from densely treed portion of bog.

The spatial distribution of surface complexity classes across the study area is displayed in Figure 2.1b. The approximate areal coverage of each class is estimated as following: Class 0—5%; Class 1—43%; Class 2—36%; and Class 3—16%. Although, Class 0 areas do not occur in naturally peatland ecosystems, including these points in the assessment serves as a baseline for investigating the effects of surface complexity on point cloud accuracy.

2.3.2. Data Sets.

Two types of data were acquired for this study: terrestrial surveys and remote sensing observations. Descriptions of the assembly and handling of these data are provided in the following sections.

2.3.2.1. Terrestrial Surveys.

Terrestrial ground surveys were used to assess the capacity of remote sensing to characterize terrain within the study area. A total of 678 points were acquired for this purpose, including 474 from cluster sampling and 204 from systematic transects. Cluster samples were acquired around 48 locations distributed randomly across the study area (Figure 2.1b). Cluster centers were marked with visible targets that served as ground-control point (GCP) locations for the UAV flights (described below), and so were positioned in locations visible to the sky. As a result, field crews occasionally moved cluster centers up to several meters from their randomly assigned locations. Around each cluster center, field crews surveyed between 6 and 12 points on

representative high points (hummocks) and low points (hollows) of terrain, regardless of visibility to the sky.

Additional terrestrial survey points were acquired along three ~10 m transects: two located near the access road and a third in an undisturbed location away from the road (Figure 2.1b). On these transects, ground elevations were recorded systematically at 10-cm intervals. Visibility to the sky was not a factor in selecting or surveying these transects. All terrestrial surveys were conducted with a Trimble R4 RTK GNSS system with a base station set up on a nearby survey monument. Average horizontal (x, y) and vertical (z) errors for terrestrial surveys was 0.87 cm and 1.47 cm, respectively.

2.3.2.2. Remote Sensing Observations.

2.3.2.2a UAV Photogrammetry.

Due to persistent full sun conditions, and third-party UAV operator time limitations which prevented early morning or late evening flights, UAV data were collected in two flights on July 13th and 14th, 2016. The first flight was completed in the late afternoon (approximately between 5:00 and 7:00 p.m.) on July 13th and the second in the mid-morning (approximately between 9:00 and 11:00 a.m.) of July 14th. The purpose of conducting two flights was to reduce impacts of deep shadows by collecting complimentary site data with opposing shadow angles, and subsequently using both datasets in point cloud production. Flight data was collected using an Aeryon Scout multirotor platform carrying an HDZoom30 20-megapixel optical camera with global shutter, and approximately 25 min flight duration per battery (3 batteries required to complete flight plan). Moderate average wind speeds were reported for the duration of flight operations (4 m/s on July 13th and 2 m/s on July 14th), and were determined to be acceptable for flight operations as per

UAV specifications reported by UAV Geomatics (wind limit of 13.9 m/s) and previous research findings (UAV Geomatics, 2011; Rosnell & Honkavaara, 2012). All flights were conducted at 110 m altitude, with a ground-sample distance of 2 cm or less. Parallel flight lines were configured across the site to generate 80% endlap and 60% sidelap amongst individual photos, and photos were obtained in movement (4 m/s flight speed) to minimize the number of required battery replacements.

Ground control was provided by ten permanent GCPs distributed systematically across the study area, and 48 additional GCPs distributed randomly (Figure 2.1b). As described in Section 2.3.2.1, these 48 additional GCPs also served as the cluster-center locations for terrestrial surveys. All GCPs were surveyed with the same RTK GNSS system described previously.

Raw UAV photographs were processed using Agisoft PhotoScan (Agisoft PhotoScan Professional Edition, 2016) to generate a dense point cloud (DPC) and digital orthophotography. In the first step, photo quality was assessed with the Agisoft Photoscan photo-quality assessment tool to determine whether low quality photos (<0.5) existed. From this assessment, all photos were determined to exceed this threshold (reporting > 0.66) and were therefore included in the dataset. Photos were then aligned using camera positions estimated by the onboard GPS during flight, and adjusted with the 10 permanent GCPs in the photos. The sparse point cloud generated through this alignment process was then optimized, with high-error tie points removed, prior to generating a dense point cloud and orthophoto mosaic.

Ground points (i.e., not vegetation) were extracted from the UAV DPC using a combination of LAStools (Isenburg, 2016) and Cloud Compare (CloudCompare, 2016) software. Cloud Compare is an open-source software package designed specifically for point-cloud

processing, and contains significant outlier-removal and noise-filtering tools which we found to work well with photogrammetric data. We used LAStools to perform general tasks such as initial noise filtering, classifying, and merging datasets. This workflow is summarized in Figure 2.3.

The classified ground DPC (gDPC) was edited manually to remove outliers that had been missed in the automatic filtering process. Point density of the resultant gDPC was calculated at 84.68 pts/m^2, although coverage was not uniform across the site and data gaps existed in areas of dense canopy cover. Average point spacing was 13 cm, with a total of 36,880,406 points in the cloud.

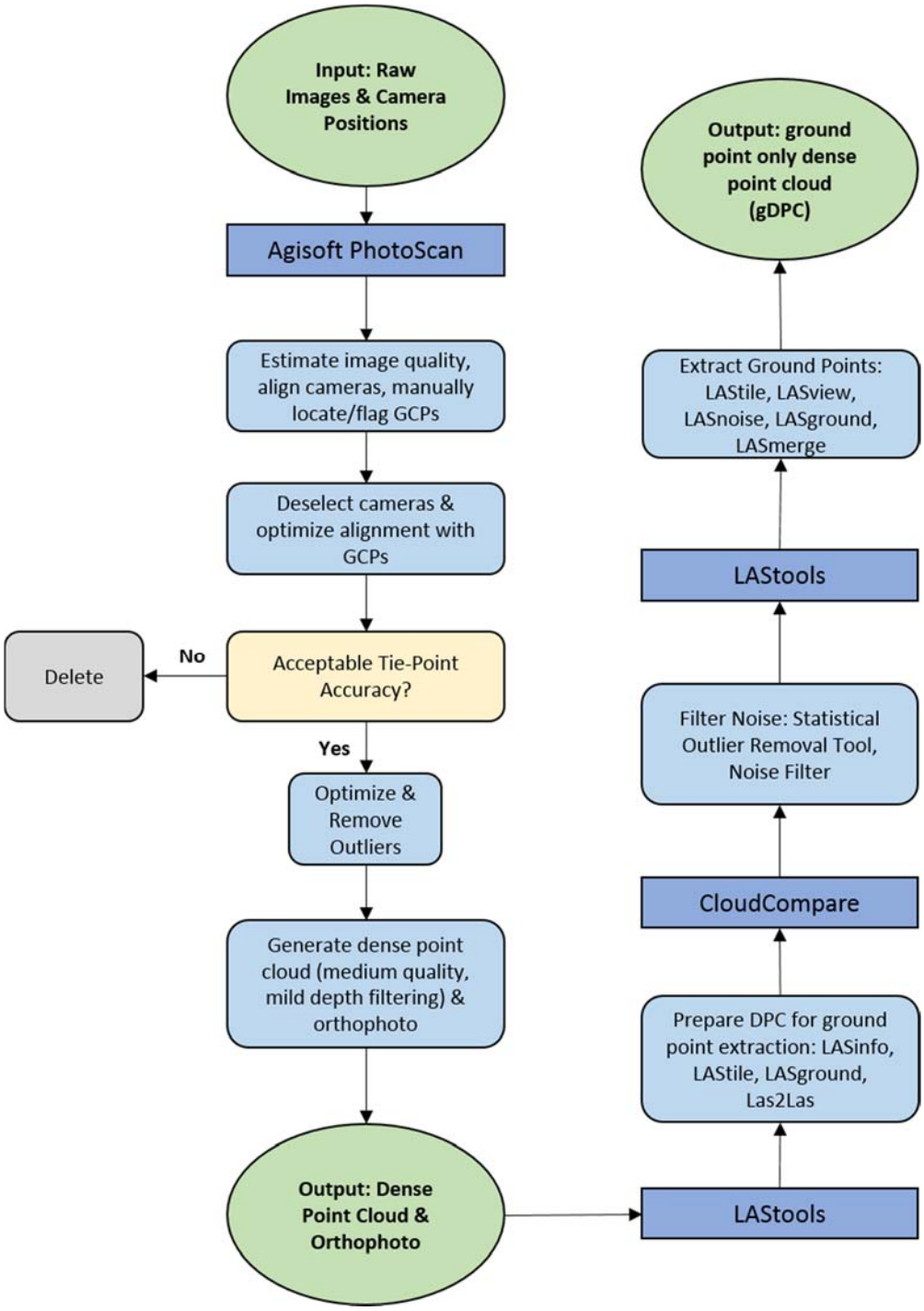

Figure 2.3: *Photogrammetric and point-cloud management software workflow illustrating the process of using UAV flight data to generate secondary (DPC and orthomosaic) and tertiary products (ground dense point cloud (gDPC)) used in this research.*

2.3.2.2b LiDAR.

LiDAR for the area was commissioned by Shell Canada and collected, processed, and calibrated by Airborne Imaging in May of 2013. This data was provided to the researchers in LAS format for use in this project. Raw point density of this dataset was reported as 4 pts/m^2. While we acknowledge the temporal disconnect between the LiDAR data (2013) and those of the UAV and terrestrial surveys (2016), we assume that the terrain elevations, which are the focus of this study, remained constant across this time period.

LAStools was used to classify ground points (ASPRS Class 02) from the raw point cloud (overall classification accuracy 96%), and remove noise from LiDAR data. The point density of the processed data was 2.88 pts/m^2, with approximate point spacing of 0.59 m and a total of 1,731,506 points.

2.3.2.2c Merged UAV Photogrammetry + LiDAR.

A combined UAV photogrammetry + LiDAR dataset was generated by merging the UAV gDPC with the ground points classified from LiDAR using LASmerge. While LiDAR clearly had lower overall point densities than the UAV dataset, it was found to have more consistent data coverage across the site, including densely vegetated areas which corresponded with (sometimes large) gaps in the UAV data. Therefore, the purpose of generating this combined dataset was to determine whether point cloud performance could be improved by using the LiDAR to fill these gaps.

2.3.3. Accuracy Assessments.

The capacity of the three remote sensing data sets—(i) UAV photogrammetry; (ii) LiDAR; and (iii) merged UAV photogrammetry + LiDAR—to capture terrain across the study area was asssessed using all appropriate terrestrial-survey points, stratified across the four classes of complexity described in Section 2.3.2.2.a.

2.3.3.1. UAV Photogrammetry Dataset Performance.

A total of 19 GCPs were used to assess the overall accuracy of the dense photogrammetry point cloud (pre-gDPC generation). GCP location and elevation values estimated by PhotoScan were compared with those collected by RTK to determine overall location accuracy (x, y, and z). The comparison of RTK vs reported PhotoScan GCP locations (x, y, z) returned RMSE values of 4 cm, 8 cm, and 13 cm, respectively. These high accuracies were corroborated by mean offset (8 cm) measurements made from the orthophoto.

A rigorous evaluation of terrain accuracy (gDCP) was assessed in two ways; first through comparision of the dataset with all 678 RTK control points, and second by comparing the dataset with with control points stratified by the four classes of surface complexity. Accuracy was determined as the difference between RTK survey point elevations and the nearest point value in the gDCP dataset ($\mathrm{gDCP}(z) - \mathrm{RTK}(z)$).

2.3.3.2. Supplemented LiDAR Performance.

The performance of the LiDAR and supplemented UAV photogrammetry+LiDAR datasets were assessed in the same manner as that described for the UAV photogrammetry data (Section 2.3.3.1 above). Firstly, all suitable RTK points (629 total) were used to assess the overall accuracy,

followed by a second assessment of points classified by surface complexity. However, no points were identified in Class 0, since the LiDAR data pre-dated road construction and no alternative bare areas (Class 0) were available. Therefore, we only preformed stratified accuracy assessment for three classes of surface complexity: Low (1); Moderate (2); and High (3).

LiDAR horizontal (x, y) accuracy and vertical (z) accuracy (on flat, hard surfaces) were reported by the acquisition company to be 30 cm and 10 cm, respectively.

2.3.4. Statistical Analysis.

Following the example of previous studies (Harwin & Lucieer, 2012; Turner, Lucieer & Watson, 2012; Lucieer et al., 2014; Mercer & Westbrook, 2016), we measured the accuracy and precision of each dataset with root mean squares error (RMSE), average absolute error, mean error, median error, and median offset (the difference between dataset medians).

Since the variance and sample sizes were unequal within the UAV photogrammetry dataset, a robust one-way analysis of variance (ANOVA) and Welch's test were conducted in SPSS software to determine whether significant differences existed between classes of surface complexity ($\alpha = 0.05$). Following this, a Tamhane pairwise comparison was conducted to determine where significant differences existed. All results were corroborated by a non-parametric Kruskal-Wallis test.

A two-way mixed model ANOVA test ($\alpha = 0.05$) was conducted on the UAV Photogrammetry and UAV Photogrammetry + LiDAR datasets in SPSS software to determine whether performance was significantly different between classes and between datasets. Based upon these results, a pairwise comparison was not deemed necessary. A second two-way mixed-model ANOVA test ($\alpha = 0.05$) was conducted on all three datasets (UAV photogrammetry,

LiDAR, and UAV photogrammetry + LiDAR) to determine whether statistically significant differences existed between classes, and between datasets. A subsequent pairwise comparison with a Bonferroni adjustment was used to determine where specific significant differences occurred.

2.4 Results

Tables 1 and 2 summarize the results of the elevation accuracy assessments. Table 2 presents dataset performance across all suitable RTK points, while Table 2 shows elevation accuracies of points stratified by surface complexity. There was no statistically significant difference ($F(1, 625) = 0.130$, $p = 0.718$) between the overall (unstratified) results obtained by UAV photogrammetry (average absolute error 31 cm, mean error 27 cm, and RMSE 40 cm), and the 'enhanced' UAV photogrammetry + LiDAR dataset (average absolute error 30 cm, mean error 27 cm, and RMSE 38 cm). However, LiDAR data alone (average absolute error 42 cm, mean error 41 cm, and RMSE 84 cm) performed significantly worse overall ($F(1, 625) = 6.041$, $p = 0.014$). All three data sources displayed positive median offsets: 23 cm for UAV photogrammetry, 27 cm for UAV photogrammetry + LiDAR, and 47 cm for LiDAR alone.

Table 2.1. Dataset Accuracies: Comparison of Dataset Elevations against all RTK Surveyed Point Elevations (678 UAV Photogrammetry dataset and 629 LiDAR and UAV photogrammetry + LiDAR datasets).

Dataset	Avg ABS z Error (cm)	Mean z Error (cm)	RMSE (cm)	Median z Error (cm)	Median z Offset (cm)
UAV Photogrammetry	31	27	40	25	23
LiDAR	42	41	84	25	47
UAV Photogrammetry + LiDAR	30	27	38	25	27

Table 2.2. Dataset Accuracies: Comparison of Dataset Elevations against RTK Point Elevations Classified by Surface Complexity.

Class	Dataset	Avg ABS z Error (cm)	Mean Error (cm)	RMSE (cm)	Median z Error (cm)	Median z Offset (cm)
Class 0 (42 points)	UAV	14	−1	15	−8	−10
Class 1 (53 points)	UAV	21	15	26	15	−10
	LiDAR	14	12	18	10	−1
	UAV + LiDAR	20	14	25	14	−6
Class 2 (264 points)	UAV	23	21	28	20	15
	LiDAR	34	33	68	23	33
	UAV + LiDAR	23	21	27	20	15
Class 3 (312 points)	UAV	42	37	51	35	47
	LiDAR	58	56	110	29	56
	UAV + LiDAR	39	35	47	32	46

This same relative pattern—no significant difference between UAV photogrammetry alone and UAV photogrammetry + LiDAR ($F(2, 625) = 2.292$, $p = 0.102$); significantly worse performance by LiDAR data alone ($F(1, 625) = 6.041$, $p = 0.014$) was also observed in the stratified results (Table 3), and we also observed a statistically significant class effect ($F(2, 625) = 22.924$, $p < 0.001$). Predictably, errors were found to increase with surface complexity, with the best results found in Class 0 (average absolute error 14 cm, mean error −1 cm, and RMSE 15 cm for UAV photogrammetry), and the worst found in Class 3 (average absolute error 42 cm, mean error 37 cm, and RMSE 51 cm for UAV photogrammetry).

Looking specifically at the UAV photogrammetry data, significant differences could be observed amongst surface-complexity classes (ANOVA: $F(3, 674) = 36.969$, $p < 0.001$, Welch: $F(3, 134.225) = 53.185$, $p < 0.001$). A post-hoc Tamhane pairwise comparison ($\alpha = 0.05$) revealed that the performance of these data in Classes 0 and 3 were significantly different from other classes

(all $p < 0.001$), while Classes 1 and 2 performed statistically the same ($p = 0.381$). A non-parametric Kruskal-Wallis test corroborated these findings.

2.5 Discussion

We found UAV photogrammetry to perform better than LiDAR in the task of characterizing terrain across our study site, suggesting that the superior point densities delivered by UAV photogrammetry are more important than the enhanced canopy penetrating abilities of LiDAR. While both technologies tended to over-estimate terrain elevation, we found photogrammetric point clouds to be better able to track microtopographic variability (Figure 2.4). 'Enhancing' photogrammetric datasets with LiDAR does not appear to be worth the increased technical and financial costs.

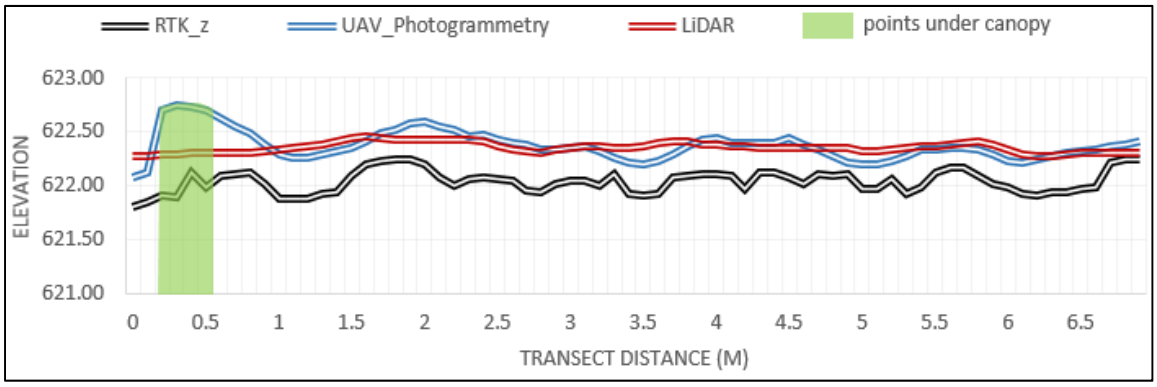

Figure 2.4: *A comparison of dataset performance along a detailed transect within an undisturbed portion of the study site (representing a mixture of Classes 2 and 3). Both UAV photogrammetry and LiDAR overestimate 'true' ground-surface elevation, represented in black, though UAV photogrammetry is better-able to capture microtopographic variability. The area in green indicates ground points that were fully covered by vegetation canopy.*

While the overall errors reported for UAV photogrammetry data (40 cm RMSE) are nominally worse than those reported by other researchers (21 cm from Roosevelt (2014); 4 cm from Lucieer et al. (2014)) we found significant variability amongst surface-complexity classes.

Areas of high complexity (Class 3) were found to perform significantly worse than other classes, whose accuracy statistics were more in line with previously published values (Class 0—14 cm; Class 1—21 cm; and Class 2—23 cm). The observation that UAV photogrammetry performed the same across the low and moderate categories of peatland complexity (Classes 1 and 2), suggests that this technology is suitable for characterizing terrain under all but the most-complex conditions. The errors we observed in Class 1 and Class 2 are generally below the scale of microforms (25 cm up to 1 m) across the site, and are therefore likely suitable for mapping microtopography. The fact that highly complex Class 3 areas were relatively rare in our study site—16% of the area as compared to 79% for Classes 1 and 2—lends even further confidence to the notion that UAV photogrammetry can be used to characterize topography in treed bogs such as the one assessed here.

The reduced performance of UAV photogrammetry in highly complex (i.e., heavily treed) areas can be partially explained by the decrease in point density on these sites: 77.5 pts/m^2 overall compared to 86.7 pts/m^2, 81.3 pts.m^2, and 91.6 pts/m^2 for Classes 0, 1, and 2, respectively. There are many more 'data holes' in these areas as well (Figure 2.5), reflecting the inability of passive photography to reliably penetrate thick canopies (Javernick, Brasington & Caruso, 2014). We had thought that these difficult conditions would be assisted by supplementary LiDAR; this turned out not to be the case in our study site. Not only did UAV photogrammetry + LiDAR fail to perform significantly better than UAV photogrammetry alone in this class (47 cm RMSE vs. 51 cm), but LiDAR data on its own was the worst-performing dataset in Class 3 (58 cm RMSE). While LiDAR is capable of penetrating vegetation canopies to a certain degree, ground point collection is still influenced by vegetation cover (Lefsky et al., 2002; Hopkinson et al., 2005; Chasmer, Hopkinson

& Treitz, 2006), and the point density is far too low overall to accurately capture microtopographic variability (Figure 2.5).

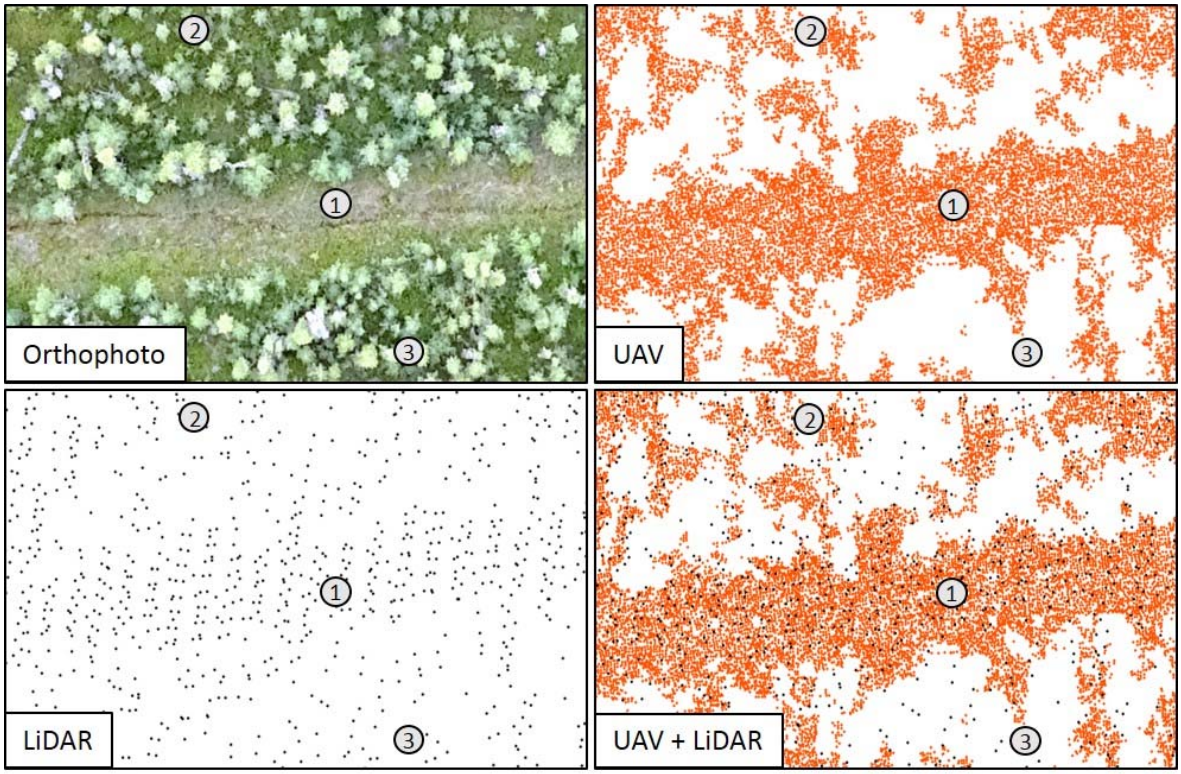

Figure 2.5: *Comparison of vegetation influence on dataset point densities, modeling a seismic line and adjacent undisturbed peatland. Examples of each surface complexity class indicated as: ① = Class 1 (low); ② = Class 2 (moderate); ③ = Class 3 (high).*

While UAV photogrammetry alone is capable of mapping most treed-bog terrain at acceptable levels of accuracy, its spatial coverage is limited: typically less than 100 ha for UAV platforms, which must fly within visible line of sight. While airborne LiDAR can cover larger areas, it is more expensive to fly, and typically not acquired at point densities sufficient for mapping peatland microtopography. We did not test high-density LiDAR, but our observations suggest that densities would have to exceed 30–50 pts/m^2 in order to be effective at this task.

Potential Sources of Error.

All data used in this research are subject to a variety of error sources during collection, processing, and analysis. Firstly, the RTK GNSS system is subject to errors introduced by satellite and radio link connectivity, which is reliant upon external factors such as canopy cover (Roosevelt, 2014), and differences in measurement techniques between field personnel. In order to mitigate these errors, survey summaries were reviewed to ensure RTK points used in the comparisons were reported at accuracies reasonable for microform scale (<20 cm). Additionally, we maintained consistency in field personnel to reduce errors in ground measurements.

UAV photogrammetry data may be compromised by external factors such as flight and weather conditions. To offset these sources of error, multiple flights were conducted to address deep shadows resulting from full sun conditions, as described in Section 2.3.2.2.a. Additionally, flights were completed in low to moderate wind (<4 m/s) and dry conditions (little to no standing water and/or moisture present at surface in vegetated areas) to reduce errors associated with these factors. Standing water was observed along the newly constructed roadway, which may have increased errors associated with Class 0 areas. However, as Class 0 areas do not occur naturally within peatland ecosystems, correcting for this source of error was not deemed a priority. Increased overlap may have improved overall model accuracies in areas of highly complex terrain, and should be considered in similar future studies. The distribution and number of GCPs was determined to be adequate for the study area, and not a major anticipated source of error, as ten GCPs per km^2 is a well-established standard in aerial photogrammetry (Krauss, 1997; McGlone, Mikhail & Bethel, 2004).

2.6 Conclusions

The primary objective of this research was to evaluate the capacity of UAV photogrammetry to characterize terrain elevation in a boreal treed bog across four categories of vegetation/surface complexity: bare, low, medium, and high. Photogrammetric data were found to perform well under all but the worst (heavily treed) conditions, with RMSE accuracies ranging from 14–23 cm. Based on this assessment, we suggest that UAV photogrammetric technology provides a reasonable foundation for supplementing or even replacing traditional RTK GNSS ground surveys for characterizing peatland terrain in low- and moderately complex conditions. While positive elevation offsets can be expected to occur, the high point density provided by this technology is generally capable of tracking microtopographic terrain undulations. This capacity can be expected to diminish (we documented 42 cm RMSE) in areas of high surface complexity due to the inability of passive photography to reliably penetrate thick vegetation canopies. As a result, site conditions should be considered carefully prior to adopting this technology in peatland-terrain-mapping applications, and researchers should determine whether or not the anticipated accuracies will meet the intended purpose.

We also assessed the value of supplementary LiDAR over the same gradient of complexity, anticipating that the enhanced canopy penetrating capacity of this technology might work well with the enhanced point densities provided by photogrammetry. However, we found no support for this concept, suggesting the type of low-density (ours was 2.88 pts/m^2) LiDAR data typically available to researchers is not worth the increased technical and financial costs.

Peatlands are highly diverse, and we would encourage additional studies aimed at characterizing terrain at other study areas, and under different conditions. In particular, it would be interesting to

assess the impact of phenological condition (leaf-on, leaf-off), shadow, and atmospheric effects on UAV photogrammetry. The capacity of the technology seems tightly tied to the ability to photograph the ground reliably. Moving from general terrain characterization (spot elevations) to true microtopographic mapping (classifying hummocks and hollows) is another logical next step.

2.7 References

Acharya, S., Kaplan, D.A., Casey, S., Cohen, M.J., & Jawitz, J.W. (2015). Coupled local facilitation and global hydrologic inhibition drive landscape geometry in a patterned peatland. *Hydrological Earth System Science*, *19*, 2133–2144.

AgiSoft PhotoScan Professional Edition (Version 1.2.4) [Software]. 2016. Available online: http://www.agisoft.com/downloads/installer/ (accessed on 3 June 2016).

Chasmer, L., Hopkinson, C., and P. Treitz. (2006). Investigating laser pulse penetration through a conifer canopy by integrating airborne and terrestrial lidar. Canadian Journal of Remote Sensing, 32 (2), 116-125.

CloudCompare (Version 2.7.0) [GPL Software]. 2016. Available online: http://www.cloudcompare.org/

Comas, X., Kettridge, N., Binley, A., Slater, L., Parsekian, A., Baird, A.J., Strack, M. and J.M. Waddington. (2014) The effect of peat structure on the spatial distribution of biogenic gases within bogs. Hydrological Processes, 28 (22), 5483-5494.

Couwenberg et. al. (2011) Assessing greenhouse gas emissions from peatlands using vegetation as a proxy, Hydrobiologia, 674, 67-89.

Cresto Aleina, F., Runkle, R.K., Kleinen, T., Kutzbach, L., Schneider, J., and V. Brovkin. (2015). Modeling micro-topographic controls on boreal peatland hydrology and methane fluxes. Biogeosciences, 12, 5689-5704.

Farmer, J., Matthews, R., Smith, J.U., Smith, P. and B.K. Singh. (2011). Assessing existing peatland models for their applicability for modelling greenhouse gas emissions from tropical peat soils. Current Opinion in Enviornmental Sustainability, 3, 339-349.

Food and Agriculture Organization of the United Nations (FAO). (2014). Towards climate-responsible peatlands management. Retrieved from http://www.fao.org/3/a-i4029e.pdf

Harwin, S., and Lucieer, A. (2012). Assessing the accuracy of georeferenced point clouds produced via multi-view stereopsis from unmanned aerial vehicle (UAV) imagery. Remote Sensing, 4, 1573-1599.

Hopkinson, C., Chasmer, L., Sass, G., Creed, I. F., Sitar M., Kalbfleisch, W., & Treitz, P. (2005) Vegetation class dependent errors in lidar ground elevation and canopy height

estimates in a boreal wetland environment. Canadian Journal of Remote Sensing, 31 (2). 191-206.

Isenburg, M. LAStools—Efficient LiDAR Processing Software (Version 160110, Licensed) [Software]. 2016. Available online: http://rapidlasso.com/LAStools/

James, M., & Robson, S. (2012). Straightforward reconstruction of 3D surfaces and topography with a camera: Accuracy and geoscience application. *Journal of Geophysical Research,* 117, doi:10.1029/2011JF002289.

Javernick, L., Brasington, J., and Caruso, B. (2014). Modeling the topography of shallow braided rivers using Structure-from-Motion photogrammetry. Geomorphology, 213, 166-182.

Jensen, J., & Mathews, A. (2016). Assessment of Image-Based Point Cloud Products to Generate a Bare Earth Surface and Estimate Canopy Heights in a Woodland Ecosystem. *Remote Sensing,* 8, doi:10.3390/rs8010050.

Krauss, K. (1997). *Photogrammetry, Volume 2: Advanced Methods and Applications*, 4th ed.; Dümmler: Bonn, Germany.

Lefsky, M.A., Cohen, W.B., Parker, G.G., and D.J. Harding. (2002). Lidar Remote Sensing for Ecosystem Studies. BioScience, 52(1), 19 - 30.

Lehmann, J.R.K., Munchberger, W., Knoth, C., Blodau, C., Nieberding, F., Prinz, T., Pancotto, V.A. and T. Kleinebecker. (2016). High-Resolution Classification fo South Patagonian Peat Bog Microforms Reveals Potential Gaps in Up-Scaled CH4 Fluxes by use of Unmanned Aerial System (UAS) and CIR Imagery. Remote Sensing, 8(173), 1-19.

Lucieer, A., Robinson, S.A., & Bergstrom, B. (2010). Aerial 'OktoKopter' to map Antarctic moss. Australian Antarctic Magazine, 19, 2010.

Lucieer, A., Turner, D., King, D.H., & Robinson, S.A. (2014). Using an Unmanned Aerial Vehicle (UAV) to capture micro-topography of Antarctic moss beds. International Journal of Applied Earth Observation and Geoinformation, 27, 53-62.

Macrae, M. L., Devito, K.J., Strack, M., and J.M. Waddington. (2013). Effect of water table drawdown on peatland nutrient dynamics: implications for climate change. Biogeochemistry, 112, 661-676.

Mancini, F., Dubbini, M., Gattelli, M., Stecchi, F., Fabbri, S., and Gabbianelli, G. (2013). Remote Sensing, 5, 6880-6898.

McGlone, C., Mikhail, E., & Bethel, J. (2004). *Manual of Photogrammetry*, 5th ed.; ASPRS: Bethesda, MD, USA.

Mercer, J., and Westbrook, C. (2016). Ultrahigh-resolution maping of peatland microform using ground-based structure from motion with multiview stereo. Biogeosciences, 121, 2901-2916.

Munir, T.M., Xu, B., Perkins, M., and M. Strack. (2014). Responses of carbon dioxide flux and plant biomass to water table drawdown in a treed peatland in northern Alberta: a climate change perspective. Biogeosciences, 11, 807-820.

Pirotti, F., and P. Tarolli. (2010). Suitability of LiDAR point density and derived landform curvature maps for channel network extraction. Hydrological Processes, 24, 1187-1197.

Pouliot, R., Rochefort, L., and E. Karofeld. (2011). Initiation of microtopography in revegetated cutover peatlands. Applied Vegetation Science, 14, 158-171.

Roosevelt, C. (2014) Mapping site site-level microtopography with Real-Time Kinematic Global Navigation Satellite Systems (RTK GNSS) and Unmanned Aerial Vehicle Photogrammetry (UAVP). Open Archaeology, 2014, 29-53.

Rosnell, T., & Honkavaara, E. (2012). Point Cloud Generation from Aerial Image Data Acquired by a Quadrocopter Type Micro Unmanned Aerial Vehicle and a Digital Still Camera. *Sensors*, 12, 453–480.

Shi, X., Thornton, P.W., Ricciuto, D.M., Hanson, P.J., Sebestyen, S.D., Griffiths, N.A., and G. Bisht. (2015). Representing northern peatland microtopography and hydrology within the Community Land Model. Biogeosciences, 12, 6463-6477.

Strack, M. (Ed.). (2008). Peatlands and Climate Change. Saarijärvi, FIN: International Peat Society (IPS).

Strack, M., Waddington, J.M., Rochefort, L., and E.S. Tuitilla. (2006). Response of vegetation and net ecosystem carbon dioxide exchange at different peatland microforms following water table drawdown. Journal of Geophysical Research, 111, 1-10.

Sturm P., Triggs B. (1996) A factorization based algorithm for multi-image projective structure and motion. In: Buxton B., Cipolla R. (eds) Computer Vision — ECCV '96. ECCV 1996. Lecture Notes in Computer Science, vol 1065. Springer, Berlin, Heidelberg

Turner, D., Lucieer, A., and Watson, C. (2012). An Automated Technique for Generating Georectified Mosaics from Ultra-High Resolution Unmanned Aerial Vehicle (UAV) Imagery, Based on Structure from Motion (SfM) Point Clouds. Remote Sensing, 4(5), 1392-1410.

UAV Geomatics. (2011). Aeryon Scout Technical Specifications. [online content] Retrieved from: http://www.uavgeomatics.com/services/system/scout.pdf

Zainuddin, K., Jaffri, M., Zainal, M., & Ghazali, N. (2016). Verification Test on Ability to Use Low-Cost UAV for Quantifying Tree Height. In Proceedings of the IEEE 12th International Colloquium on Signal Processing & Its Applications, Melaka, Malaysia, 4–6 March 2016.

Chapter Three: UAV Remote Sensing Can Reveal the Effects of Low Impact Seismic Lines on Surface Morphology, Hydrology, and Methane (CH_4) Release in a Boreal Treed Bog

3.1 Abstract

Peatlands are globally significant stores of soil carbon, where local methane (CH_4) emissions are strongly linked to water table (WT) position and microtopography. Historically, these factors have been difficult to measure in the field, constraining our capacity to observe local patterns of variability. In this paper, we show how remote sensing surveys conducted from unmanned aerial vehicle (UAV) platforms can be used to map microtopography and depth to water (DTW) over large areas with good accuracy, paving the way for spatially explicit estimates of CH_4 emissions. This approach enabled us to observe – for the first time – the effects of low-impact seismic lines (LIS; petroleum exploration corridors) on surface morphology and CH_4 emissions in a treed-bog ecosystem in northern Alberta, Canada. Through compaction, LIS lines were found to flatten the observed range in microtopographic elevation by 46cm and decrease mean DTW by 15.4cm, compared to surrounding undisturbed conditions. These alterations are projected to increase CH_4 emissions by 20-120% relative to undisturbed areas, which translates to a total rise of 0.011-0.027 $kgCH_4\ d^{-1}$ per linear kilometer of LIS (~2m wide). The ~16 km of LIS present at our 61 ha study site were predicted to boost CH_4 emissions by 20-70 kg between May and September, 2016.

3.2 Introduction

Peatlands – wetlands that accumulate organic matter – can release large volumes of carbon into the atmosphere in response to anthropogenic disturbances (Wieder & Vitt, 2006; Strack & Waddington, 2006; Parish et al., 2008; Vitt & Bhatti, 2012; Munir et al., 2014). Of particular concern is CH_4: a powerful greenhouse gas (GHG) with a 20-year global warming potential 84-

times greater than that of carbon dioxide (IPCC, 2014a; Zhu et al., 2014). The Intergovernmental Panel on Climate Change states that CH_4 emissions from wetlands are the primary driver of variability in atmospheric CH_4 concentrations (IPCC, 2013). However, the processes relating anthropogenic disturbance to wetland CH_4 production and emission rates are both highly variable and poorly quantified, ultimately limiting our capacity to generate reliable global CH_4 estimates (IPCC, 2014b).

Methane flux is difficult to observe directly, and most non-point estimates rely on modeled associations with environmental covariates (Xu et al., 2010). For example, previous research has shown that CH_4 is released in greater volumes in peatlands when WT is at or near the surface (Wieder & Vitt, 2006), and numerous studies have observed that much of the variability in peatland CH_4 flux can be explained by differences in WT position (Kellner, Waddington & Price, 2005; Couwenberg & Fritz, 2012). WT estimates are commonly derived through repeated field measurements using monitoring wells (Lee and Cherry, 1979; Vazquez-Amábile & Engel, 2005). However, this method is time-consuming and spatially limited to single observation points.

As an alternative or complement to measuring WT, many researchers have mapped microtopography – small-scale heterogeneities in the ground-surface elevation – for the purpose of upscaling point-level GHG measurements (Nungesser, 2003; Strack et al., 2016; Becker et al., 2008; Baird et al., 2009; Loisel & Yu, 2013). In addition to influencing CH_4 flux, microforms (hummocks and hollows) can also foster variations in vegetation community, hydrology, nutrient content, and temperature across peatlands (Lucieer et al., 2010; Macrae et al., 2013; Cresto Aleina et al., 2015; Acharya et al., 2015). Microtopographic observations are generally easier to acquire than WT positions, since no water wells are necessary. In addition, the temporal persistence of

microforms (Nungesser, 2003) means that fewer monitoring events are required for a given site. Regardless, microform data still requires detailed terrain observations, which are normally collected with labor-intensive GPS surveys and specialized equipment (Roosevelt, 2014): a strategy that is expensive and difficult to scale (Pouliot et al., 2011; Roosevelt, 2014).

Recent developments in UAV technology and related workflows have provided exciting new capabilities for peatland observation. UAV platforms can deliver ultra-high resolution imagery and 3-D point clouds (100s of points per m^2) using consumer-grade digital cameras (Lovitt et al., 2017). In turn, these data permit the measurement of CH_4 controlling factors such as WT position (Rahman et al., 2017) and terrain (Lovitt et al., 2017) at unprecedented levels of detail, with capacity for extensive spatial coverage and flexible monitoring intervals. As a result, UAVs present researchers with novel opportunities to investigate the impacts of anthropogenic disturbances on peatland ecosystem functions.

Peatlands in the Canadian province of Alberta and elsewhere have been heavily disturbed by the construction of seismic lines for petroleum resource exploration (Schneider & Dyer, 2006; Pasher, Seed & Duffe, 2013). Seismic lines can be extremely disruptive to low-lying peatland ecosystems, often triggering persistent changes in environmental factors such as hydrology (van Rensen et al., 2015), which may have implications on GHG release rates. Low-impact seismic (LIS) lines are widespread in Alberta, and are deemed 'low impact' on account of reduced clearing widths (~2-3 m) compared to legacy seismic lines (~8-10 m; Schneider & Dyer, 2006; BC OGC, 2016). However LIS are constructed in dense grid networks (~50 m intervals) across vast areas, and there is little evidence of enhanced recovery rates in peatlands, which are notoriously slow to recover from disturbance events (Schnieder & Dyer, 2006; BC OGC, 2015; van Rensen et al.,

2015). Few studies to date have explored the impact of LIS on physical peatland conditions (microtopography, hydrology) and GHG fluxes. Strack et al. (2017) provides the only related study, which investigated GHG emissions from a conventional seismic line-turned winter access road within a wooded fen in northern Alberta. Their results showed that altered ecohydrological conditions on lines can substantially increase GHG emissions, with mean CH_4 flux values measured at 479 CH_4 $m^{-2}d^{-1}$, compared to 4.9 - 6.3 CH_4 $m^{-2}d^{-1}$ in adjacent undisturbed areas (Strack et al., 2017).

The focus of this research was twofold: first, to compare two UAV-based methods of estimating CH_4 release from a treed-bog study site in northern Alberta, Canada: (i) microtopography and (ii) DTW; and second, to quantify the impact of LIS lines on CH_4 release, microtopography, and DTW across our 61 hectare study site. Our work represents the first-known spatially explicit quantification of LIS impacts on morphology, hydrology, and chemistry on peatlands in Canada.

3.3 Materials and Methods

3.3.1 Study site.

The study site is a ~61 ha portion of treed bog located roughly 35 km northeast of Peace River, Alberta (Figure 3.1a). Treed bogs are a type of wetland that receive water exclusively from precipitation (no input from surrounding watersheds), and accumulate organic matter (peat) on account of their low-oxygen environment (National Wetlands Working Group, 1997). Within our study site, a 3.8 ha subset area (Figure 3.1b) was used to assess model accuracies and generate CH_4 estimates for up-scaling across the full site. The study area is heavily disturbed by resource exploration and extraction activities. A mineral-filled access road traverses the eastern portion of

the site, and the center is bisected by a pipeline. However, the main focus of the present work is the dense network of ~2-m wide LIS lines, which total 16 km in length within the study area and 1.4 km in length within the subset area. In the undisturbed portions of the bog, microforms (hummocks and hollows) are present at scales from 30-cm to 1-m diameter and height, and occur in roughly equal proportions. Vegetation is typical of treed bogs within the region, with black spruce (Picea mariana) being the dominant tree species, labrador tea (*Rhododendron groelandicum*) and small cranberry (*Oxycoccus microcarpus*) representing the majority of shrub species, and Sphagnum spp. (*Sphagnum fuscum* - rusty peat moss, *Sphagnum capillifolium* - acute-leaved peat moss, *Sphagnum girgensohnii* - Girgensohn's peat moss, *Sphagnum magellanicum* - midway peat moss, *Sphagnum warnstorfii* - Warnstorf's peat moss) dominating the ground layer. Zones disturbed by LIS appear as linear clearings with apparent flattening of microtopography. In many cases, the remnants of vehicle tracks were observed along these features, having formed pools of standing water surrounded by vascular vegetation more commonly found in fen ecosystems, including willow (Salix spp.) and a variety of sedges. Repeated vehicle use on seismic lines in this study area was not observed, suggesting the tracks were created during initial construction.

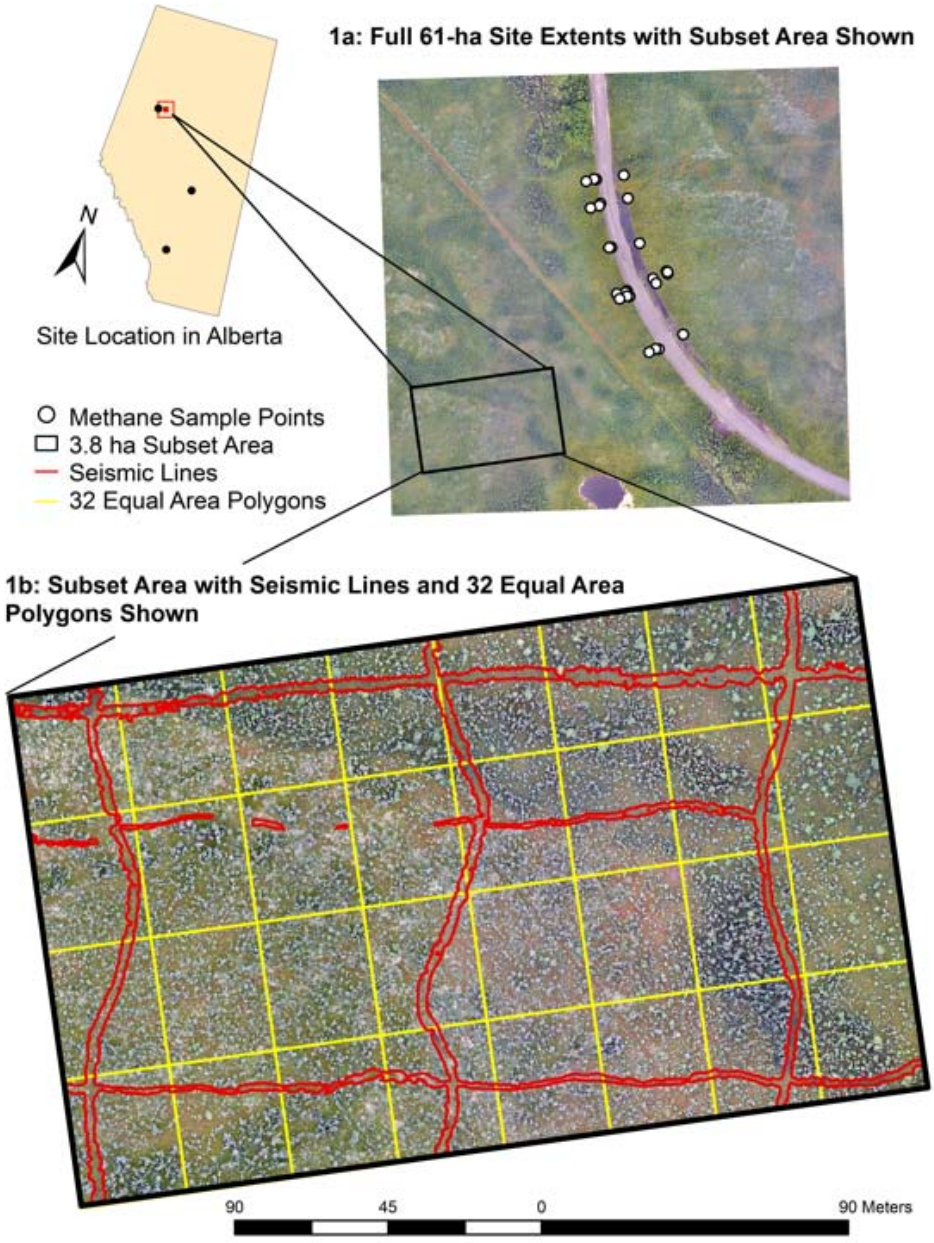

Figure 3.1: *Full Study Site Extents (3.1a) and Subset (3.1b) Showing Equal Area Polygons and Seismic Lines used to Generate Methane Flux Estimates from MT and DTW Surfaces (Process Explained in Section 2.2.3.3). Within Figure 3.1b, a variety of surface features can be observed including dispersed pockets of dense black spruce.*

3.3.2 Field-Measured CH_4 Flux (Point Samples).

Methane samples were collected at 27 points (collars) every second week over a 150-day monitoring period, which ran from May to September of 2016. Collars were permanently installed across 14 hollows and 11 hummocks in order to capture a range of data for each identified microform type. These collars were measured as part of another study investigating the impact of a permanent access road on peatland carbon exchange, but any collars in areas specifically impacted by road construction (i.e., where vegetation had been disturbed) were not included in the present dataset. Since the road has impacted hydrology at the site, some of the measurement collars were likely wetter or drier than would have occurred in undisturbed conditions, which allowed for a wider range of DTW to be considered. Therefore, although no collars were specifically located on seismic lines, they do represent the full range of microtopography and WT position present across the site. Prior to collecting the gas samples, a closed opaque chamber (60 cm x 60 cm x 30 cm) was fitted over each collar and sealed from the atmosphere (Tuittila et al., 2000). An internal fan mixed headspace air, and a 20-mL syringe was used to collect gas samples at pre-determined intervals (7, 15, 25, and 35 minutes). A thermocouple was used to determine the chamber's internal air temperature at the time each sample was collected. Gas samples were then stored in pre-evacuated Exetainers (Labco Ltd., UK) and shipped to the University of Waterloo for analysis. On each sampling day, four ambient gas samples were also collected to provide background CH_4 concentrations at the study site, and the WT position of wells installed beside each collar was recorded.

The CH_4 concentration of each sample was analyzed using a Shimadzu GC-2014 gas chromatograph (GC), at the University of Waterloo, and CH_4 flux was determined from the linear

change in concentration over time. Flux measurement with a poor linear relationship ($R^2 < 0.75$) were deemed indicative of chamber disturbance during measurement, and were removed from the dataset. These instances generally occur due to ebullition, and indicate that CH_4 flux is likely poorly represented by our chamber measurements (as in other studies such as Christen et al., 2016). Therefore, flux estimates and the calculated impact of seismic lines on ecosystem CH_4 flux are likely conservative. Fluxes in which no change in CH_4 concentration was noted (i.e., change in concentration was within the precision of the GC of 0.5 ppm) were assigned a value of zero. Approximately 10% of the data was removed following these protocols. Accepted CH_4 fluxes were then corrected for both internal chamber air temperature and chamber volume.

Flux sampling points were identified as either hummocks or hollows based on vegetation and microtopographic characteristics. From this segregation, the average CH_4 flux per microform (hummock vs. hollow) was calculated. We then determined the relationship between CH_4 emission and DTW by applying a LOG_{10} transformation to the 150-day mean CH_4 flux data of each plot, and performing a linear regression with mean WT position of each corresponding water well. Previous studies have noted that a log-linear relationship exists between CH_4 flux and WT position (Moore and Roulet, 1993, Bubier et al. 1993). The LOG_{10} approach was found to improve both the normality of the CH_4 flux data distribution, and residual errors of the regression. Across all sampling plots, the relationship between CH_4 flux and WT position ($p < 0.01$; $R^2 = 0.28$; Figure 3.2) was described by the following equation:

$$\boldsymbol{log_{10}(CH_4) = 0.0305*WTposition + 1.5257} \quad \textbf{[1]}$$

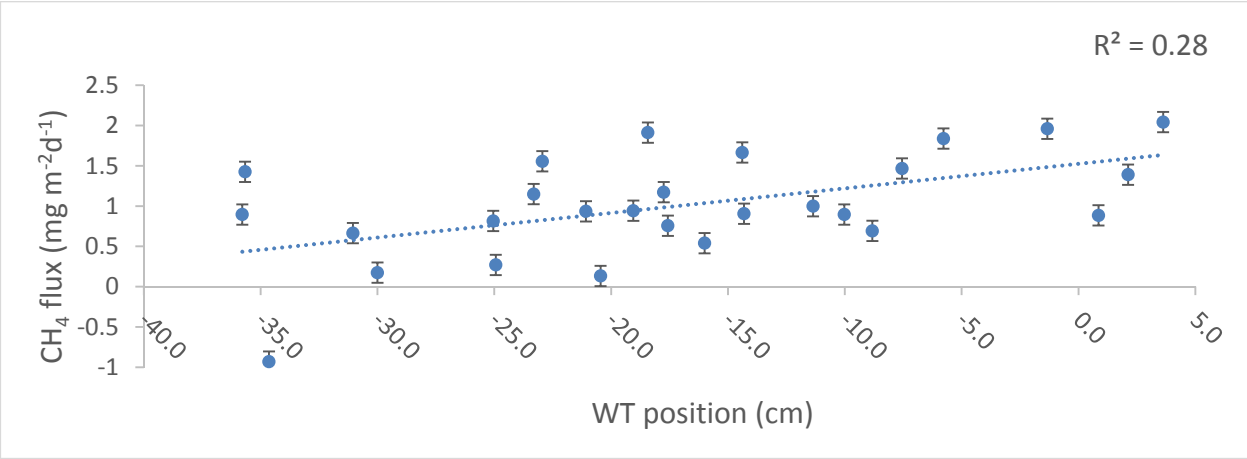

***Figure 3.2**: Relationship between LOGCH₄ (mgm^{-2}d^{-1}) and Water Table position (cm), where water table located below ground surface is given a negative value. Error bars indicate the standard error of LOG$_{CH4}$ values (±0.13).*

3.3.3 Remote Sensing Observations.

UAV data were acquired on September 2, 2016 using an Aeryon Skyranger fitted with an HDZoom30 RGB optical camera (20 megapixels, global shutter). The flight was completed between 9:30 am and 2:00 pm at 110 m altitude with approximate wind speeds of 3m/s. Data were collected continuously during flights (flight speed 4 m/s) to minimize battery replacements (3 for full site coverage), with flight lines positioned to deliver 80% endlap and 60% sidelap amongst photographs. Ground resolution of the resulting dataset was approximately 2 cm. Lighting was diffuse and low during flight operations due to persistent high cloud cover, thereby minimizing the amount of shadow in the imagery. It's worth noting that small pools of standing water were dispersed across the site resulting from very wet conditions leading up to flight operations. These pools may have influenced UAV product accuracies due to increased surface homogeneity and reflectivity, though accuracies of the resultant dense point cloud and digital surface models (DSM) were deemed sufficient to proceed with secondary analyses.

3.3.4. Classification of Terrain (Microtopography).

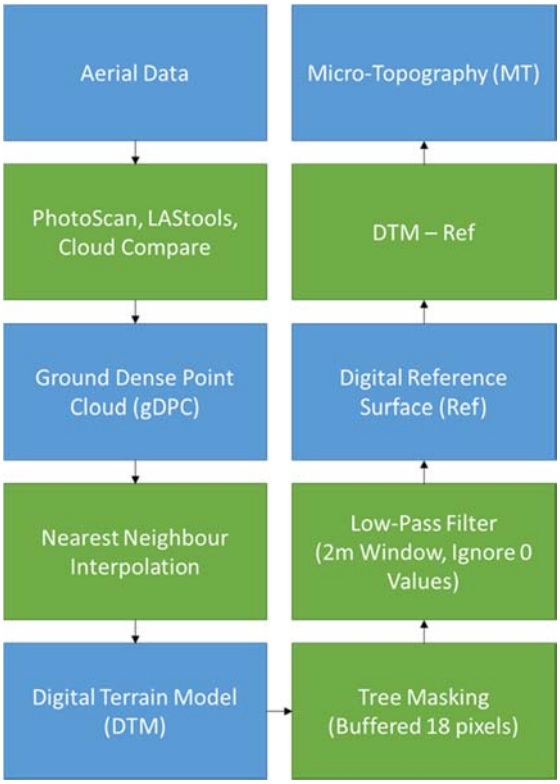

***Figure 3.3**: The workflow for generating microtopographic surface.*

The workflow used to generate a classified microtopography surface is summarized in Figure 3.3. From the aerial data, a dense point cloud comprised only of ground points, which we call the ground dense point cloud (gDPC), was generated as per Lovitt et al. (2017). Accuracies of the gDPC were estimated by PhotoScan (Version: 1.2.4) as ~0 cm (x,y) and 21 cm (z). Nearest-neighbour interpolation was applied to the gDPC in ESRI ArcMap (Version: 10.3.1) to generate the DTM. Using ENVI (Version 5.1) we then applied a mask, buffered by 18 pixels, over treed areas, followed by a low-pass filter (window size 2 m) to generate a reference surface (Ref) representing general site slope. The purpose of buffering the tree mask was to ensure that

vegetation edge points (ie. points falling on the boundary between terrain and tree, as per Lovitt et al. 2017) were excluded from the low-pass filter calculation. The purpose of excluding these points was to avoid artificially increasing ground-surface elevations in areas where points represented vegetation rather than ground. A window size of 2 m was selected for the low-pass filter after comparison with window sizes of 1 m, 1.5 m, and 3 m. In order to ensure ENVI was excluding masked areas (assigned 0 value) in the averaging window calculation, we applied a custom IDL script which forced ENVI to average pixels with non-zero values only. Finally, after generating Ref, we subtracted it from the DTM [DTM-Ref] to generate a microtopography elevation surface (MT; Figure 3.4).

We classified the MT surface using a simple, pixel-based density slicing approach in ENVI. A total of three classes were identified across the site: (i) hummocks, (ii) hollows, and (iii) trees. The classification specified hummocks > 0, hollows < 0, and trees = 0 (masked). The approach was based on the assumption that areas taller than the average elevation of the surrounding peatland (positive MT surface values) corresponded to hummocks, while areas below the average elevation (negative MT surface values) corresponded to hollows (Figure 3.4).

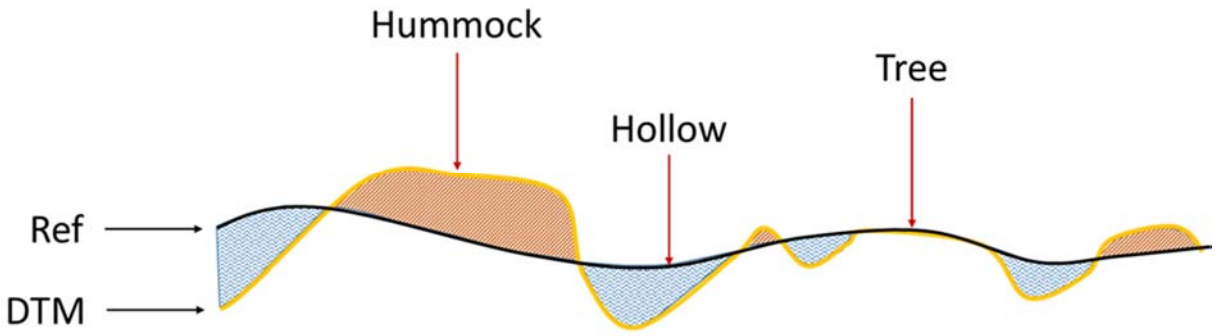

Figure 3.4: *Process of producing the microtopography surface by subtracting the reference surface (Ref) from the digital terrain model (DTM). Areas above Ref are considered hummocks (brown), areas below are considered hollows (light blue), and areas which are masked are assigned the class 'Trees'.*

Classification accuracy was assessed by generating a confusion matrix using 105 validation points collected in the field. Samples were selected using a stratified-random sampling strategy, and observed locations were surveyed using a Trimble R4 real-time kinematic (RTK) global navigation satellite system (GNSS) system. In addition to this ground data, 50 random points representing tree pixels were selected for assessment of the tree class. Results of this classification are summarized in Table 3.1. The overall accuracy of the classification was 84% (kappa: 0.76). This classification performed good overall, though it resulted in a slight over-representation of hollows (86% producer's accuracy vs. 77% user's accuracy), and a slight under-representation of trees (92% producer's accuracy vs. 100% user's accuracy) across the site. However, there appears to be no bias in the classification of hummocks (75% producer's accuracy vs. 77% user's accuracy). The majority of errors in distinguishing hummocks and hollows were found to occur in cases where the target microform was within ±5 cm of the reference surface, an area we define as the microform 'transition zone'. The accuracy of the classification was comparable to results

reported in similar studies (Lehman et al., 2016), and was therefore deemed acceptable for use in estimating CH_4 emissions and disturbance related changes in microtopography.

Table 3.1. Confusion Matrix of Pixel-Based Density Slicing Classification Approach (Overall Accuracy = 84%; kappa = 0.76)

		Reference				
	n = 155	Hummock	Hollow	Trees	Total	User's Accuracy (%)
Predicted	Hummock	40	8	4	52	77
	Hollow	13	44	0	57	77
	Trees	0	0	46	46	100
	Total	53	52	50	155	
	Producer's Accuracy (%)	75	86	92		

3.3.5. Generating the Depth to Water Surface (DTW) Surface.

The DTW surface was generated using the methods described by Rahman et al. (2017). In their workflow, areas of stable open water were first classified using a decision-tree classification scheme. From among the resulting classified pixels, spatially distributed samples of open water were selected, and their elevations interpolated via ordinary kriging to obtain the height of the WT in meters above mean sea level (masl). The groundwater-level surface was then subtracted from the DTM to obtain DTW. The accuracy of the DTW surface was assessed as per Rahman et al. (2017). Validation of the DTW surface was completed by comparing modeled values against field

data collected at five wells within the study site. The results of this comparison indicated an RMSE of the DTW surface in the study area subset of 11.3 cm.

Since WT fluctuates throughout the year, we needed to adjust the DTW surface estimated at the date of the UAV flight on September 2 in order to reflect the mean value of DTW across our flux monitoring period from May to September. True point measures of DTW were observed at 37 water wells across the study area by field personnel every two weeks. We selected the well which was located closest to our 3.8 ha subset area, and averaged all measurements to determine the mean DTW in the well over the 150-day monitoring period. We then compared this value with that estimated from our UAV model at the well's location (collected as part of the terrestrial survey via RTK GNSS). This comparison revealed that the mean DTW, as calculated from the water well data, was 4.8 cm lower than the DTW position estimated by the UAV model for September 2. As a result, we lowered the DTW model by 4.8 cm to better reflect the seasonal average. This adjustment assumes that WT fluctuates consistently across the site, and that averaging the collected data from one sampling point is sufficient to estimate mean WT position across the larger area.

3.3.6. Predicted CH_4 Flux.

The subset area was divided into 32 equal-area quadrats (~1189 m^2 each) to allow for a statistical analysis of flux estimates within each quadrat (Figure 3.1b). Seismic lines were manually digitized from the high-resolution UAV orthophoto in ESRI ArcMap 10.3.1. We clipped the MT and DTW layers using seismic-line boundaries to divide the study site into two categories: undisturbed and disturbed. CH_4 emissions were then estimated from each category (undisturbed: MT & DTW, disturbed: MT & DTW) for each of the 32 polygons.

Figure 3.5 provides a visual representation of surfaces used in predicting CH_4 emission. To estimate CH_4 fluxes from the MT surfaces, the percent-area coverage of hummock, hollow, and tree (undisturbed) was calculated and multiplied by the corresponding average fluxes of 13.3, 34.5, and 24.3 $mgCH_4\ m^{-2}\ d^{-1}$. The standard errors of these fluxes were estimated as 3.8, 9.5, and 0.09 $mgCH_4\ m^{-2}\ d^{-1}$, respectively. As CH_4 fluxes were not directly measured in areas below trees, we assigned average CH_4 values to treed areas. Based on field observations of microtopographic conditions below trees, no discernable pattern in microform occurrence in these areas was identified, so applying an average flux value was considered appropriate. This approach involved calculating the average flux for undisturbed and disturbed portions of the polygon, estimated exclusively by the areal coverage of classified hummocks and hollows in these areas. Since this method estimated greater CH_4 emission within disturbed areas (higher occurrence of hollows), a slightly higher average flux value of 26.1 $mgCH_4\ m^{-2}\ d^{-1}$ was used for trees in these areas. The standard error of this flux was estimated as 0.3 $mgCH_4\ m^{-2}\ d^{-1}$.

To estimate CH_4 flux from the DTW surface, equation [1] was applied to the DTW surface. This produced a CH_4 surface with flux values across the site at 2 cm resolution. The same buffered tree mask was then applied to the DTW surface to ensure flux estimates between the DTW and MT surface were comparable. Similar to the MT surface, treed areas were assigned an average flux value based upon their surrounding conditions; i.e., Trees [undisturbed]: 12.2 $mgCH_4\ m^{-2}\ d^{-1}$, Trees [disturbed]: 27.5 $mgCH_4\ m^{-2}\ d^{-1}$ with a corresponding standard error of 1.0 and 3.6 $mgCH_4\ m^{-2}\ d^{-1}$.

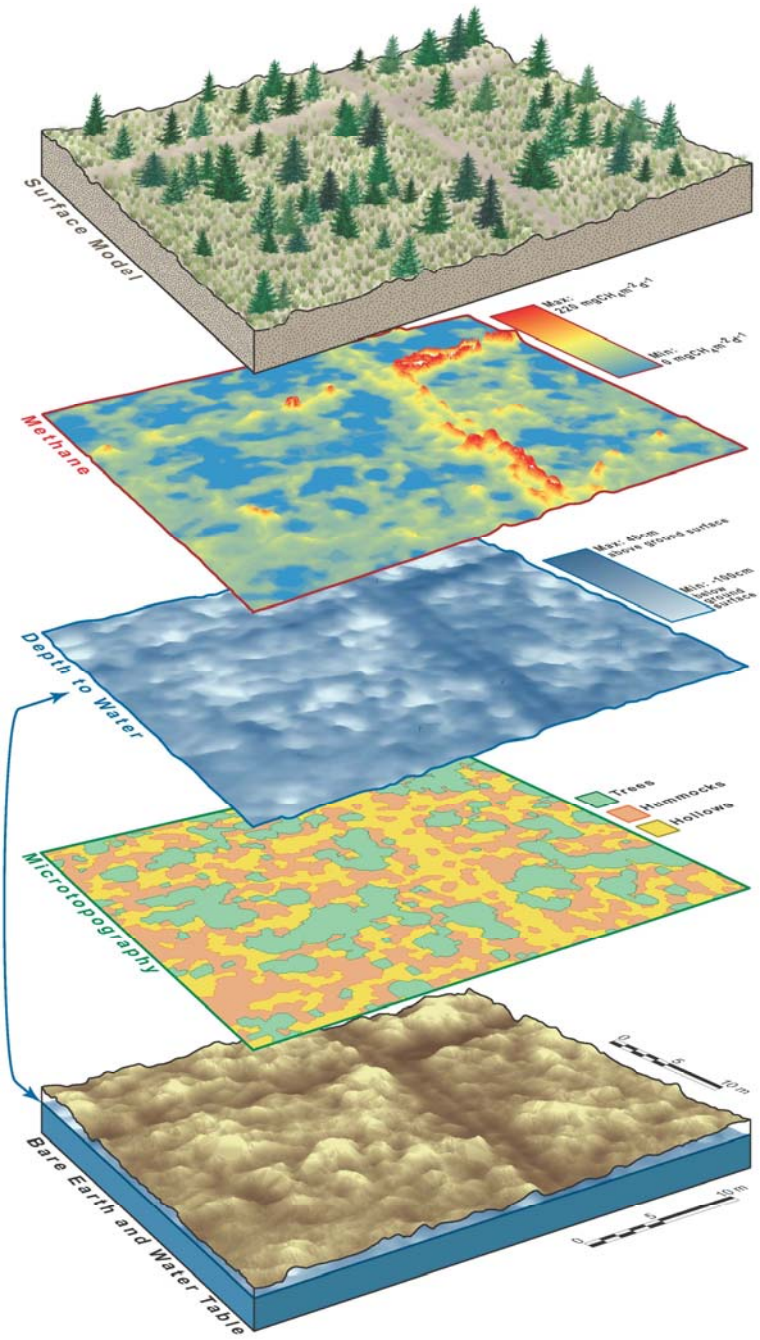

Figure 3.5: *Graphical visualization of digital surfaces generated from the input surface model (shown at top of stack). Surfaces include the bare earth and water table (WT), microtopography, depth to water (DTW) and CH_4. DTW is shown in centimeters where depths below ground surface are negative, CH_4 is shown in $mgCH_4\ m^{-2}\ d^{-1}$. The DTW surface was derived from the bare earth and WT surfaces, the arrow shows this link to the WT position below ground surface. Figure prepared by Robin Poitras and Julie Lovitt at the University of Calgary.*

3.4 Results

3.4.1 Seismic Line Impacts on Microtopography and DTW.

Mean ground elevations were significantly different between undisturbed and disturbed areas ($p<0.01$), with seismic lines occurring 2.2 cm lower on average relative to undisturbed peat (RMSE: 2.6 cm). Additionally, an overall flattening of microtopographic features was noted along LIS (Figure 3.5, microtopography), with the majority of microforms existing within ±5 cm of Ref. By comparison, greater variation in ground-surface elevations was noted in undisturbed areas, specifically an increased occurrence of tall hummocks (i.e. ground > 10 cm of Ref). Ground elevations in undisturbed areas (32 total polygons) ranged from -74 cm below to +97 cm above Ref, with a mean value of 0.6 cm. Comparatively, elevations in disturbed areas (27 total polygons) ranged from -64 cm to +64 cm, with a mean value of -1.5 cm (Table 3.2). This translates to a 46-cm reduction in the average microform elevation range within seismic lines.

A near-equal frequency of hummock vs. hollow occurrence was noted in undisturbed areas (51.8% hollow coverage). However, an increase in hollow prevalence (60.8% coverage) was observed along seismic lines (Table 3.2).

Table 3.2. Summary Table Showing Absolute and Average Differences in Microform Heights, Percent Coverage and Measured Depth-to-Water between Undisturbed and Disturbed Areas

			Undisturbed (32 Polygons)	Disturbed (27 Polygons)
Microform Height (cm)	Absolute	Minimum	-74	-64
		Maximum	97	64
		Range	171	128
	Average	Minimum	-48	-30
		Maximum	69	41
		Range	117	71
		Mean	0.6	-1.5
		Hummock/Hollow Coverage (%)	48.2/51.8	39.2/60.8
Depth-to-Water (cm)	Absolute	Minimum	-159	-81
		Maximum	71	39
		Range	230	120
	Average	Minimum	-95	-40
		Maximum	24	21
		Range	119	61
		Mean	-17.5	-2.1

Significant differences in DTW were found to exist between seismic lines and undisturbed peatland areas ($p < 0.01$). In undisturbed areas, DTW ranged from 159 cm below to 71 cm above ground surface, with a mean value of 17.5 cm below surface (Table 3.2). Along seismic lines, DTW ranged from 81 cm below to 39 cm above ground surface, with a mean value of 2.1 cm below the surface. Comparing average values suggests that little difference exists in maximum

DTW values between undisturbed areas (24 cm) and disturbed areas (21 cm). However, there were clear differences in the calculated average minimum DTW values (-95 cm vs. -40 cm respectively). This indicates that a shallower WT position exists along seismic lines (average difference 15.4 cm; RMSE: 17.5 cm).

3.4.2 CH_4 Flux Estimates and Quantification of Seismic Line Impacts.

Table 3.3 summarizes partial (undisturbed vs disturbed) and total (undisturbed + disturbed) CH_4 flux estimates for the study site as calculated by both surfaces (MT and DTW), as well as estimated increase (%) of CH_4 along seismic lines. Significant differences were noted between the two surfaces when predicting CH_4 flux in undisturbed areas ($p<0.01$) but not along seismic lines ($p=0.454$). Total CH_4 for the 3.8 ha study site over the 150-day flux monitoring period was estimated as 124 kg (MT), and 76 kg (DTW), resulting in the MT surface estimating +48 kgCH_4 more than the DTW. The correlation between the two surfaces' estimates in undisturbed areas was slightly lower (0.55) than that observed in disturbed areas (0.69). Methane emissions are predicted to increase substantially (MT: +20%, DTW: +120%) on seismic lines relative to undisturbed peatland. Results of the statistical analysis indicate that these differences are significant ($p<0.01$) in both surfaces (MT & DTW).

Table 3.3. Predicted CH_4 Emissions (standard error) of 3.8ha Subset Study Site over 150-day monitoring Period and Estimated Increase (per ha) due to Seismic Line Disturbance

		MT Surface	DTW Surface
Undisturbed	Total Estimated CH_4 Flux ($kg \cdot d^{-1}$)	0.759 (0.0003)	0.433 (0.0006)
	Total Area (ha)	3.78	3.78
	Avg Predicted Flux ($kg \cdot ha^{-1} \cdot d^{-1}$)	0.216 (0.1)	0.123 (0.3)
Disturbed	Total Estimated CH_4 Flux ($kg \cdot d^{-1}$)	0.070 (0.0003)	0.072 (0.0004)
	Total Area (ha)	0.269	0.267
	Avg Predicted Flux ($kg \cdot ha^{-1} \cdot d^{-1}$)	0.261 (0.3)	0.270 (3.0)
Total Site	CH_4 Increase per ha due to Disturbance	20%	120%
	Percent of Site Disturbed	7%	7%
	Total Predicted Flux for Site ($kg \cdot 3.8\ ha^{-1} \cdot 150\ d^{-1}$)	124	76

To estimate CH_4 flux per linear kilometer of LIS, we multiplied predicted CH_4 flux (in kg per m^2 d^{-1}) by the estimated line width (2 m) and length (1000 m). Both surfaces estimate approximately 0.050 $kgCH_4$ d^{-1} per linear kilometer of LIS (MT: 0.052 $kgCH_4$ d^{-1}, DTW: 0.054 $kgCH_4$ d^{-1}). This translates to an increase between 0.011 and 0.027 $kgCH_4$ d^{-1} per linear kilometer of LIS. These values can be adjusted to represent older, legacy lines of varying widths as desired.

Table 3.4 presents estimates of CH_4 flux across the entire 61 ha study site. Excluding other disturbance features (pipeline and road) LIS account for approximately 5.2% of the total site coverage. Assuming the site had 0% seismic line disturbance, total site CH_4 emission estimated over the 150 day monitoring period is predicted to be between 1,130 $kgCH_4$ (DTW) and 1,990 $kgCH_4$ (MT). The standard error for these values is estimated to be 30 and 13 $kgCH_4$ respectively. Adjusting these predictions to include 5.2% LIS disturbance, total CH_4 emission estimates increase

to 1,200 $kgCH_4$ (DTW) and 2,010 $kgCH_4$ (MT), with standard errors of 15 and 2 $kgCH_4$, respectively. This translates to an absolute total site CH_4 emission increase at the 61 ha site over the 150 day monitoring period of approximately 70 kg and 20 kg, respectively.

Table 3.4. Estimated Total CH_4 Emission across 61 ha Study Site (as per Figure 3.1a) and Predicted Increase over 150 day monitoring Period due to Seismic Line Disturbance

	Undisturbed	Disturbed
Areal Coverage	94.8%	5.2%
MT Flux ($kgha^{-1}d^{-1}$)	0.216	0.261
DTW Flux ($kgha^{-1}d^{-1}$)	0.123	0.270

	MT Surface	DTW Surface
Total Predicted Flux in Undisturbed Areas ($kg{\cdot}ha^{-1}{\cdot}d^{-1}$)	1.25	0.71
Total Predicted Flux in Disturbed Areas ($kg{\cdot}ha^{-1}{\cdot}d^{-1}$)	0.08	0.09
Theoretical Total Predicted Flux of Site (%coverage of LIS = 0) ($kg{\cdot}ha^{-1}{\cdot}d^{-1}$)	1.32	0.75
Actual Total Predicted Flux of Site (%coverage of LIS = 5.2) ($kg{\cdot}ha^{-1}{\cdot}d^{-1}$)	1.33	0.80
Absolute Total Site CH_4 Increase due to Disturbance ($kg \cdot 61ha^{-1} \cdot 150d^{-1}$)	20	70

Using the 0% disturbance-site flux values, we performed a sensitivity analysis of calculated CH_4 emissions across the study site over the 150 day monitoring period, based on the errors documented for both surfaces (11.3 cm RMSE for DTW; 84% for MT). The DTW surface was regenerated twice: once lower (DTW minus 11.3 cm) and once higher (DTW plus 11.3 cm) based on reported RMSEs. These adjustments produced estimated CH_4 fluxes ranging from 960 $kgCH_4 \cdot 61ha^{-1} \cdot 150d^{-1}$ (DTW minus 11.3 cm) to 2,200 $kgCH_4 \cdot 61ha^{-1} \cdot 150d^{-1}$ (DTW plus 11.3 cm), revealing the estimated uncertainty in our DTW generated CH_4 predictions. We did a similar analysis for the fluxes estimated from the MT surface, both increasing (plus 16%) and decreasing

(minus 16%) the proportion of hummocks to hollows, based on reported accuracies. These adjustments produced estimated CH_4 fluxes ranging from 1,480 $kgCH_4 \cdot 61ha^{-1} \cdot 150d^{-1}$ (proportion of hummocks plus 16%) to 2,200 $kgCH_4 \cdot 61ha^{-1} \cdot 150d^{-1}$ (proportion of hollows plus 16%). Again we interpret this as an estimate of uncertainty in our MT generated CH_4 predictions. The sensitivity analyses reveals greater uncertainty in CH_4 estimates arising from the DTW surface (960-2,200 $kgCH_4 \cdot 61ha^{-1} \cdot 150d^{-1}$) than the MT surface (1480-2,200 $kgCH_4 \cdot 61ha^{-1} \cdot 150d^{-1}$).

3.5 Discussion

We conducted a thorough comparison of peatland microtopographic and DTW characteristics across our study area to determine how seismic lines have impacted these key environmental factors. Results of this assessment indicate that LIS lines at the study site caused an overall flattening of microforms, increase in hollow frequency, and decreased the mean ground elevations by 2 cm (RMSE: 2.6 cm). These same disturbances decreased mean DTW by 15.5 cm. By comparison, a study investigating permafrost-related impacts in Canada's Northwest Territories showed that seismic lines on permafrost peatlands produced ground subsistence between 3 and 53 cm (Williams, Quinton & Baltzer, 2013). While these dramatic results are caused at least in part due to altered permafrost regimes along seismic lines, they reflect the trends observed in our analysis: LIS lines stand out from the surrounding peatland as lower, wetter, and flatter areas. Assuming that our study site is indicative of typical treed bog conditions, these findings can partially explain the lack of successful ecosystem recovery (i.e. restoration of ground surface, hydrological and vegetation conditions comparable to pre disturbance) along linear features within the western Canadian Boreal region. Van Rensen et al. (2015) indicated wetter (flooded) areas are less likely to establish new Sphagnum moss communities, an important genus in natural hummock

formation. This suggests LIS lines within our study site, and those in comparable disturbed peatlands, are highly unlikely to recover without the pursuit of active restoration designed to recreate suitable surface conditions.

Furthermore, the results of our CH_4 flux estimates indicate the strength of the link between lower, wetter peatland conditions, as found along LIS, and significantly increased CH_4 emissions. Both MT and DTW surfaces predict CH_4 release increases between 20% (MT) and 120% (DTW) along LIS (2 m width) compared to adjacent undisturbed areas. Logically, it follows that wider conventional lines, such as those constructed in the mid 1950's, would produce even higher CH_4 emission per linear kilometer. Considering these wider lines have been linked to other altered environmental conditions, including light exposure and surface temperatures (Dabros et al., 2017), these increases in CH_4 emission may be exponential, and the cumulative emission of unreclaimed LISs over their lifespan is likely to be highly significant.

In this study, microtopography and DTW were modelled from UAV data with good results (MT: 84% overall accuracy, DTW: 11.3 cm RMSE), though uncertainties within these layers persist. Our sensitivity analyses reveal these uncertainties to produce greater variability in CH_4 output from the DTW surface. This is perhaps predictable, given the simpler nature by which CH_4 estimates are up-scaled with the MT surface, using a small number of averaged microform fluxes. However, it also reflects the fact that the log-linear equation [1] of the DTW approach is highly sensitive to the quality of input water-level data; small errors in estimated WT position may produce large uncertainty in CH_4 predictions. Unfortunately, we had insufficient flux data to perform an accuracy assessment of CH_4 estimates: something that should be pursued in future research.

Lacking a proper model validation, we assume the more technically complex DTW surface is better representative of real world conditions in undisturbed areas due to the higher spatial resolution of CH_4 estimates. This is in line with previous studies that indicate simple classifications are likely to over- or under-estimate CH_4 emission (Hartley et al., 2015; Lehmann et al., 2016). However, there was no significant difference in estimates from either surface along seismic lines. The higher estimation of the MT surface within undisturbed areas is likely due to the wide range of flux rates reported across microforms of differing heights (hummocks) and depths (hollows). We suggest including additional classes of microforms may address this issue by accounting for greater variability in both microforms and CH_4 emission rates within undisturbed peatland areas (Bubier et al., 1993). Furthermore, this may overcome classification issues in differentiating hummocks from hollows as the majority of these errors were found to occur in in the transition zone, the area between clearly identifiable microforms (±5 cm of Ref). Alternatively, a Lawn class could be created to capture areas within the transition zone, entirely replacing the need for 'Transitional Hummock' and 'Transitional Hollow' classes. Bubier et al. (1993) define lawns as areas which are relatively flat compared to the surrounding peatland surface. In this case, areas within the identified transition zone would fit the description of lawns as they are within 5 cm of the mean peatland surface elevation.

3.5.1 Potential Sources of Error

As described in Lovitt et al. (2017) and Rahman et al. (2017) numerous external factors, such as weather conditions during UAV operations and input model accuracies (ie. DTM, water level surface), may have affected the accuracy of our results. These factors were addressed in their respective manuscripts and will not be discussed further.

The microtopographic classification method applied in this study could be improved. Due to the slight over representation of hollows, the MT surface likely overestimates CH_4 flux in undisturbed areas, and comparatively underestimates the impact of seismic lines. Similarly, the inclusion of vegetation border points during DTM generation caused us to apply an 18 pixel buffer to the tree mask which likely removed useful terrain pixels from the MT surface.

Predicting CH_4 emission from the MT surface was limited by a lack of CH4 measurements across a variety of microform heights. As a result, average flux values were applied to only three microform classes (hummocks, hollows, and trees), which likely overestimated flux from undisturbed areas. Although CH_4 estimates from the DTW surface were anticipated to be more accurate than the MT surface, the reported R^2 value (0.28) of the LOG(CH_4) linear equation [1] may explain a degree of uncertainty in the results. While this R^2 value is comparable to similar studies (Moore & Roulet, 1993: $R^2 = 0.332$), others have reported stronger relationships between peatland CH_4 flux and WT position (Bubier et al., 1993: $R^2 = 0.649$; Shannon & White, 1994: $R^2 = 0.58$, Sundh et al., 1994: $R^2 = 0.50$, Bubier, 1995: $R^2 = 0.74$), Therefore, expanding the CH_4 dataset (spatially or temporally) may strengthen the relationship between CH_4 flux and WT position, and improve CH_4 estimates from the DTW surface. Conversely, this R^2 value may indicate that other environmental factors have greater influence on CH_4 generation and emission at this study site. For example, previous studies indicate that soil temperature may influence bog CH_4 flux (van Winden et al., 2012), and vegetation type is often a strong predictor of peatland CH_4 flux (Bubier, 1995; Couwenberg et al., 2011).

It was beyond the scope of this paper to investigate other disturbance features present at the study site (pipeline and road). However, these features likely have similar impacts on peatland

hydrology and microtopography, and we recommend future research on how they may alter peatland CH_4 release. Moreover, peat composition and biogenic gas distribution is anticipated to be comparable across the entire 61 ha study site, which may not be the case if woody debris or confining layers, such as peat with low permeability, vary (Comas et al., 2014). Therefore, these methods of estimating CH_4 emissions across large areas may need to be modified by site-specific criteria prior to application.

3.6 Conclusions

The primary objective of this research was to use UAV data to quantify the impact of seismic lines on peatland CH_4 emissions, microtopography, and DTW within a boreal treed bog in northern Alberta, Canada. From this investigation, we determined that seismic lines have significant impacts on the peatland ecosystem, causing overall flattening of microtopography and decreasing DTW, resulting in significant increases in CH_4 release. Based on this assessment, and the knowledge that seismic lines are widespread within the western Canadian Boreal region, we suggest these linear disturbances should be included in land-use change GHG emission estimation to avoid under-reporting at the national scale. Furthermore, due to the noted degree of microtopographic and DTW disturbance, we posit that active restoration will likely be necessary to achieve recovery of vegetation and ecosystem function along LIS. Additional data are required to properly validate the CH_4 flux estimates and determine which UAV method is superior; however, we believe the relationships presented here (significant increase in CH_4 emission along seismic lines) are valid based upon the assessment of altered physical parameters (microtopography and DTW).

This research represents an initial attempt to determine how LIS have altered boreal peatland carbon balance and storage functions at a single treed bog in northern Alberta. However, peatlands are incredibly diverse ecosystems and we encourage additional studies building upon our methods, and/or aimed at investigating similar disturbance features within different peatland types. Moreover, assessing the impact of mineral-filled linear disturbances, such as pipeline right of ways and resource roads, would be beneficial. Additionally, it would be useful to up-scale these findings to the regional level, and/or adjust national GHG estimates to include disturbance features, especially considering key points in the current provincial government's Climate Leadership Plan have been identified as reducing CH_4 emissions by 45% by 2025, and improving management of industry GHG emissions (GoA, 2017).

3.7 References

Akumu,C.E., Pathirana, S., Baban, S., & bucher, D. (2010). Monitoring coastal wetland communities in north-eastern NSW using ASTER and Landsat satellite data. Wetlands Ecological Management, 18, 357-365.

Acharya, S., Kaplan, D. A., Casey, S., Cohen, M. J., & Jawitz, J. W. (2015). Coupled local facilitation and global hydrologic inhibition drive landscape geometry in a patterned peatland. Hydrology and Earth System Sciences, 19(5), 2133–2144.

Baird, A.J., Belyea, L.R., & Morris, P.J. (2009). Upscaling of peatland-atmosphere fluxes of methane: small-scale heterogeneity in process rates and the pitfalls of "bucket-and-slab" models. In A.J. Baird, L.R. Belyea, X. Comas, A.S. Reeve, L.D. Slater (Eds.), Carbon Cycling in Northern Peatlands, Geophysical Monograph (37-53). Washington D.C.: American Geophysical Union.

British Columbia Oil and Gas Commission (BC OGC). (2016). Natural Recovery on Low Impact Seismic Lines in Northeast British Columbia (BCIP-2016-18). Prepared by: Golder Associates. Report No. 1654243. Retrieved from: http://www.bcogris.ca/sites/default/files/bcip-2016-18-natural-recovery-lis-final-report-golderexplor.pdf

Becker, T., Kutzbach, L., Forbrich, I., Schneider, J., Jager, D., Thees, B., & Wilmking, M. (2008). Do we miss the hot spots? - The use of very high resolution aerial photographs to quantify carbon fluxes in peatlands. Biogeosciences, 5, 1387-1393.

Bubier, J., Costello, A., & Moore, T.R. (1993) Microtopography and methane flux in boreal peatlands, northern Ontario, Canada. Canadian Journal of Botany, 71(8), 1056-1063.

Bubier, J. (1995). The relationship of vegetation to methane emission and hydrochemical gradients in northern peatlands. Journal of Ecology, 83(3), 403-420.

Christen, A., Jassal, R. S., Black, T. A., Grant, N. J., Hawthorne, I., Johnson, M. S., … Merkens, M. (2016). Summertime greenhouse gas fluxes from an urban bog undergoing restoration through rewetting, 17(3), 1–24.

Comas, X., Kettridge, N., Binley, A., Slater, L., Parsekian, A., Baird, A. J., … Waddington, J. M. (2014). The effect of peat structure on the spatial distribution of biogenic gases within bogs. Hydrological Processes, 28(22), 5483–5494.

Couwenberg, J., Thiele, A., Tanneberger, F., Augustin, J., Bärish, S., Dubovik, D., … Joosten, H. (2011) Assessing greenhouse gas emissions from peatlands using vegetation as a proxy. Hydrobiologia, 674, 67-89.

Couwenberg, J., & Fritz, C. (2012). Towards developing IPCC methane 'emission factors' for peatlands (organic soils). Mires and Peat, 10(3), 1-17.

Cresto Aleina, F., Runkle, R.K., Kleinen, T., Kutzbach, L., Schneider, J., and Brovkin, V. (2015). Modeling micro-topographic controls on boreal peatland hydrology and methane fluxes. Biogeosciences, 12, 5689-5704.

Dabros, A., Hammond, H.E.J., Piinzon, J., Pinno, B., & Langor, D. (2017). Edge influence of low-impact seismic lines for oil exploration on upland forest vegetation in northern Alberta (Canada). Forest Ecology and Management, 400, 278-288.

Government of Alberta [GoA]. (2017). Climate Leadership Plan: Reducing methane emissions. [online content]. Retrieved from: https://www.alberta.ca/climate-leadership-plan.aspx.

Hartley, I.P., Hill, T.C., Wade,T.J., Clement, R.J., Moncrieff, J.B., Prieto-Blanco, A., … Baxter, R. (2015). Quantifying landscape-level methane fluxes in subarctic Finland using a multiscale approach. Global Change Biology, 21, 3712-3725.

IPCC. (2013). Technical Summary. In: Climate Change 2013: The Physical Science Basis. Contribution of Working Group I to the Fifth Assessment Report of the Intergovernmental Panel on Climate Change. [Stocker, T.F., Qin, D., Plattner, G.-K., Tignor, M., Allen, S.K., Boschung, J., … Midgley, P.M. (eds.)]. Cambridge University Press, Cambridge, United Kingdom and New York, NY, USA. 115pp.

IPCC. (2014a). Climate Change 2014 Synthesis Report. Contribution of Working Groups I, II and III to the Fifth Assessment Report of the Intergovernmental Panel on Climate Change [Core Writing Team, R.K. pachauri and L.A. Meyers (eds.)]. IPCC, Geneva, Switzerland, 151 pp.

IPCC. (2014b). Drivers, Trends and Mitigation. In: Climate Change 2014: Mitigation of Climage Change. Contribution of Working Group III to the Fifth Assessment Report of the Intergovernmental Panel on Climate Change [Edenhofer, O., Pichs-Madruga, R., Sokona,

Y., Farahani, E., Kadner, S., Seyboth, K., … Minx, J.C. (eds.)]. Cambridge University Press, Cambridge, United Kingdom and New York, NY, USA.

Kellner, E., Waddington, J.M., & Price, J.S. (2005). Dynamics of biogenic gas bubbles in peat: Potential effects on water storage and peat deformation. Water Resources Research, 19. doi: 10.1029/2004GB002330

Lee, D. R., & Cherry, J. A. (1979). A field exercise on groundwater flow using seepage meters and mini-piezometers. Journal of Geological Education, 27(1), 6-10.

Lehmann, J.R.K., Munchberger, W., Knoth, C., Blodau, C., Nieberding, F.; Prinz, T., … Kleinebecker, T. (2016). High-Resolution Classification of South Patagonian Peat Bog Microforms Reveals Potential Gaps in Up-Scaled CH4 Fluxes by use of Unmanned Aerial System (UAS) and CIR Imagery. Remote Sensing, 8, 1–19.

Loisel, J., & Yu, Z. (2013). Surface vegetation patterning controls carbon accumulation in peatlands. Geophysical Research Letters, 40, 5508-5513.

Lovitt, J., Rahman, M.M., McDermid, G.J. (2017). Assessing the Value of UAV Photogrammetry for Characterizing Terrain in Complex Peatlands. Remote Sensing. 9(7). 715. doi:10.3390/rs9070715.

Lucieer, a, Robinson, S., & Turner, D. (2011). Unmanned Aerial Vehicle (UAV) remote sensing for hyperspatial terrain mapping of Antarctic Moss beds based on Structure from Motion (SfM) point clouds. Proceeding of the 34th International Symposium on Remote Sensing of Environment, Sydney, Australia, (January 2008), 1–4.

Macrae, M. L., Devito, K. J., Strack, M., & Waddington, J. M. (2013). Effect of water table drawdown on peatland nutrient dynamics: implications for climate change. Biogeochemistry, 112(1–3), 661–676.

Moore, T., & Roulet, N.T. (1993). Methane Flux: Water Table Relations in Nothern Wetlands. Geophysical Research Letter, 20(7), 587-590.

Munir, T. M., Xu, B., Perkins, M., & Strack, M. (2014). Responses of carbon dioxide flux and plant biomass to water table drawdown in a treed peatland in Northern Alberta: A climate change perspective. Biogeosciences, 11(3), 807–820.

National Wetlands Working Group. (1997). The Canadian Wetland Classification System, 2nd Edition. [Warner, B.G. and C.D.A. Rubec (eds.)]. Wetlands Research Centre, University of Waterloo, Waterloo, ON, Canada. 68 p.

Nungesser, M.K. (2003). Modelling microtopography in boreal peatlands: hummocks and hollows. Ecological Modelling, 165, 175-207.

Parish, F., Sirin, A., Charman, D., Joosten, H., Minayeva, T., Silvius, M., & Stringer, L. (2008). Assessment on Peatlands, Biodiversity and Climate Change: Main Report. Kuala Lumpur and Wageningen. https://doi.org/10.1017/CBO9781107415324.004

Pasher, J., Seed, E., & Duffe, J. (2013). Development of boreal ecosystem anthropogenic disturbance layers for Canada based on 2008 to 2010 Landsat imagery. Canadian Journal of Remote Sensing, 39(1), 42-58.

Pouliot, R., Rochefort, L., and Karofeld, E. (2011). Initiation of microtopography in revegetated cutover peatlands. Applied Vegetation Science, 14, 158-171.

Rahman, M.M., J. Lovitt, G.J. McDermid, M. Strack and B. Xu. (2017). Mapping Peat Groundwater Table Dynamics using Unmanned Aerial Vehicle and Photogrammetric Techniques. Remote Sensing, 9(10), 1057. doi:10.3390/rs9101057.

Roosevelt, C. (2014) Mapping site site-level microtopography with Real-Time Kinematic Global Navigation Satellite Systems (RTK GNSS) and Unmanned Aerial Vehicle Photogrammetry (UAVP). Open Archaeology, 2014, 29-53.

Schneider, R. & Dyer, S. (2006). Death by a Thousand Cuts: Impacts of In Situ Oil Sands Development on Alberta's Boreal Forest. Edmonton, AB: Canadian Parks and Wilderness Society and the Pembina Institute.

Shannon, R.D., & White. J.R., (1994). A three-year study of controls on methane emissions from two Michigan peatlands. Biogeochemistry, 27, 35-60.

Strack, M., Cagampan, J., Fard, G.H., Keith, A.M., Nugent, K., Rankin, T., … Xu, B. (2016). Controls on plot-scale growing season CO2 and CH4 fluxes in restored peatlands: Do they differ from unrestored and natural sites? UWSpace: http://hdl.handle.net/10012/11531

Strack, M., Softa, D., Bird, M., & Xu, B. (2017). Impact of winter roads on boreal peatland carbon exchange. Global Change Biology, doi: 10.1111/gcb.13844.

Strack, M., Waller, M.F., & Waddington, J.M. (2006). Sedge Succession and Peatland Methane Dynamics: A Potential Feedback to Climate Change. Ecosystems, 9, 278–287.

Sundh, I., Nilsson, M., Granberg, G., & B.H. Svensson. (1994). Depth distribution fo microbial production and oxidation of methane in northern boreal peatlands. Microbial Ecology, 27(3), 253-265.

Tuittila, E., Komulainen, V., & Vasander, H. (2000). Methane dynamics of a restored cut-away peatland. Global Change Biology, 6, 569-581.

van Rensen, C.K., Nielsen, S.E., White, B., Vinge, T., & Lieffers, V.J. (2015). Natural Regeneration of Forest Vegetation on Legacy Seismic Lines in Boreal Habitats in Alberta's Oil Sands Region. Biological Conservation, 184, 127-135.

van Winden, J.F., Reichard, G-J., McNamara, N.P., Benthien, A., & Damsté, J.S.S. (2012). Temperature-Induced Increase in Methane Release from Peat Bogs: A Mesocosm Experiment. PLoS ONE, 7(6): e39614. Doi: 10.1371/journal.pone.0039614

Vazquez-Amábile, G.G., & Engel, B.A. (2005). Use of SWAT to Compute Groundwater Table Depth and Streamflow in the Muscatatuck River Watershed. Transactions of the ASAE, 48(3), 991-1003.

Vitt, D. H., & Bhatti, J. S. (2012). Restoration and reclamation of boreal ecosystems : attaining sustainable development. Cambridge University Press.

Wieder, R. K., & Vitt, D. H. (2006). Boreal peatland ecosystems. Springer.

Williams, T.J., Quinton, W.L., & Baltzer, J.L. (2013). Linear Disturbances on Discontinuous Permafrost: Implications for Thaw-Induced Changes to Land Cover and Drainage Patterns. Environmental Research Letters, 8(2), doi: 10.1008/1748-9326/8/2/025006.

Xu, K., Kong, C., Liu, J., & Wu, Y. (2010). Using Methane Dynamic Model to Estimate Methane Emission from Natural Wetlands in China. 18th International Conference on Geoinformatics. Beijing, Hebei: IEEE.

Chapter Four: Conclusions

The link between ecosystem disturbance and increased greenhouse gas (GHG) release is well-documented in eastern Canadian peatland complexes (Strack & Waddington, 2012; Strack & Zuback, 2013; Macrae et al., 2013). However, very little research to date has focused on how western Canadian Boreal peatlands respond to small-scale disturbances such as seismic lines and other non-mineral-fill related linear features (power transmission lines, winter roads, pipelines, etc). Though more recently constructed seismic lines are considered low-impact due to their relatively small local scale (2m widths), it is anticipated their high-density construction design will have significant, compounding effects on peatland surface conditions and hydrology, and therefore GHG flux (Weider & Vitt, 2006; Graf, 2009). The research presented here strives to address this knowledge gap by describing methods for leveraging cost-effective UAV technology to characterize and assess terrain (microtopography) within a complex peatland of northern Alberta, Canada. These methods are based on the assumption that microtopography indirectly describes environmental conditions controlling peatland GHG generation and distribution, and can therefore be used to predict changes in CH_4 release between disturbed and undisturbed areas. Results of this research indicate that UAVs are suitable for mapping peatland microtopography under all but the most complex surface conditions, and provide the first-known spatially explicit quantification of seismic-lines impacts on physical peatland parameters (hydrology and microtopography), and CH_4 emission. These findings suggest that it is vital to include estimates of linear features when calculating peatland carbon stocks, specifically in the sedimentary basin of western Canada, where seismic-line disturbances are ubiquitous (Schneider & Dyer, 2006).

4.1 Research Objectives Summary

The overall goal of this research was to assess the suitability for UAVs to map and classify peatland terrain, and to use these data to estimate seismic line impacts on peatland surface, hydrology, and methane emission. The research objectives were as follows:

1. To assess the capacity of UAV photogrammetry for modelling microtopography in complex peatland systems within Alberta by:
    a. Assessing the accuracy of modelling peatland microtopography using UAV photogrammetry, and
    b. Developing a method for characterizing (classifying) peatland surface morphology using UAV imagery
2. To quantify the impact of seismic lines on physical environmental parameters (microtopography and depth-to-water), and CH_4 emission, in a typical treed bog of northern Alberta

A summary of research activities made in addressing these objectives is summarized below:

- (Objective 1a) A review of the literature, as summarized in Chapter 1, revealed the need for an efficient and economical method for collecting the spatially explicit, high-resolution data required to accuratly map peatland microtopography, and capture CH_4 hotspots across the larger landscape. While unmanned aerial vehicles (UAVs) fitted with passive sensors have been shown promise in open peatland complexes, they had yet to be tested in the more complex treed peatlands of western Canada. As the use of UAVs was critical to this research program, I completed an accuracy assessment to determine whether models developed from the UAV data would be of sufficient quality to proceed with the subsequent

research objectives. As part of this assessment, I also tested whether the UAV point cloud could be enhanced by using complimentary LiDAR data to fill in data gaps caused by densely treed vegetation. Results of this assessment revealed that UAV photogrammetry data alone are appropriate for collecting microtopographic data under all but the most-complex surface conditions of a treed bog, with no notable benefit found by incorporating LiDAR. Additionally, there was no significant difference in UAV model accuracies in areas disturbed by linear features (pipeline, seismic lines etc.) and sparsely treed undisturbed peatland areas. This lead to the conclusion that UAVs are appropriate platforms for collecting peatland microtopographic data, and also for comparing peatland surface conditions between undisturbed peatland and areas disturbed by linear features. This second conclusion was essential to proceed with the quantification of seismic line impacts on the treed bog ecosystem (Research Objective 2).

- (Objective1b). Once the accuracy assessment had been completed, a method of converting ground elevation data to meaningful microtopographic information had to be developed. There were two main reasons for completing this objective: 1) to facilitated meaningful comparisons of microform characteristics in undisturbed and disturbed (via seismic line) areas, and 2) to use the classified surface in quantifying seismic line impacts on CH_4 emission, and up-scale CH_4 flux to the larger study area (Research Objective 2). I devised a simple classification scheme, based on the assumption that elevations greater than the local (2m) average would correspond with hummocks, while those below the local average would correspond with hollows. Applying this workflow to the digital terrain model

effectively divided the study area into meaningful classes of hummocks, hollows, and trees (masked areas). Assessment of the classification confusion matrix indicated that the overall accuracy was sufficiently high (84%) for use in characterizing CH_4 flux. This approach to microform classification was highly successful in differentiating tall hummocks and deep hollows, but performed less well when differentiating smaller microforms within 5cm of the local (2m) average surface. Results could potentially be improved with further segregation of the hummocks and hollows classes. In particular, the identification of a transitional microform class, which would capture points ±5cm of the local average surface, would likely address the majority of commission errors.

- (Objective 2) The final objective was to quantify seismic line impacts on peatland environmental conditions and CH_4 emissions. To quantify seismic line impacts on peatland environmental conditions and CH4 emissions, I used the microtopographic (MT) surface (from 1b) and a depth-to-water (DTW) surface generated by a colleague (Rahman et al., 2017) to estimate CH_4 emission across the study area. A thorough comparison of undisturbed peatland conditions (MT, DTW, and CH_4 flux) and those of areas disturbed by seismic lines was then completed. Results of this assessment reveal significant differences between undisturbed peatland conditions and those of seismic lines. In particular, dramatic increases in CH_4 release (up to 120% per linear kilometer) was estimated along seismic lines. Predicted CH_4 flux was found to be significantly different between the two surfaces (MT and DTW) when modeling undisturbed peatland areas, but not along seismic lines. Additional data is required to determine which model more accurately estimates flux within

the undisturbed peatland areas. Results of the microform comparison indicate peatland microtopography was flattened along seismic lines, with a reported maximum decrease in hummock height of 33cm and maximum decrease in hollow depth of 10cm. Additionally the water table position was found to be shallower by 15.5cm (on average) along seismic lines when compared with DTW of undisturbed areas. When considered cumulatively, these seismic-line impacts appear to be severe as they not only result in greater CH_4 release from the peatland, but generate low and wet environmental conditions which are unfavourable for natural ecosystem recovery (Rensen et al., 2015), thus suggesting these impacts may be long-lasting. All seismic lines assessed in this study were approximately 2m wide and are therefore classified as 'low-impact' under current industry and regulatory standards. This investigation reveals the true effect of these lines on peatland surface conditions and CH_4 release, and wider lines are anticipated to cause even greater impacts.

To conclude, the research objectives posed in this thesis were achieved successfully. UAV data was found to be appropriate for modeling peatland terrain, and methods were developed to utilize this data to quantify the impacts of seismic lines on a western Canadian peatland ecosystem. The potential to use cost-effective UAV platforms to model these complex peatlands opens the door for future research on how linear disturbance features are altering these sensitive ecosystems.

4.2 Research Contributions

Research undertaken in this thesis has resulted in a number of methodological and theoretical contributions to the fields of remote sensing and peatland monitoring. Peatlands of western Canada are extremely complex ecosystems, and as such are difficult to model. However it is vital to

improve the accuracy of estimated peatland carbon stocks and carbon balance models to better inform global climate change policies and predictive models. Therefore, the main contribution of this research is the first-known spatially explicit quantification of seismic-line impact assessment on peatland morphology, hydrology, and GHG flux. As part of this contribution, the demonstrated application of UAV technology to successfully derive these estimates is significant, as the suitability of these platforms for use in treed bog ecosystems had not previously been assessed. The methods developed during the completion of this research are fairly straight-forward, with the potential to be applied across a variety of study sites.

This research has the potential to assist with the development of provincial legislation regarding linear-feature restoration requirements within the Boreal region of western Canada. My work shows that seismic lines create lower, wetter areas within the treed-bog system I worked in, leading to increased methane release and likely reducing the chance of re-establishing a comparable ecosystem (Rensen et al., 2015). With improved methods of mapping undisturbed peatland conditions, clear microtopographic restoration standards could be mandated for disturbed Boreal peatlands (ie. minimum microform heights and frequencies) as part of provincial land-use guidelines. Currently, many regional plans which include intents to restore seismic lines within Boreal areas are written with a focus on woodland caribou habitat, rather than greenhouse gas potential or peatland microtopography (GoA, 2016). As such it appears significant environmental factors are being omitted from the legislation which, if included, may ultimately increase the chance of successfully achieving overall restoration of ecosystem functions.

Other contributions include:

1. The development of ten methodological tutorials (Appendix A) which were shared internally, and used as laboratory material of undergraduate classes. The titles of these tutorials are:
    i. Downloading Files from the Trimble R4 or R8 and Determining RTK Accuracies
    ii. Point Cloud Generation in Agisoft PhotoScan
    iii. Re-projecting Point Clouds using LAStools
    iv. Updating Image Pathways in PhotoScan
    v. Extracting Ground from Dense Point Clouds (when the PhotoScan Point Classification Tool is Inadequate)
    vi. Converting Ground Point Clouds to DTMs and Model Validation in ESRI ArcMap
    vii. Applying Filters to Masked Images in ENVI
    viii. OBIA in eCognition with Accuracy Assessment in ESRI ArcMap
    ix. GCP Design Considerations – Review of Problems from 2016 Peatlands Research Project
    x. How to Bust Clusters in PCI Geomatica
2. Personally prepared a written summary of the overall peatland research project and arranged for it to be showcased in Duck Unlimited Canada's Wetland Best Management Knowledge Exchange, (DU, 2017).
3. Select material from Chapter 2 was presented at the Earth Observation Summit in Montreal on June 21, 2017 (Lovitt et al., 2017b), as well as a second 15 minute oral presentation of work completed by a project partner describing the generation and accuracy assessment of the DTW surface (Rahman et al., 2017b).

4. The published manuscript (Lovitt, Rahman & McDermid, 2017 [Chapter 2]), peer-reviewed article (Rahman et al., 2017a), and one article currently in review (Lovitt et al., 2017a [Chapter 3]), represent formal contributions to the literature and broader body of knowledge.

4.3 Recommendations for Future Research

While this thesis represents numerous research contributions, there remains a number of points which would benefit from additional analysis and more thorough investigation. The areas of future research identified as most important are summarized below.

Firstly, alternative methods of filtering trees and other vegetation from the dense point cloud should be investigated. During the ground-point extraction workflow (as described in Chapter 2) it became apparent that the software packages I used (PhotoScan, LAStools and Cloud Compare) struggle in correctly distinguishing true ground points from those representing low-hanging branches at the edge of tree boundaries. This weakness was attributed to the software filtering tools, which rely primarily upon point isolation and elevation-spike thresholds, which do not perform well when point clouds are very dense. Had these points been included in the dataset, they would have caused an inappropriate localized overestimation of ground-surface elevations which would have negatively influenced results. I dealt with this issue through the application of an 18-pixel buffer to masked treed areas, but this approach likely also masked out valid ground points. The extraction of accurate ground points affects all subsequent steps of analysis, and is therefore a crucial step. Furthermore, the current methodology for extracting ground points is computationally expensive, as it requires data processing with three separate software packages

(PhotoScan, LAStools and Cloud Compare). Therefore, additional research focusing on improving dense-point-cloud filtering tools and workflows would also be beneficial. LAStools has a very active user base, with new tool applications being reported and discussed every week. One such release (July 4, 2017) described a workflow for correctly classifying excessive low noise in dense point clouds (Isenburg, 2017). Although this workflow does not directly address the aforementioned issue of limited above-ground vegetation filtering, it does describe methods of point filtering based on expected values (ie. searching within specific ranges of accepted ground maxima) which could be used to improve vegetation filtering in this work.

Microform classification methods developed through this research could also be refined and improved with further analysis. The simple density slicing approach utilized in this project was applied after an assessment of alternate methods, including a combination of spectral and elevation data, and object-based image analysis (OBIA). I found that spectral differences between hummocks and hollows did not exist consistently across the large study area. Therefore, the RGB data did not contribute significantly to microform identification across the bog, and so classification was based exclusively upon relative elevation thresholds. Data used in the classification workflow was collected in September, which is fairly late in the growing season, and produced an orthophoto slightly more blurry than the July data. However, this data was used as the July dataset had extremely dark shadows which obscured a great deal of ground in the orthophoto. It is likely that enhanced flight-mission planning, designed to capture data in the spring under diffuse, bright-light conditions, could address the issue of limited spectral contribution to microform classification. This is based on the assumption that spectral differences between hummocks and hollows are less obvious later in the growing season (ie. September) than they are

in the spring. Additionally, experimenting with different flight parameters such as altitude, overlap and sensors (ie. NIR) may improve microform classification results (Lehmann et al., 2016).

Gathering additional flux measurements over a variety of microform heights would allow for greater segregation of microform classes in the MT surface. Incorporating more classes may improve CH_4 estimates from the MT surface in undisturbed portions of the bog. In particular, establishing an appropriate flux to assign to a 'transitional' microform class (or 'lawn' class) would address weaknesses identified in the classification workflow. Similarly, supplementary data could be used to assess overall accuracy of both predictive surfaces (MT & DTW), and determine which method is superior for estimating CH_4 flux. Future research focusing on repeating this study, or conducting similar studies, over a variety of peatland types and environmental conditions would contribute to a better understanding of Boreal peatland ecosystem function and response to disturbances within western Canada. For example, UAV data could be used to estimate emissions of other greenhouse gases (ie. CO_2), or to investigate vegetation differences along seismic lines and other linear features, potentially extending into comparative impact assessments of mineral fill linear features (ie. roads and pipelines) vs non-mineral fill linear features (ie. seismic lines and power lines).

This brief summary is by no means a complete review of all potential future research opportunities, rather it is meant to showcase points which emerged as a direct result of the methodologies developed through this project. ☙

4.4 Bibliography

Acharya, S., Kaplan, D.A., Casey, S., Cohen, M.J., & Jawitz, J.W. (2015). Coupled local facilitation and global hydrologic inhibition drive landscape geometry in a patterned peatland. Hydrology and Earth System Sciences, 19, 2133-2144.

Alberta Environment and Sustainable Resource Development [ESRD]. (2015). Alberta Wetland Classification System. Water Policy Branch, Policy and Planning Division, Edmonton, AB.

Belyea, L., & Malmer, N. (2004). Carbon sequestration in peatland: patterns and mechanisms of response to climate change. Global Change Biology, 10, 1043-1052.

Brandt, J.P., Flannigan, M.D., Maynard, D.G., Thompson, I.D., & Volney, W.J.A. (2013). An introduction to Canada's boreal zone: ecosystem processes, health, sustainability, and enviornmental issues. Environmental Reviews, 21(4), 207-226.

Bridgham, S.D., Cadillo-Quiroz, H., Keller, J.K., and Qianlaizhuang. (2013). Methane emissions from wetlands: biogeochemical, microbial, and modeling perspectives from local to global scales. Global Change Biology, 19, 1325-1346.

British Columbia Oil and Gas Commission [BC OGC]. (2016). Natural Recovery on Low Impact Seismic Lines in Northeast British Columbia (BCIP-2016-18). Victoria, BC: Golder Associates.

Bubier, J., Costello, A., Moore, T.R., Roulet, N.T., & Savage, K. (1993). Microtopography and methane flux in boreal peatlands, northern Ontario, Canada. Canadian Journal of Botany, 71(8), 1056-1063.

Chimner, R.A., Cooper, D.J., Wurster, F.C., and Rochefort, L. (2016) An overview of peatland restoration in North America: where are we after 25 years? Restoration Ecology. 25: 283-292.

Chisholm, R.A., Cui, J., Lum, S.K.Y. & Chen, B.M. (2013). UAV LiDAR for below-canopy forest surveys. Unmanned Vehicle Systems, 1, 61-68.

Comas, X., Kettridge, N., Binley, A., Slater, L., Parsekian, A., Baird, A.J., Strack, M. & Waddington, J.M. (2014). The effect of peat structure on the spatial distribution of biogenic gases within bogs. Hydrological Processes, 28 (22), 5483-5494.

Couwenberg, J., & Joosten, H. (2005). Self-organization in raised bog patterning: the origin of microtope zonation and mesotope diversity. Journal of Ecology, 93, 1238-1248.

Couwenberg, J., Thiele, A., Tanneberger, F., Augustin, J., Bärisch, S., Dubovik, D., … Joosten, H. (2011) Assessing greenhouse gas emissions from peatlands using vegetation as a proxy, Hydrobiologia, 674, 67-89.

Cresto Aleina, F., Runkle, R.K., Kleinen, T., Kutzbach, L., Schneider, J., & Brovkin, V. (2015). Modeling micro-topographic controls on boreal peatland hydrology and methane fluxes. Biogeosciences, 12, 5689-5704.

Dabros, A., Hammond, H.E.J., Piinzon, J., Pinno, B., & Langor, D. (2017). Edge influence of low-impact seismic lines for oil exploration on upland forest vegetation in northern Alberta (Canada). Forest Ecology and Management, 400, 278-288.

Ducks Unlimited Canada [DU]. (2017). Improved construction to minimize greenhouse gas emissions. Wetland BMP Knowledge Exchange. Issue 11(May, 2017). Retrieved from: http://mailchi.mp/72186041f158/may-2017-wetland-bmp-knowledge-exchange-newsletter?e=36733ef23a.

Eisenbeiß, H. (2009). UAV Photogrammetry (Doctoral dissertation). Retrieved from http://www.igp-data.ethz.ch/berichte/blaue_Berichte_PDF/105.pdf

Eppinga, M.B., Rietkerk, M., Wassen, M.J., & De Ruiter, P.C. (2009). Linking habitat modification to catastrophic shifts and vegetation patterns in bogs. Plant Ecology, 200, 53-68.

Farmer, J., Matthews, R., Smith, J.U., Smith, P. & Singh, B.K. (2011). Assessing existing peatland models for their applicability for modelling greenhouse gas emissions from tropical peat soils. Current Opinion in Enviornmental Sustainability, 3, 339-349.

Food and Agriculture Organization of the United Nations [FAO]. (2014). Towards climate-responsible peatlands management. Retrieved from http://www.fao.org/3/a-i4029e.pdf

Fritz, A., Kattenborn, T., & Koch, B. (2013). UAV-Based Photogrammetric Point Clouds - Tree STEM Mapping in Open Stands in Comparison to Terrestrial Laser Scanner Point Clouds. International Archives of the Photogrammetry, Remote Sensing and Spatial Information Sciences, 40, 141-146.

González, E., & Rochefort, L. (2014). Drivers of success in 53 cutover bogs restored by a moss layer transfer technique. Ecological Engineering, 68, 279-290.

Government of Alberta [GoA]. (2016). Little Smoky and A La peche Caribou Range Plan (DRAFT). [online content]. Retrieved from: http://aep.alberta.ca/fish-wildlife/wildlife-management/caribou-management/caribou-action-range-planning/documents/LittleSmokeyAlaPecheRangePlan-Draft-Jun2-2016.pdf

Graf, M.D. (2009). Literature Review on the Restoration of Alberta's Boreal Wetlands Affected by Oil, Gas and In Situ Oil Sands Development. Prepared for Ducks Unlimited Canada. Retrieved from http://www.biology.ualberta.ca/faculty/stan_boutin/ilm/uploads/footprint/Graf%20Wetland_Restoration_Review%20FINAL-Small%20File.pdf

Hartley, I.P., Hill, T.C., Wade,T.J., Clement, R.J., Moncrieff, J.B., Prieto-Blanco, A., … Baxter, R. (2015). Quantifying landscape-level methane fluxes in subarctic Finland using a multiscale approach. Global Change Biology, 21, 3712-3725.

Hogg, E. H. (1993). Decay potential of hummock and hollow Sphagnum peats at different depths in a Swedish raised bog. OIKOS, 66, 269-278.

Isenburg, M. (2017). Removing Excessive Low Noise from Dense-Matching Point Clouds. [online content]. Retrieved from: https://rapidlasso.com/2017/07/04/removing-excessive-low-noise-from-dense-matching-point-clouds/

Joosten, H. & Couwenberg, J. (2009). Are emission reductions from peatlands MRV-able? [online content] Retrieved from: http://www.wetlands.org/WatchRead/tabid/56/mod/1570/articleType/ArticleView/articleId/2294/Default.aspx

Kalacska, M., Arroyo-Mora, J.P., de Gea, J., Snirer, E., Herzog, C., & Moore, T.R. (2013). Videographic Analysis of Eriophorum Vaginatum Spatial Coverage in an Ombotrophic Bog. Remote Sensing, 5, 6501-6512.

Knoth, C., Klein, B., Prinz, T., & Kleinebecker, T. (2013). Unmanned aerial vehicles as innovative remote sensing platforms for high-resolution infrared imagery to support restoration monitoring in cut-over bogs. Applied Vegetation Science, 16, 509-517.

Lechner, A.M., Fletcher, A., Johansen, K., & Erskine, P. (2012). Characterising upland swamps using object-based classification methods and hyper-spatial resolution imagery derived from an unmanned aerial vehicle. ISPRS Annals of the Photogrammetry, Remote Sensing and Spatial Information Sciences, 1(4), 101-106.

Lee, P., & Boutin, S. (2006). Persistence and developmental transition of wide seismic lines in the western Boreal Plains of Canada. Journal of Environmental Management, 78, 240-250.

Lefsky, M.A., Cohen, W.B., Parker, G.G., & Harding, D.J. (2002). Lidar Remote Sensing for Ecosystem Studies. BioScience, 52(1), 19 - 30.

Lehmann, J.R.K., Munchberger, W., Knoth, C., Blodau, C., Nieberding, F., Prinz, T., … Kleinebecker, T. (2016). High-Resolution Classification fo South Patagonian Peat Bog Microforms Reveals Potential Gaps in Up-Scaled CH4 Fluxes by use of Unmanned Aerial System (UAS) and CIR Imagery. Remote Sensing, 8(173), 1-19.

Lejot, J., Delacourt, C., Piégay, H., Fournier, T., Trémélo, M-L. & Allemand, P. (2007). Very high spatial resolution imagery for channel bathymetry and topography from an unmanned mapping controlled platform. Earth Surface Processes and Landforms, 32, 1705-1725.

Limpens, J., Berendse, F., Blodau, C., Canadell, J.G., Freeman, C., Holden, J., … Schaepman-Strub, G. (2008). Peatlands and the carbon cycle: from local processes to global implications - a synthesis. Biogeosciences, 5, 1475-1491.

Lovitt, J., Rahman, M.M., & McDermid, G.J. (2017). Assessing the Value of UAV Photogrammetry for Characterizing Terrain in Complex Peatlands. Remote Sensing, 9(7), 715.

Lovitt, J., Rahman, M.M., McDermid, G.J., Strack, M., & Xu, B. (2017b) Mapping Micro-Topography of Peatlands within Alberta: Applications for Unmanned Aerial Vehicle (UAV) Technology. Earth Observation Summit 2017, Montreal, Quebec.

Lovitt, J., Rahman, M.M., Saraswati, S., McDermid, G.J., Strack, M., & Xu, B. (2017a). UAV Remote Sensing Can Reveal the Effects of Low-Impact Seismic Lines on Methane Release in a Forested Boreal Bog. Journal of Geophysical Research: Biogeosciences. [In Review].

Lucieer, A., Robinson, S.A., & Bergstrom, B. (2010). Aerial 'OktoKopter' to map Antarctic moss. Australian Antarctic Magazine, 19, 2010.

Lucieer, A., Turner, D., King, D.H., & Robinson, S.A. (2014). Using an Unmanned Aerial Vehicle (UAV) to capture micro-topography of Antarctic moss beds. International Journal of Applied Earth Observation and Geoinformation, 27, 53-62.

Macrae, M. L., Devito, K.J., Strack, M., & Waddington, J.M. (2013). Effect of water table drawdown on peatland nutrient dynamics: implications for climate change. Biogeochemistry, 112, 661-676.

McCarter, C.P.R. & Price, J.S. (2012). Ecohydrology of Sphagnum moss hummocks: mechanisms of capitula water supply and simulated effects of evaporation. Ecohydrology, 7(1), 33-44.

Mesas-Carrascosa, F.J., Inmaculada, C.R., Barrera Berrocal, J.A., & García-Ferrer Porras, A. (2014). Positional Quality Assessment of Orthophotos Obtained from Sensors Onboard Multi-Rotor UAV Platforms. Sensors, 14, 22394-22407.

Munir, T.M., Xu, B., Perkins, M., & Strack, M. (2014). Responses of carbon dioxide flux and plant biomass to water table drawdown in a treed peatland in northern Alberta: a climate change perspective. Biogeosciences, 11, 807-820.

National Wetlands Working Group (NWWG). (1997). The Canadian Wetland Classification System. (2nd ed.). Waterloo, ON: University of Waterloo.

Nungesser, M. K., (2003). Modelling microtopography in boreal peatlands: hummocks and hollows. Ecological Modelling, 165, 175-207.

Parish, F., Sirin, A., Charman, D., Joosten, H., Minanyeva, T., Silvius, M. & Stringer, L. (Eds.) (2008). Assessment on Peatlands, biodiversity and Climate Change: Main Report. Global Environmental Centre, Kuala Lumpur and Wetlands International, Wageningen.

Pattison, C.A., Quinn, M.S., Dale, P., and Catterall, C.P. (2016). The Landscape Impact of Linear Seismic Clearings for Oil and Gas Development In Boreal Forest. Northwest Science. 90(3): 340-354.

Pirotti, F., & Tarolli, P. (2010). Suitability of LiDAR point density and derived landform curvature maps for channel network extraction. Hydrological Processes, 24, 1187-1197.

Pouliot, R., Rochefort, L., & Karofeld, E. (2011). Initiation of microtopography in revegetated cutover peatlands. Applied Vegetation Science, 14, 158-171.

Quinty, F., & Rochefort, L. (2003). Peatland Restoration Guide: Second Edition, Canadian Sphagnum Peat Moss Association and New Brunswick Department of Natural Resources and Energy.

Rahman, M.M., G.J. McDermid, M. Strack and J. Lovitt (2017a). A New Method to Map Groundwater Table in Peatlands Using Unmanned Aerial Vehicles. Remote Sensing, 9(10), 1057. doi: 10.3390/rs9101057.

Rahman, M.M., J. Lovitt, G.J. McDermid, M. Strack and B. Xu. (2017b). Mapping Peat Groundwater Table Dynamics using Unmanned Aerial Vehicle and Photogrammetric Techniques. Earth Observation Summit 2017, Montreal, Quebec.

Rochefort, L. (2000). Sphagnum – A Keystone Genus in Habitat Restoration. The Bryologist, 103(3), 503-508.

Rochefort, L., Strack, M., Poulin, M., Price, J.S., Graf, M., Desrochers, A., Lavoie, C., & Lapointe, L. 2012. Northern peatlands, In Wetland Habitats of North America: Ecology and Conservation Concerns, Batzer, D., Baldwin, A. (eds.), University of California Press, Berkeley, California, USA, pp. 119-134.

Roosevelt, C. (2014) Mapping site site-level microtopography with Real-Time Kinematic Global Navigation Satellite Systems (RTK GNSS) and Unmanned Aerial Vehicle Photogrammetry (UAVP). Open Archaeology, 2014, 29-53.

Scharlemann, J.P., Tanner, E.V., Hiederer, R., and V. Kapos. (2014). Global soil carbon: understanding and manageing the largest terrestrial carbon pool. Carbon Management, 5(1), 81-91.

Schneider, R. & Dyer, S. (2006). Death by a Thousand Cuts: Impacts of In Situ Oil Sands Development on Alberta's Boreal Forest. Edmonton, AB: Canadian Parks and Wilderness Society and the Pembina Institute.

Shi, X., Thornton, P.W., Ricciuto, D.M., Hanson, P.J., Sebestyen, S.D., Griffiths, N.A., & G. Bisht. (2015). Representing northern peatland microtopography and hydrology within the Community Land Model. Biogeosciences, 12, 6463-6477.

Strack, M. (Ed.). (2008). Peatlands and Climate Change. Saarijärvi, FIN: International Peat Society (IPS).

Strack, M., & Waddington, J.M. (2007). Response of peatland carbon dioxide and methane fluxes to a water table drawdown experiment. Global Biogeochemical Cycles, 21, 1-13.

Strack, M., & Waddington, J.M. (2012). Effects of peat extraction and restoration on greenhouse gas exchange from Canadian peatlands. In Vitt, D., and Bhatti, J. (Eds.), Restoration and Reclamation of Boreal Ecosystems (386-403). Cambridge: Cambridge University Press.

Strack, M., & Zuback, Y.C.A. (2013). Annual carbon balance of a peatland 10 yr following restoration. Biogeosciences, 10, 2885-2896.

Strack, M., Waddington, J.M., Rochefort, L., & Tuitilla, E.S. (2006). Response of vegetation and net ecosystem carbon dioxide exchange at different peatland microforms following water table drawdown. Journal of Geophysical Research, 111, 1-10.

Sturm, P., & Triggs, B. (1996). A factorization based algorithm for multi-image projective structure and motion. In Proceedings of the 4th European Conference on Computer Vision, Cambridge, UK, 15–18 April 1996.

Turetsky, M.R., Kotowska, A., Bubier, J., Dise, N.B., Crill, P., Hornibrook, E.R.C., … Wilmking, M. (2014). A synthesis of methane emissions from 71 northern, temperate, and subtropical wetlands. Global Change Biology, 20, 2183-2197.

Turner, D., Lucieer, A., & Wallace, L. (2014). Direct Georeferencing of Ultrahigh-Resolution UAV Imagery. IEEE Transactions on Geoscience and Remote Sensing, 52(5), 2738-2745.

Turner, D., Lucieer, A., & Watson, C. (2012). An Automated Technique for Generating Georectified Mosaics from Ultra-High Resolution Unmanned Aerial Vehicle (UAV) Imagery, Based on Structure from Motion (SfM) Point Clouds. Remote Sensing, 4(5), 1392-1410.

van Rensen, C.K., Nielsen, S.E., White, B., Vinge, T., & Lieffers, V.J. (2015). Natural regeneration of forest vegetation on legacy seismic lines in boreal habitats in Alberta's oil sands region. Biological Conservation, 184, 127-135.

Vitt, D. & Bhatti, J. (2012). Restoration and Reclamation of Boreal Ecosystems: Attaining Sustainable Development. Cambridge: Cambridge University Press.

Webster, K.L., F.D. Beall, I.F. Creed, and D.P. Kreutzweiser. (2015). Impacts and prognosis of natural resource development on water and wetlands in Canada's boreal zone. Environmental Reviews. 23(1): 78-131.

Wieder, R.K. & Vitt, D. H. (2006) Boreal Peatland Ecosystems. Verlag Berlin Heidelberg. Germany: Springer.

Wu, J., Roulet, N. T., Moore, T. R., Lafleur, P., & Humphreys, E. (2010). Dealing with microtopography of an ombrotrophic bog for simulating ecosystem-level CO2 exchanges. Ecological Modelling, 222, 1038-1047.

Yu, Z.C. (2012). Northern peatland carbon stocks and dynamics: a review. Biogeosciences, 9, 4071-4085.

Yu, Z.C., Loisel, J, Brosseau, D.P., Beilman, DW, & Hunt, S.J. (2010). Global peatland dynamics since the Last Glacial Maximum. Geophysical Research Letters, 37(13), L13402.

Zhu, Q., Liu, J., Peng, C., Chen, H., Fang, X., Jiang, H., … Zhou, X. (2014). Modelling methane emissions from natural wetlands by development and application of the TRIPLEX-GHG model. Geoscientific Model Development, 7, 981-999.

Appendix A: Tutorials

A(I) Downloading Files from the Trimble R4 or R8 and Determining RTK Accuracies

This tutorial will help you download survey data from the department RTK units (Trimble R4 and R8). If you have questions on how to download the files from the lab RTK (Hemisphere) please ask Mustafiz. These instructions are partially from Derek and partially from my own fiddling so if you find a more streamlined approach please update this file!
You will be downloading **two** files from the RTK unit:

1. A comma delimited file which includes your surveyed data: points, lines and/or polygons
2. An HTML 'survey summary report' file which includes recorded RTK accuracies for each of your features during the survey

On the Trimble Hand-held unit: Export your files

Step 1: Open your desired file on the handheld unit

General Survey > Jobs > Open File

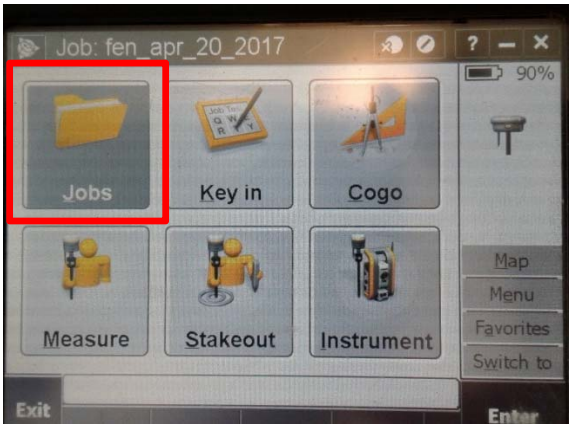

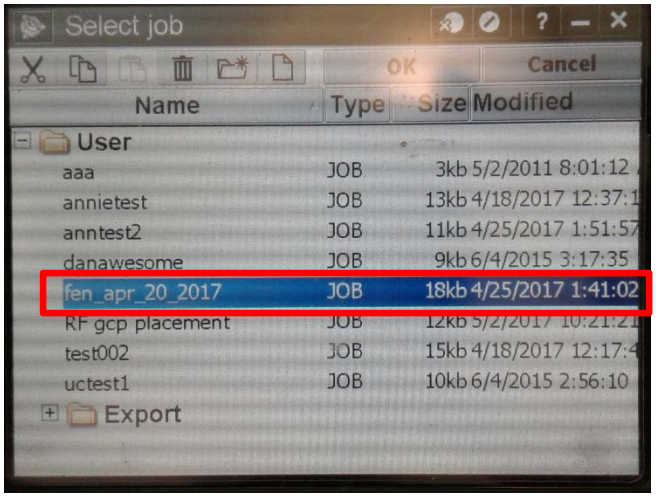

Step 2: Export the survey data as a .CSV file

Jobs > Import/Export > Export fixed format* > CSV**

*make sure the selected file name matches the file you wish to export

** you can customize the column your data goes into. The default will give you data in the order: Point Name, Northing, Easting, Elevation, Code

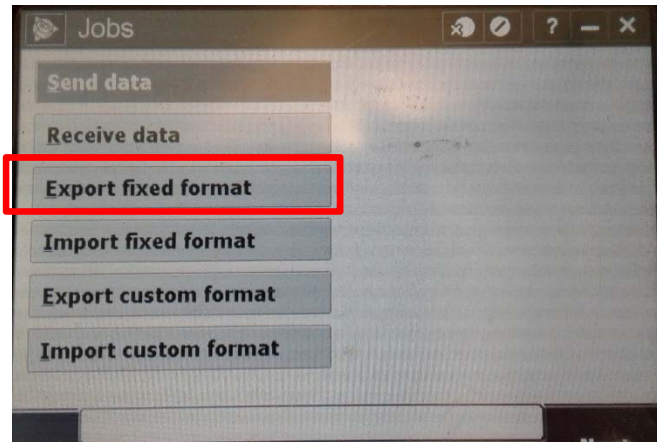

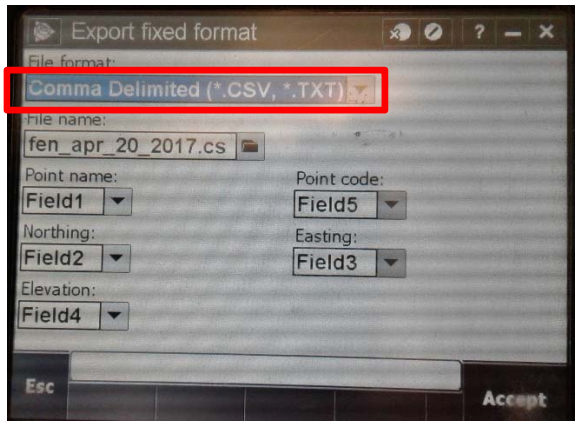

Step 3: Export your survey summary report as HTML

Jobs > Import/Export > Survey report > HTML

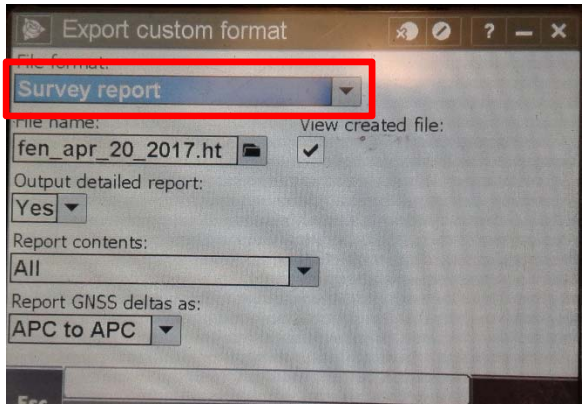

On your computer: Download the files

Step 4: Download files from handheld unit to computer

1. Plug in the handheld unit to your computer using the cable included in the kit
2. Navigate to the Trimble unit on your computer, and the job folder which contains your file
3. There should be an 'Export' folder, open it and copy or move your desired files to a new location on your computer

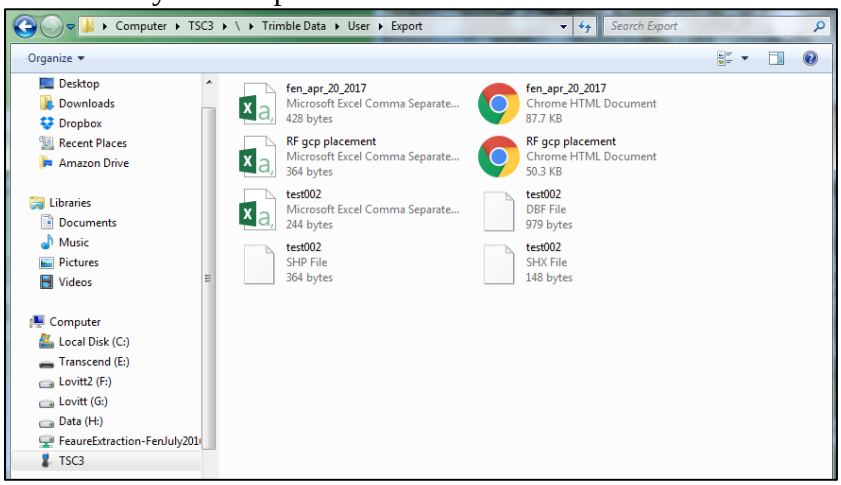

Step 6: Extract recorded RTK point accuracies to your survey data file (In Excel)

Accuracies are reported along with a lot of additional information for each point collected by the RTK. As far as I know there is no other way to get the estimated accuracies for each point other than exporting the survey summary report and using the following formula in Excel which I developed last summer. If you come across a better method, please update this file and let the lab know.

1. Open both files in Excel
    a. Combine all RTK points into an excel file if necessary*
    b. Combine all accuracy reports into excel file and unmerge cells
        i. Convert html file to excel

1. Open HTML > Save as > .xlsx format

ii. Select all cells in file (ctrl + A) and unmerge

iii. If necessary use:
    1. Find & Select > Format > Merged Cells > Find All
    2. Select all returned merged cells and hit 'Merge & Center'
    3. If merged cells are present the formula in step 3 will not work, so use this method to ensure all merged cells are unmerged

**If necessary. For example: if you are doing this at the end of the summer rather than for each downloaded file as you create them during the summer*

2. In your survey data (points) file create two new column entries with meaningful titles to represent the reported RTK accuracy in the horizontal and vertical directions.
    a. For example: "Hz_Accuracy_Reported" and "Vt_Accuracy_Reported"
3. Use Index and Matchup formula combination to find reported Hz and Vt accuracies for each point in your survey file

Formula:

=INDEX('array', MATCH(lookup_value, lookup_array, match_type)±X)

Where:

Array = **Desired column to return values** (ex. Horizontal accuracies in accuracy file)

Lookup_value = **Single cell entry to search for** (ex. One point ID)

Lookup_array = **Desired column to match entry with the lookup_value**

(ex. Corresponding point ID in survey file)

Match_type = **Type of match, exact match = 0** (represents an exact match)

±X = **Adjustment to returned cell location**

(ex. +2 = return cell value from searched column which is 2 below the matched cell row location [point ID]. Adjust this if your notice the desired accuracy is reported in a different location, ie. +3 would return the value in the cell which is three cells below the row of the matched point ID)

Example:

=INDEX('H:\UofC\Data Analysis\7. Validation Point Accuracies\sibbald\[sibb_all_accuracies.xlsx]Sheet1'!$F2:$F9000,MATCH(A3,'H:\UofC\Data Analysis\7. Validation Point Accuracies\sibbald\[sibb_all_accuracies.xlsx]Sheet1'!$B2:$B9000,0)+2)

4. Don't forget to save the entries as numbers once you are sure you have copied the correct values. If you leave them as a formula and decide to delete or move the files they reference the values will disappear so it's always best to save them as numbers in your survey data file.

A(II) Point Cloud Generation in Agisoft PhotoScan

Files to use with this tutorial (in shared Google drive or use your own data):

Aerial Photographs	Images folder
Georeferencing GCP locations (x,y,z)	Georeference.csv
Validation GCP locations (x,y,z)	Validation.csv
Google Earth GCP locations to assist with locating	Bog_Site_Lab.kml
A list of which images show which GCPs	GCP_IMGS.xlsx

If you have questions as you go through this tutorial you may reference the Agisoft PhotoScan Professional Edition User Manual: http://www.agisoft.com/pdf/photoscan-pro_1_2_en.pdf.

Agisoft PhotoScan Processing Workflow:

Loading Photos (Estimated Time required: 3 mins)

1. Select 'add photos' from Workflow menu, or click
2. Browse to the images and upload
3. Selected photos will appear on the Workspace pane. You can view thumbnails of photos by selecting the 'Photos' tab at the bottom of the pane.

Estimating Image Quality (Estimated Run Time: 3 mins)

1. Navigate to the Photos tab
2. Change image display to 'Details' by clicking and selecting this view
3. In the photos pane right click and select 'Estimate Image Quality….'
    a. Apply the analysis to all cameras
4. Once complete filter results by 'Quality' and delete any images with estimated quality <0.5 (threshold recommended in User Manual, may be adjusted as needed)
    a. Low image quality can be caused by high blurriness and over/under exposure. Including these images into your dataset will decrease overall model accuracy.

Align Photos (Estimated run time: 10 mins)

1. Navigate to the 'Reference' tab to view reference details for each image. These data were captured by the UAV during flight. Some UAVs are not capable of collecting reference data, which affects how you align in PhotoScan.
2. In the Workflow menu select 'Align Photos…'
    a. Accuracy: High
    b. Pair preselection: Reference*
        i. *Reference data is available, if missing you would select 'generic'
    c. Advanced → Key Point Limit: 400,000 and Tie Point: default
3. Execute

Check Camera Alignment (Estimated Time 15mins)

1. Navigate to Photos tab and sort by 'Aligned'
    a. Cameras may not align due to insufficient overlap between images or high texture homogeneity. If you discover these issues the best course of action is to collect additional data, with either increased overlap or altered flight parameters (ie. higher altitude)
2. If there are a lot of images (ie. 50%) missing alignment (no green checkmark):
    a. Select images which are not aligned

b. Right click and select ‘Reset Camera Alignment’
c. Re-run alignment on whole dataset (follow step 2 from **Align Photos** instruction section) and use the ‘generic’ reference setting

3. If only a few images are missing alignment, either:
    a. Remove these images by selecting and deleting (ie. if ~3 images don’t align by the edge due to low overlap)
    OR (if you think you’ll have time)
    b. Manually assign tie points by:
        i. Select images which are not aligned, Right Click and select ‘Reset Camera Alignment’
        ii. Right click in the photo pane and select ‘Filter Photos by Selection’
        iii. Double click on any image and scroll through them in full screen to see why they might not have aligned
            1. ie. low, leafy shrubs obscuring ground, with no clear individual tree tops or individual plants to identify will cause issues which cannot be addressed with manual tie points
        iv. If the issue is not clear, try assigning manual tie points:
            1. Identify points that you can visually match between photos (tie points)
            2. Right click at a tie point and select ‘create marker’ (you can rename if you right click on the marker)
            3. Navigate to another image which includes the same tie point and right click on the tie point, selecting ‘place marker’ and placing the corresponding tie point marker
            4. Place at least 4 markers per photo and find at least 2 of these points in neighbouring images which have been correctly aligned to assign image projection data
            5. In the Photos pan select your non-aligned photos and right click. Select ‘Align Selected Cameras’
            6. Return to the Model tab to view your results
            7. You can remove the image filter at any time by clicking
        v. Remove any few remaining images you are not able to align

Geo-Referencing (Estimated Time Required: 30mins – 45mins)

1. Navigate to the Reference tab and upload your georeferencing GCP data ‘Georeference.csv’ by clicking and selecting the file (be sure to match the correct import columns with the data you want)
    a. Coordinate system: WGS 84 (EPSG::4326)
    b. Delimiter: Comma
    c. Start import at row: 2
    d. Label: 1
    e. Longitude: 6
    f. Latitude: 5
    g. Altitude: 4
    h. Uncheck “load orientation” as these are ground survey points
2. Since you have not previously created these markers PhotoScan will ask you if you want to create them. Click Yes to All.

3. Open Google Earth and upload 'Bog_Site_Lab.kml'
    a. Turn on: Georeference markers, Site boundary and roadway to orient yourself
    b. Refer to this document when attempting to locate georeferencing GCPs
4. In PhotoScan:
    a. You can toggle camera positions on and off by clicking
    b. Locate GCP center points in images by:
        i. Select and filter images you believe to capture each GCP location using the select tool ( ), right clicking and selecting 'filter photos by points' (or just scroll through ALL images to get started). Use Google Earth as reference in locating GCPs – use features such as seismic lines, the roadway and pipeline to orient yourself.
        ii. Scroll through photos by double clicking one and using Page Up and Page Down, using the scroll bar on the mouse to zoom in or out
        iii. Once you find a GCP, Right click and select 'place marker', placing the corresponding marker in the center point of the GCP (or as close as possible)
        iv. Avoid marking photos where GCP is extremely skewed unless you are unable to locate better quality images as this will increase model errors. You can zoom to full image extent quickly by clicking
        v. Once you have located a GCP in at least 2 images, PhotoScan will estimate its location. You can then refine your selected images by right clicking on the marker in an image, or the Reference pane, and selecting 'filter photos by marker'. PhotoScan will then display a list of photos it estimates the marker to be in. Go through these images and adjust the marker to the center point. For markers to be turned on, they must be green ( ) this occurs once you have manually adjusted their location. If the flag is not green (ie. grey) the point will NOT be considered in dense point cloud generation.

***If you have difficulty locating the GCPs, open 'GCP_IMGs.xls'. This document includes a list of images which you are able to locate the GCPs in ***

Optimizing Camera Alignment (Estimated Time Required: 5mins)

This portion of the workflow is not necessary to produce a dense point cloud. However, it does remove high error tie points from the sparse point cloud prior to dense point cloud generation, which results in a more accurate model. The following thresholds were developed from data collected by an Aeryon Skyranger fitted with an HDZoom30 optical camera (reported 2.9cm ground resolution). If your data is of lower quality you may have to lower the thresholds to avoid removing too many points. As you proceed through the workflow and select points for deletion, ensure they are not concentrated in one spot otherwise you will end up with major data gaps. It is up to you to play with the thresholds to determine what is appropriate for your data.

1. Navigate to the reference tab and uncheck all images (select all, right click and select 'uncheck')
2. Optimize Cameras using GCPs only by clicking and running with default settings
3. Remove high error points by the following processes:
    a. Edit > Gradual Selection > Reconstruction Uncertainty (10) > Ok > Delete ( )

b.
c. Edit > Gradual Selection > Reconstruction Uncertainty (10) > Ok > Delete ( )
d.
e. Edit > Gradual Selection > Reprojection Error (1) > Ok > Delete ( )
f.
g. Edit > Gradual Selection> Projection Accuracy (10**) > Ok > Delete ( )
    i. ** Do not use this threshold if more than 10% of the points are selected, adjust it to select fewer than 10%
h.
i. Manually select and delete any obvious outliers (ie. points extremely high or low)
j.

Dense Point Cloud (Estimated Run Time: 20mins)

The following settings are data specific and dependent on your research objectives, you may increase the quality setting to 'High' but this may also increase the noisy-ness if your dense point cloud. If you are working with data from vegetated areas you should either select 'Mild' or fully disable depth filtering. Depth filtering removes points which PhotoScan deems too far from the surface based upon the threshold you have selected. Choosing 'High' depth filtering is the most stringent threshold and will result in poorly estimated vegetation heights. High depth filtering is designed for models of smooth surfaces or items with low anticipated surface variability (ie. dinosaur fossils).

1. From the Workflow menu select 'Build Dense Point Cloud':
    a. Quality: Medium
    b. Advanced → Depth filtering: Mild
    c. Execute
    d. You can view the results in the Workspace pane by double clicking the Dense Cloud
2. Export your Dense Point Cloud by right clicking on it in the Workspace pane and selecting 'Export Dense Cloud…'
    a. Save in .laz file format

Accuracy Assessment (Estimated Required Time: 5mins)

PhotoScan already calculates estimated errors for each GCP you used to geo-reference but it's always better to perform an independent test since error should theoretically be 0 at geo-referencing GCP locations.

Perform the independent accuracy test:

1. Upload your validation GCP locations 'Validation.csv' into the Reference pane
2. Manually locate validation points in photos (see step 5 in **Geo-referencing** section)
3. In the Reference pane click to see PhotoScan location estimates and to see estimated errors
4. Export the estimated locations by clicking , saving as .txt and selecting 'markers'. Be sure that 'save estimated values' is selected.
5. Open the .txt file in Excel and view the estimated x, y and z errors. Alternatively, you may compare the estimated X, Y, and Z values for each validation point with those found

in the ‘Validation.csv’ file to manually calculate errors (first converting Lat/Long to UTM for comparison).

Generate OrthoPhoto (Estimated Required Time: 20mins)

In Workflow menu:

1. Build mesh: default settings except change Source Data to ‘dense cloud’
2. Build texture: default settings
3. Build Orthomosaic: default settings
4. Export Orthomosaic as a .tif file, check ‘write BigTIFF file’
    a. Make a note of the resolution, listed in brackets next to the orthophoto in the Workspace pane.

A(III) RE-PROJECTING POINT CLOUDS USING LASTOOLS

Sometimes when you export a dense point cloud from PhotoScan it will need to be re-projected. You might already know this if you're planning to compare it against another dataset with a different projection, or it may become obvious when you attempt to view the dense point cloud and get something like this:

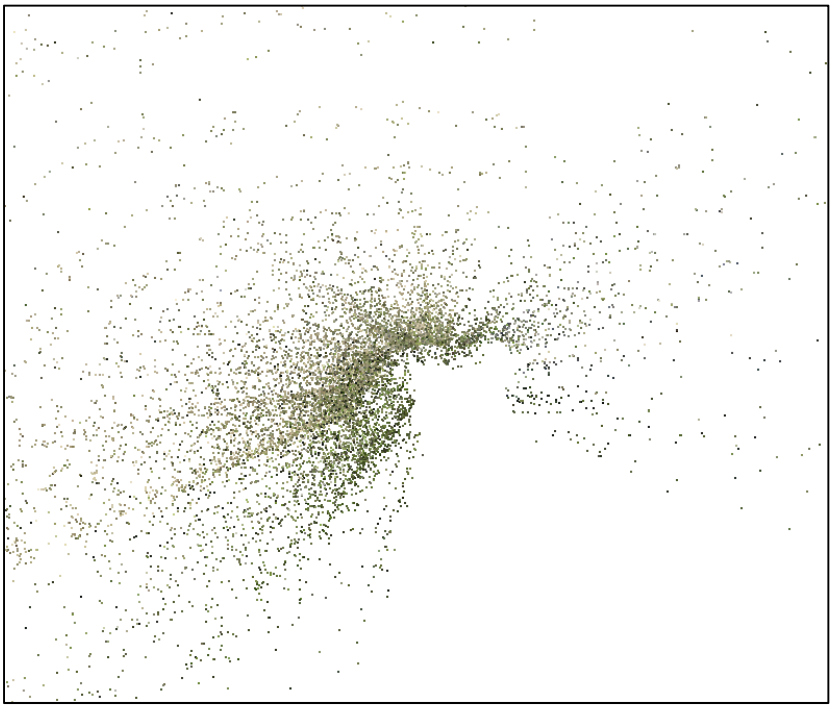

Either way, it's a quick fix. There are two ways to use LAStools to re-project your point cloud: i) from the command line, and ii) using the Las2Las GUI. This tutorial will show you how to re-project a dense point cloud from Lat/Long to UTM coordinates.

Scenario 1: Command Line

1. From the Start menu of your computer open the command line (type 'cmd' into the search bar)
2. Navigate to your LAStools bin folder. Example: **cd: C:/LAStools/LAStools/bin**
3. Re-project your data using the Las2Las tool
    a. Code format is: *las2las –I "input file name.laz" –odir "output directory" –o "output file name.laz" –longlat –target_utm auto*

Example:

las2las.exe –i "c:\LAStools\LAStools\bin\Sibbald Lake\May_Data\sibb_may_DPC_optim.laz" –odir "c:\LAStools\LAStools\bin\Sibbald Lake\May_Data" –o"sibb_may_repro_UTM.laz" –longlat –target_utm auto

4. You should now be able to open the re-projected file to make sure it worked. If it did not, have a look through the cmd window to see where the error is

Scenario 2: Las2Las GUI

1. Navigate to the Las2Las application file in the bin folder and open it
2. Browse to your desired input file and double click it to input:

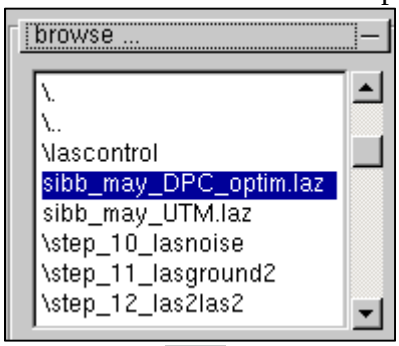

3. Select your output directory by clicking

under the ‘output’ menu on the right side of the GUI:

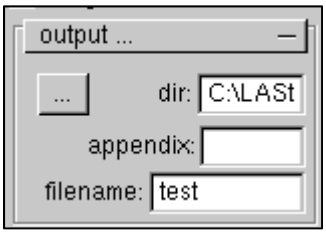

4. Give your output file a name in the ‘filename’ line
5. Expand the target projection menu and select your desired projection etc. and precision:

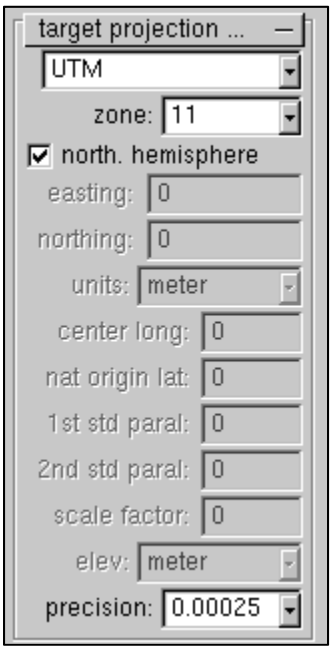

6. Click ‘RUN’
7. Once complete, open the output file to make sure it re-projected correctly. If it did not, have a look at the cmd window to see what the error might be.

In either case, you will hopefully end up with something like this:

Instead of what you started with:

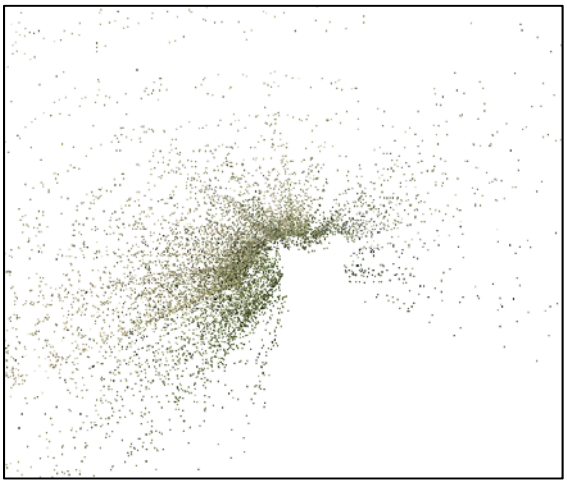

Alternatively you make use other tools/applications to re-project your data.
For example pdal (discovered by the lovely Jordan Eamer):
https://www.pdal.io/workshop/exercises/translation/reprojection.html

A(IV) UPDATING IMAGE PATHWAYS IN PHOTOSCAN
(A tutorial for non-programmers)

This is an important step if you wish to share a .psx file with collaborators, or move the saved location of your PhotoScan project. If you do not update the image pathways you will run into an error (see below) when attempting to access individual images from the Photos tab in PhotoScan. This results in PhotoScan loading the thumbnail (super low resolution) rather than the high quality image you used for point cloud/orthophoto generation.
Example Error:

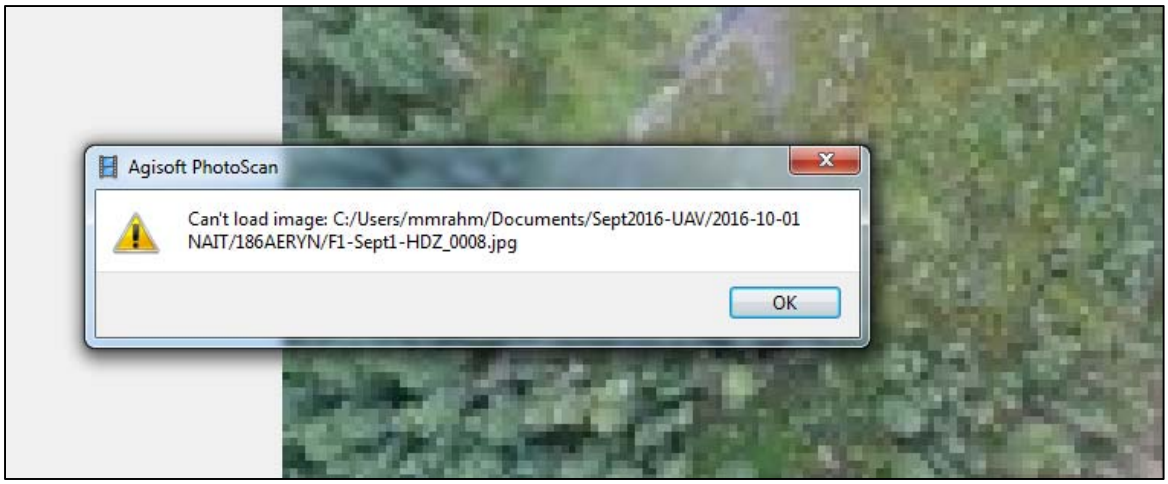

To update the pathway information directly (not using Python) is simple. Each PhotoScan project generates a .psx file and a corresponding .files folder. You will be working in the .files folder.

You will need:

1. Notepad++ (or similar)
2. 7zip (or similar)
3. Knowledge of where the images are now saved so you can update the pathway

Steps:

1. In Windows explorer navigate to the frame.zip file for the project you wish to update.
    a. Example: G:\CarmonCreek-Sept2016-FEN-wGCPs-optim.files\0\0\frame.zip

2. In Notepad++
    a. Open the doc.xml file located within the frame.zip folder
        i. The best way to do this is to copy the document location from your windows explorer (step 1) and paste it into Notepad++ open file path
            1. Attempting to open the frame.zip file in Notepad++ directly won't work

Example: file pathway in Windows explorer to be copied into Notepad++:

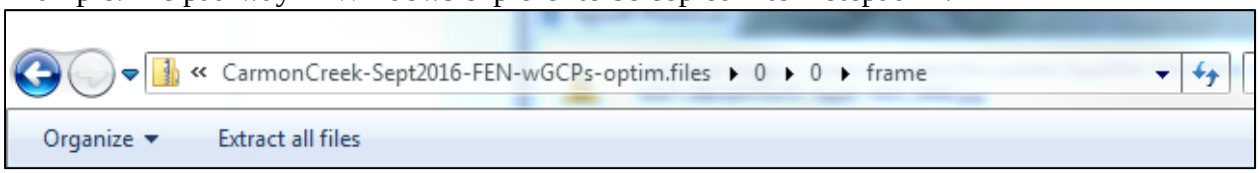

File pathway copied into Notepad++, with doc.xml file shown:

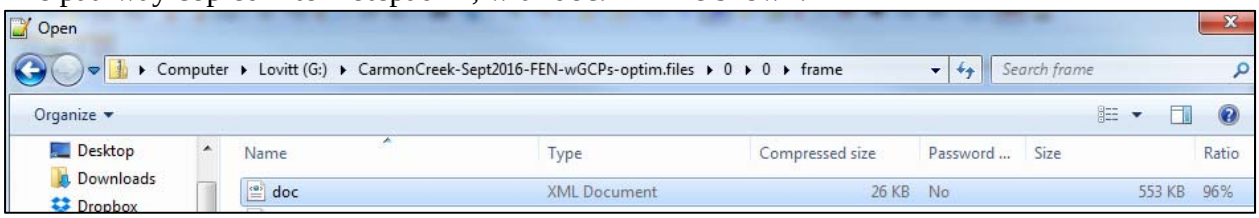

b. In the file you will see a bunch of code. You are going to update the photo path line:

```
<photo path="G:/Fen_sept_images/2016-10-01NAIT/186AERYN/F1-Sept1-HDZ_0001.jpg">
```

c. Hit CTRL+H to open the find & replace window

d. In 'Find' line: enter the old image pathway you want to replace

e. In 'Replace' line: enter the updated image pathway (example below)

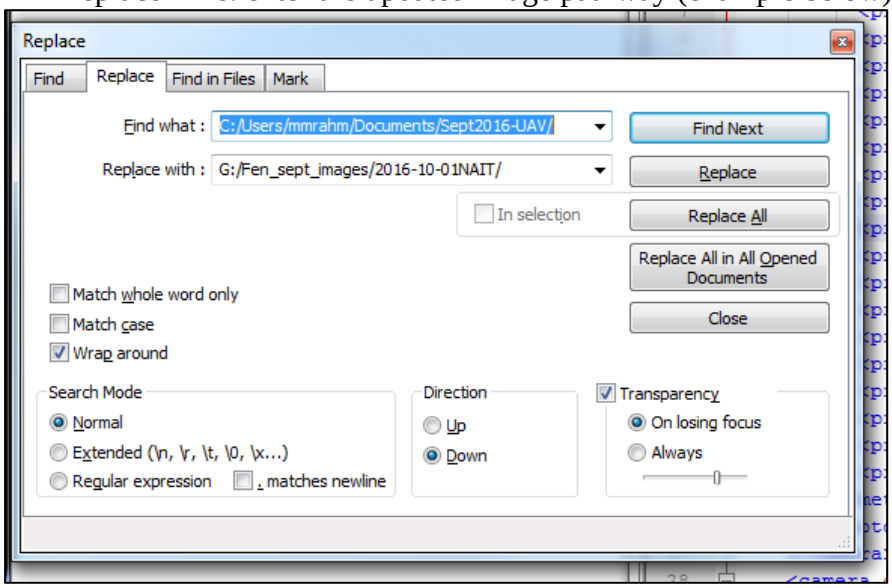

f. Save document as doc.xml to your Desktop

3. In Windows explorer right click on the frame.zip folder and select:
   a. 7zip>Open Archive

4. In 7zip rename the doc.xml file to something else (example: doc_old)
    a. You do not want to delete this file in case you make a terrible mistake

5. Drag the updated doc.xml file from your Desktop into the 7zip archive and click ‘YES’ to the warning

6. Close 7zip and Notepad++

7. Open your PhotoScan project and try opening an image in the Photos tab
    a. If it still gives you an error go back and check the photo path code in Notepad++ to make sure there are no extra spaces, missing slashes etc.

A(v) Extracting Ground Points from Dense Point Clouds (when the PhotoScan Point Classification Tool is Inadequate)

This tutorial will assist you in extracting the ground from a dense point cloud. It is important to note that Agisoft PhotoScan includes a classification tool which activates once you have finished generating all products (dense point cloud, ortho, mesh, texture etc.). It is located under Tools>Dense Cloud>Classify Ground Points. Have a look at the performance of this tool before you jump into the following tutorial as it may produce acceptable output for your needs. PhotoScan classification tool uses step and angle thresholding to classify ground points.

Assuming you have already played with the classification tool from PhotoScan and found it lacking, you may experiment with LAStools and Cloud Compare. LAStools is similar to PhotoScan in that it uses step and angle thresholding, however you have many more tools at your disposal and have more control over the filtering than in PhotoScan, which is handy for complex datasets.

1. You will need an updated LAStools license in the bin folder to have full access to all tools.
2. You will need a copy of Cloud Compare if not already installed. Free download here: http://www.danielgm.net/cc/release/

In this tutorial 'noise' refers to all points in the cloud which are not considered ground – such as trees/vegetation and actual noise.

Step 1. Pre-Noise Filtering (roughly extracting ground points):

1. Export dense point cloud (DPC) from PhotoScan (after manual removal of clear outliers)
2. Reproject las file if necessary: Full steps provided in tutorial "*Reprojecting Point Clouds using LAStools*"
    a. Quick guide:
        i. Las2Las: reprojection of DPC into UTM using code: "las2las -i in.las -o out.las -longlat -target_utm auto"*
        ii. * use this file for next steps

Step 2. 'Noise' Filtering:

Alter thresholds as necessary, this workflow is data specific meaning these values may not work for your data or for site data collected on different dates. LASground relies primarily upon point isolation and positional thresholds (ie. elevation spike) to distinguish ground from surrounding points in the cloud. This does not work very well with high density clouds such as what you produce from UAV data, hence the need for filtering with Cloud Compare. LAStools and Cloud Compare are both open source software packages, meaning tools may have been developed in the time since this tutorial was created, and/or other software packages may now exist which do a better job of extracting ground from dense clouds. It is worth it to spend some time researching current approaches to ground extraction prior to executing this workflow. **I highly recommend reading the README file for each LAStool before you use it.** This will

explain how the tool works and allow you to better modify the thresholds for your data, increasing your efficiency. If at any point a LAStool fails to execute you can refer to the command window for an error report.

Using LAStools:

1. Lastile: tile size = 550, buffer = 15
2. Lasground: *custom settings**:*** step = 1, bulge = 0.5, spike = 0.3, offset = 0.2, std dev = 3, "-coarse" added to code, compute height = checked
3. Las2las: filter = keep_classification_2
4. Lastile: remove buffer points
5. Las2las: merge files into one = checked
6. **In Cloud Compare:**
    1. Import file from step 7 to Cloud Compare (CC) and allow for data shift
    2. CC statistical outlier removal (SOR) Filter: # of points = 100, std dev = 1.5
    3. CC noise filter: radius = 0.5, max err (abs) = 0.5, remove points = checked
        a. Export filtered files from CC in .las format

Back to LAStools:

7. Lastile: tile size = 250, buffer = 15*
    a. *merged file is too large (too many points) to perform step 12 without tiling
8. Lasview: Unclassify **all** points (set classification to 1)*
    a. *Perform separately for each tile unless you figure out how to batch
        i. Wait for all points to load in view window before:
        ii. Right Click > reclassify points as > unclassified (1)
        iii. R = registers the change
        iv. Ctrl + S = saves changes to .lay file
        v. Ctrl + A = converts .lay file to .las file
        vi. Wait for message indicating .las file has been written prior to closing view window
9. Lasnoise: step (x,y) = 2, step (z) = 0.5, isolated = 300
10. Lasground: *custom settings*: step = 5, bulge = 0.25, spike = 0.25, offset = 0.25, std dev = 1, ignore points = 7, computer height = checked
11. Las2las: filter = keep_classification_2 (or drop classifications 1 & 7), drop_z_above_624
    a. Select elevation threshold (ie. 624 for bog or 625 for fen) by comparing outliers to known ground points (use 'I' in lasview to read x,y,z coordinates for individual points)
12. Lasview: inspect & manually remove outliers
    a. Example of outliers (lingering vegetation):

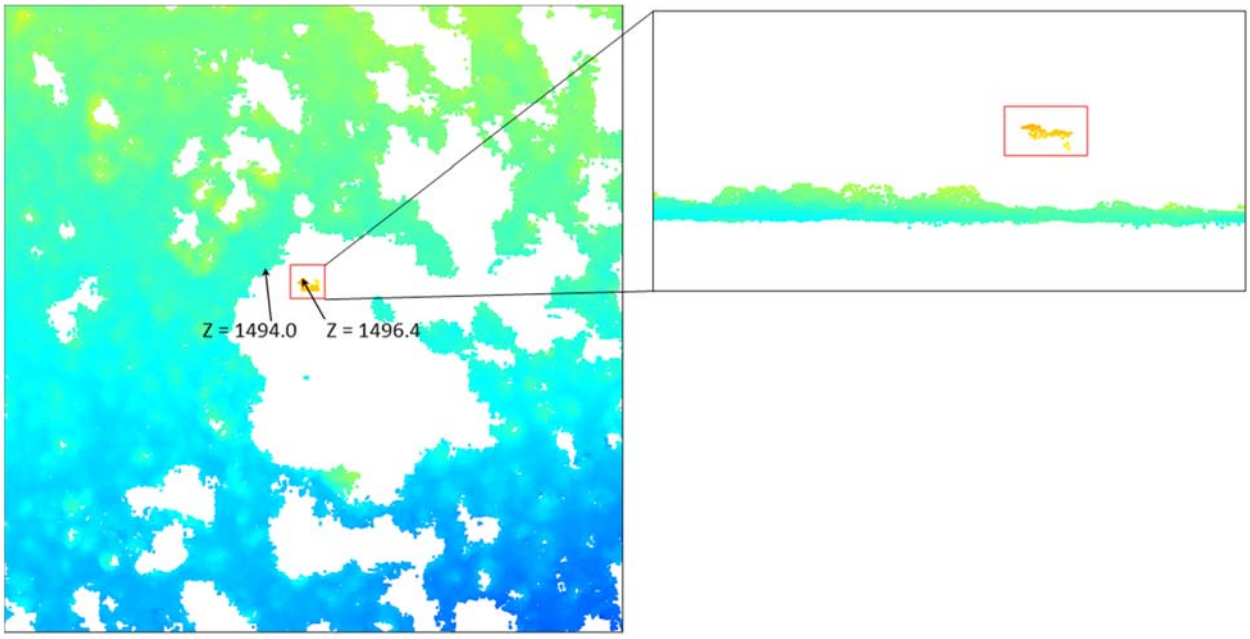

13. Lastile: remove buffer points
14. Las2las: merge files into one = checked, target projection = UTM Zone 11, WGS84, keep_classification_2, output format = .las
15. Quickly estimate accuracy of output: lascontrol against validation points
    a. **Note: LAScontrol validates based on comparison with TIN surface – use as quick estimate only to determine whether workflow tweaks are necessary, unless interpolation method is unimportant to your final products**

This is the end of the ground point extraction workflow. There are multiple ways to convert the cloud into a DTM, ***see tutorial "Converting Ground Dense Point Clouds to DTMs and Validating"*** *for quick summary using ArcGIS and LAStools. I recommend ArcGIS for this task, LAStools output for large datasets requires merging in QGIS which is time consuming and prone to errors, plus LAStools interpolates using TIN (cannot change) which is another reason why ArcGIS is superior as you have more control over interpolation method and parameters (ie. resolution). However, it's always a good idea to have a plan B in case there are issues with ArcGIS output. I encourage you to refine this workflow, or develop a superior one as new tools are developed.*

A(VI) CONVERTING GROUND POINT CLOUDS TO DTMS AND MODEL VALIDATION IN ESRI ARCMAP

1. Open ArcMap and create new LAS dataset:
    a. Data Management Tools > LAS Dataset > Create LAS Dataset
    b. Input = LAS file from Step 14 in ground extraction workflow
        i. Specify coordinate system
2. Convert point cloud to Raster:
    a. Conversion Tools > To Raster > LAS Dataset to Raster
        i. Select preferred interpolation method and input cell size to achieve desired resolution of Raster (ie. 0.02 = 2cm in UTM coordinate system)

LAStools Method (Not recommended unless ArcMap doesn't work for some reason):

1. Input = LAS file output in Step 14 from ground extraction workflow
2. Lastile: tile size = 550, buffer = 0 (file too large to generate DEM without tiling)
3. Las2dem: step = 1, kill >100, -elevation, actual values, format = .tif
    a. **Note: LAStools generates a DEM using TIN interpolation which may be undesirable depending on your project goals**
    b. If you do not wish to output TIN interpolated DEM follow ArcGIS workflow
4. Import tiled las2dem output into QGIS & Merge dataset
    a. Raster > Miscellaneous > Build Virtual Raster (Catalog) > select visible raster layers for input > enter output name > Ok
    b. Double check elevations are reported correctly!

Validating Models with RTK Reference Points (ArcGIS)

1. Input reference points into ArcGIS: Right Click input table > display x,y data
2. Input Raster (DTM) you wish to assess the accuracy of
3. Extract Raster values to reference points and export to Excel for comparison:
    a. Spatial Analyst Tools > Extraction > Extract Values to Points
    b. Right click on output in ArcMap > Open Attribute Table
        i. Menu > Export… > Save as .txt
    c. Open .txt file in Excel and convert to useable format:
        i. Select Column 1 in Sheet > Data Tab > Text to Columns
    d. Compare Raster value with reference point RTK elevation value
    e. Calculate stats like RMSE from difference etc.

A(VII) APPLYING FILTERS TO A MASKED IMAGE IN ENVI

Sometimes you need to generate new data for further processing by applying filters to masked data. Unfortunately, ENVI does not properly ignore 0 values in the filter calculations, so your masked cells are included rather than ignored, skewing output and misrepresenting true conditions. To correct this, the wonderful Dr. Mustafiz Rahman created a series of codes which you can execute in the IDL window depending on the kind of filter you wish to apply. You can run them all or separately by adding lines to specify data location at the beginning of each code, and/or 'end' commands to stop the process after it completes.

Code 1. Apply a Median Filter to data within DN range 500-800 (excludes masked values '0'), window size approx. $2m^2$ (cell size 2cm), and output as tif file:

```
Pro DefineRef

data = read_tiff("C:\Users\julie.lovitt\FeaureExtraction-FenJuly2016\SeptDTM_MaskedNodata.tif", Geotiff =
GEO)

W = (size(data))[1]
print, "width = ", W
H = (size(data))[2]
print, "height = ", H

outputMedian = fltarr(w, h)
for i = 51, W-51 do begin
  for j= 51, H-51 do begin
    if data[i,j] gt 500 and data[i,j] le 800 then begin
      Cdata = data[i-51:i+50, j-51:j+50]
      location = where((Cdata gt 500 and cdata le 800), Count)
      ;print, 'number of finite pixels = ', count
      TrimCdata = Cdata[location]
      outputMedian[i, j] = median(trimCdata)
    endif else begin
      outputMedian[i, j] = data[i, j]
    endelse
  endfor
endfor

write_tiff, "C:\Users\julie.lovitt\FeaureExtraction-FenJuly2016\Bog_Test\SeptDTMRef_Med.tif", outputMedian,
/float, Geotiff = GEO
outputMedian = !NULL

Print, "median file created"
end
```

Code 2. Apply a Mean Filter to data within DN range 500-800 (excludes masked values '0'), window size approx. 1.5m^2 (cell size 2cm), and output as tif file:

```
Pro DefineRef

data = read_tiff("C:\Users\julie.lovitt\FeaureExtraction-FenJuly2016\SeptDTM_MaskedNodata.tif", Geotiff =
GEO)


outputMean15 = fltarr(w, h)
for i = 37, W-38 do begin
  for j= 37, H-38 do begin
    if data[i,j] gt 500 and data[i,j] le 800 then begin
      Cdata = data[i-37:i+37, j-37:j+37]
      location = where((Cdata gt 500 and cdata le 800), Count)
      ;print, 'number of finite pixels = ', count
      TrimCdata = Cdata[location]
      outputMean15[i, j] = mean(trimCdata)
    endif else begin
      outputMean15[i, j] = data[i, j]
    endelse
  endfor
endfor


write_tiff, "C:\Users\julie.lovitt\FeaureExtraction-FenJuly2016\Bog_Test\SeptDTMRef_Mean15.tif",
outputMean15, /float, Geotiff = GEO
outputMean15 = !NULL

Print, "mean 1.5 file created"
end
```

Code 3. Sort data values within filter window and drop outliers (top 100, bottom 100) before applying a Mean Filter to data within DN range 500-800 (excludes masked values '0'), window size approx. $2m^2$ (cell size 2cm), and output as tif file (note: this one takes days to run if you apply to a large dataset):

```
Pro DefineRef

data = read_tiff("C:\Users\julie.lovitt\FeaureExtraction-FenJuly2016\SeptDTM_MaskedNodata.tif", Geotiff =
GEO)


outputMean2trim = fltarr(w, h)
for i = 51, W-51 do begin
  for j= 51, H-51 do begin
    if data[i,j] gt 500 and data[i,j] le 800 then begin
      Cdata = data[i-51:i+50, j-51:j+50]
      location = where((Cdata gt 500 and cdata le 800), Count)
      ;print, 'number of finite pixels = ', count
      TrimCdata = Cdata[location]
      sortLoc = Sort(TrimCdata)
      SortedTrimCdata = TrimCdata[sortLoc]
      if count gt 250 then begin
        SampleCdata = SortedTrimCdata[100:count-101]
        outputMean2trim[i, j] = mean(SampleCdata)
      endif else begin
        outputMean2trim[i, j] = mean(SortedTrimCdata)
      endelse
    endif else begin
      outputMean2trim[i, j] = data[i, j]
    endelse
  endfor
endfor


write_tiff, "C:\Users\julie.lovitt\FeaureExtraction-FenJuly2016\Bog_Test\SeptDTMRef_Mean2Trim.tif",
outputMean2trim, /float, Geotiff = GEO
outputMean2trim = !NULL

Print, "processing complete"
end
```

A(VIII) OBIA IN ECOGNITION WITH ACCURACY ASSESSMENT IN ESRI ARCMAP

This tutorial will provide a starting point for anyone interested in performing feature extraction (by developing a rule set) in eCognition, and subsequently assessing classification accuracy in ArcMap. Data used here includes an RGB orthophoto and specialized elevation data which was created for use in identifying Hummocks from Hollows across a peatland of Northern Alberta. Additionally, the data used here includes RTK points used in the accuracy assessment. As a result, there was no need to select 'training sites' for the accuracy assessment. This may be different for you depending on your data.

Step 1: Building a Ruleset in eCognition

1. Watch the YouTube videos from Jarlath O'Neil-Dunne, especially this one (https://www.youtube.com/watch?v=QEDGz749lwc&t=398s&list=PLG0a9U3eef7ogzqmj2PwTy2splFdHKe7i&index=1) and follow along with your data to develop rules:
    a. Using a subset of your data if it is a large dataset, tweak your rules until you believe your results are adequate for full site classification

    b. Try changing the weighting of bands in your segmentation to improve your output segments (ie. if your data is: R,G,B,Elevation and classes are clearly visually apparent in the green band, you may change weights to something like: 1,3,1,1)

    c. eCognition allows you to develop a wide variety rules including: spectral, proximity, elevation etc. The rules will be specific to your data and research objectives, therefore this tutorial won't go into great detail. Jarlath does an excellent job in his youtube videos.

    d. Once you are happy with your classes, merge your class polygons to reduce export time
        i. You will need to create merge rules for each of your classes, if you just run one it will merge all polygons regardless of class so you'll end up with one large polygon

    e. Export vector layers for each class with meaningful names like 'bog_sept_ruleset1_Trees'

Step 2a: Assigning Class Results to your Validation Points for Assessment

This assumes you have RTK validation points available for all classes

In ArcMap:

1. Open the polygon layers individually and create new field to list class name
    a. Right click on layer > Open Attribute Table > Menu ( ) > Add Field > Type field name (ie. 'Class') > type = text > OK
    b. Right click on newly created field in Attribute Table > Field Calculator > enter class name (ie. "Trees") > OK > Close Attribute Table
        i. Repeat for each class vector you have imported

2. Merge Class polygons into one file
    a. ArcToolbox > Data Management Tools > General > Merge

3. Convert merged polygon to Raster
    a. ArcToolbox > Conversion Tools > To Raster > Feature to Raster > field = Class > output cell size = desired resolution

4. Assign Raster values to your validation points
    a. ArcToolbox > Spatial Analyst Tools > Extraction > Extract Values to Points

Step 2b: Select Validation Points (training sites) for Accuracy Assessment

Complete this step if you don't have RTK point data for all classes

1. Watch & follow this YouTube Video: https://www.youtube.com/watch?v=FaZGAUS_Nlo

Step 3: Assess the Accuracy of your Classification

In Excel:

1. Compare the raster class to the field assigned class for each point and generate a confusion matrix

2. Calculate the kappa statistic
    a. Online calculator: http://vassarstats.net/kappa.html

3. Return to your ruleset if necessary to improve your classification accuracy

4. If you are satisfied and have been working with a subset, apply the ruleset to the full dataset and repeat accuracy assessment. You might find the results are surprising and need to tweak some rules that don't appear to work well across the entire study area.

A(IX) GCP DESIGN CONSIDERATIONS – REVIEW OF PROBLEMS FROM 2016 PEATLANDS RESEARCH PROJECT

This document will provide you with some image comparisons of GCPs used in the 2016 peatlands research project. Hopefully this will help you select the proper GCP design for your flights and you can avoid problems we ran into. Conclusions and recommendations are summarized after each comparison.

Permanent GCP (pGCP) Specs: 10 installed across site
Size: 25cm^2
Materials: steel plate, poorly painted by summer students (unclear middle point) with different coloured corners and letters A – J for easy identification (theoretically)
Fastening Design: four 2m long metal rods pounded through peat to underlying mineral layer via rubber mallet, fastened to GCP corners through pre-drilled holes and wing-nuts

Example: pGCP Paint Design (No Stencil Used)

Temporary GCP (tGCP) Specs: 50 installed over 3 trips to site
Size: 25cm^2
Materials: Corrugated plastic board and spray paint (Rona)
Fastening Design: one 9’ nail through a corner of the GCP into the ground (Home Depot)

Example: tGCP Paint Design (Stencil Used)

Flight Plan Details:
UAV: Aeryon Scout with HDZOOM30 **OR** EBee with Canon S110 RGB (will be listed by image)
Altitude: 110m (Scout) **OR** 70m (EBee)
Desired Res & Overlap: 2cm, 80% (fore), 60% (side)
Weather Conditions: described for each comparison

Comparison 1a: pGCPs – Full Sun vs Shade Conditions
UAV: Aeryon Scout with HDZOOM30
Flight Date: July, 2017

Conditions: Full sun, two flights conducted (morning and afternoon) to capture different shadow angles

pGCP: Deep Shadows

pGCP: Full Sun

Problem: Steel surface of permanent GCPs highly reflective, causing washout and inability to accurately locate center point.

Comparison 1b: tGCPs – Full Sun vs Shade Conditions

Same flight conditions as 1a

GCP material: RED corrugated plastic board with black spray paint

tGCP: Deep Shadows

tGCP: Full Sun

Result: Temporary GCPs center point more clearly visible in full sun conditions as compared to steel plate permanent GCPs.

Comparison 2: pGCP vs tGCP Painting Design

UAV: EBee with Canon S110 RGB
Flight Date: October, 2017
Flight Conditions: Overcast, 2-3cm snow on ground
Same zoom level shown in images below

pGCP in field (this is the GCP displayed on page 1):

tGCP (RED corrugated plastic board with black spray paint):

Both in Same Image:
(Poor performance of pGCP not due to distortion as it is closer to center of image)

Result: Effort should be taken to paint GCPs as clearly as possible to provide a solid center point for locating. **Use a stencil to get clean edges and pick colours with good contrast!**

<u>Comparison 3: tGCPs Design – RED vs WHITE</u> Corrugated Plastic Board with black spray paint

Notes: WHITE board spray painted fluorescent orange (purchased when RED unavailable) ex. Page 1. WHITE tGCPs had not been installed at site until August which is why there are images from both flights.

UAV: EBee with Canon S110 RGB
Flight Date: May & August, 2017
Flight Conditions: Overcast with a brief window of full sun (August), high clouds, bright (May)

RED Corrugated Board: Full Sun
(Flight – May, 2017)

RED Corrugated Board: Shade
(Flight – August, 2017)

WHITE Corrugated Board: Full Sun
(Flight – August, 2017)

WHITE Corrugated Board: Shade
(Flight – August, 2017)

Result: Don’t use white corrugated board for small GCPs **OR** use a different colour of spray paint on them (not fluorescent orange), and ensure the paint is durable to last wear and tear through summer use.

Comparison 4: tGCPs Design – RED corrugated board in Red Edge Imagery

UAV: EBee with Canon S110 RE
Flight Date: May, 2017
Flight Conditions: High clouds, bright indirect lighting

tGCP: RED corrugated plastic board

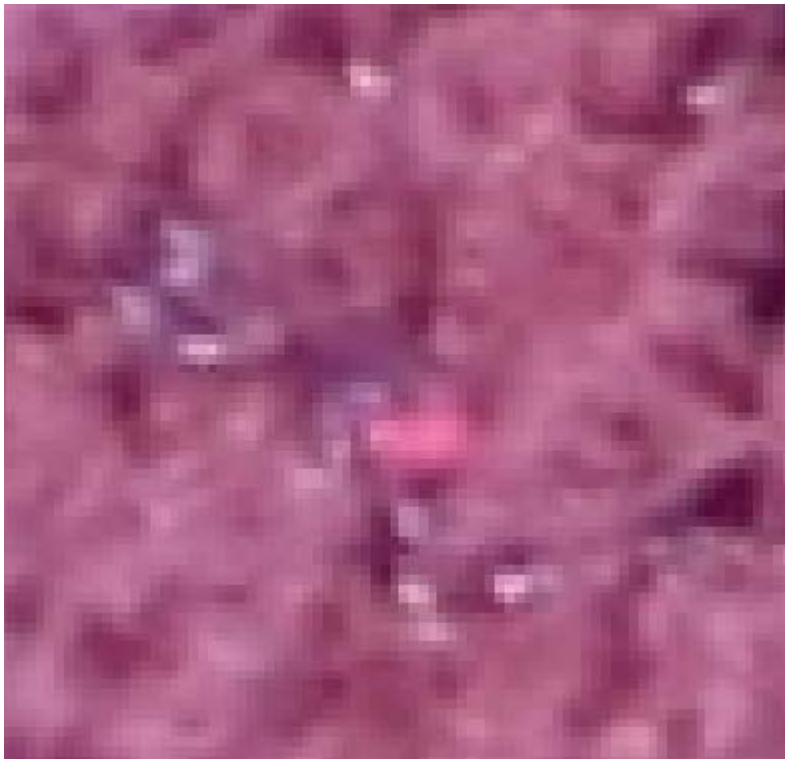

Result: Don't use red plastic GCPs if you plan to collect red edge imagery. They are extremely difficult to locate in vegetated areas.

A(x) How to Bust Clusters in PCI Geomatica

Always save files with clearly named titles and checkmark the Output save file box

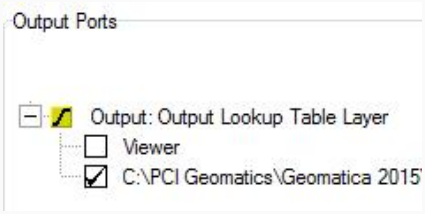

You can find all applications in Geomatica's 'Algorithm Librarian' (Tools>Algorithm Librarian)

1. Create mask of class you want to bust (using THR: input = unsupervised classification layer, parameters: min & max = class you are interested in (ie. 2 and 2 if you want to bust class 2), complement mode should be OFF = all values within class = DN of 1, all values outside class = DN of 0. (If you want to run opposite turn ON, class =0, surrounding =1)

2. Make sure that the produced mask (bitmap) is saved under the image file in Files and Maps tabs (Right click on bitmap mask>Export(save as)>To existing file>*your image file)

3. Rerun unsupervised classification with bitmap applied in drop down:

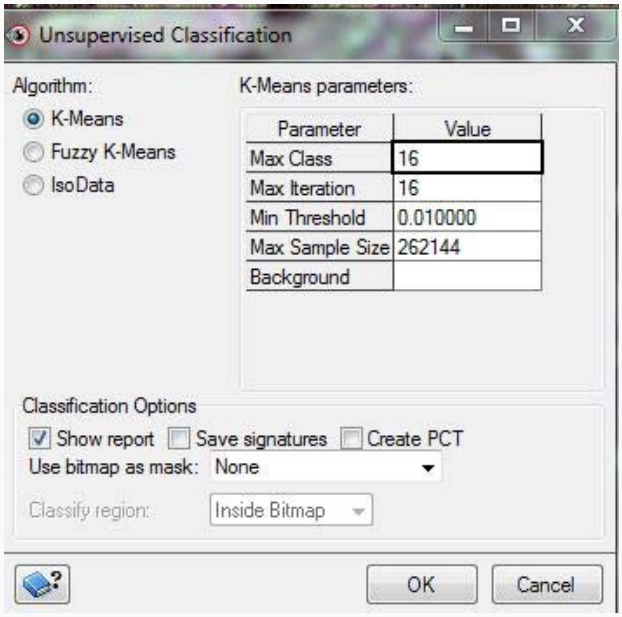

4. Now you have your busted class layer! Toggle between image and layer to ensure it is the class you want. Edit PCT to view 'random' to make sure it has busted the layer properly.

To merge this busted layer into your original classification:

1. REC: Create Recode-LUT Layer (using busted class layer, assigning new values which don't occur in original classification (higher values)) Check Log for success of run. This creates a look up table with the new class values
    a. For example (class values renamed to 21, 22…etc.)

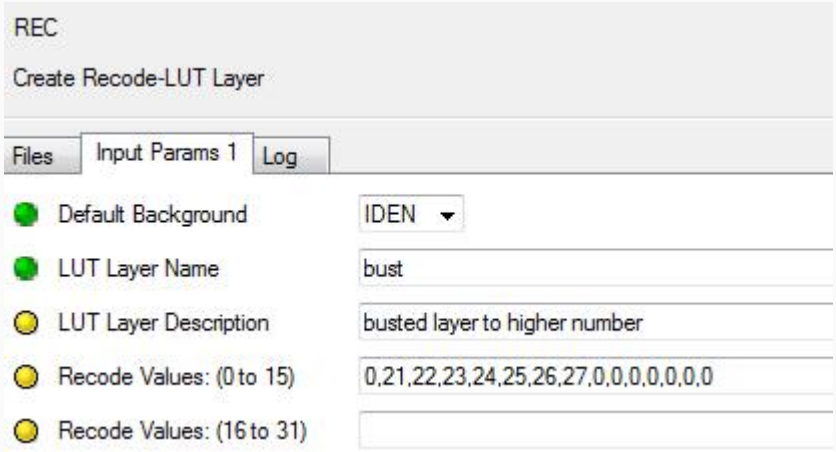

2. **After running, rename layer in map and file tabs if necessary – might still say 'new layer' in title which can become confusing**

3. LUT: Image Enhancement via Lookup Table (input raster = busted layer, LUT = the one you created in REC), select Viewer-PCT, make sure to save the output file (browse if necessary) Check Log for success of run.

4. Now you have created a layer with the new recoded class values! But it still needs to be joined with the original classification

5. Raster Calculator: View> Advanced, Categories>Extreme:

    a. Double click 'Max(a,b)', in the space of 'a' select the original classification layer from the list, in the space of 'b' select the recoded busted cluster classification layer from the list of layers

    b. Save file to original image layer (same file as what you have been working with) and select 'new layer' to produce a new layer (might need to be renamed if it says 'empty' or 'new layer' after running)

6. Now you have a layer which includes your original classification PLUS the busted class!

7. Change view (edit PCT) to display layer as 'random' to make sure you have all the different classes

8. Double check by looking at the histogram to make sure it shows your recoded values